

MODELING THE AIRWAY SURFACE LIQUID
REGULATION IN HUMAN LUNGS

Peiying Zuo

A dissertation submitted to the faculty of the University of North Carolina at Chapel Hill
in partial fulfillment of the requirements for the degree of Doctor of Philosophy in the
Department of Mathematics.

Chapel Hill
2007

Approved by:
Chair of Committee: Dr. M. Gregory Forest
Advisor: Dr. Timothy C. Elston
Advisor: Dr. Richard C. Boucher
Reader: Dr. Jingfang Huang
Reader: Dr. Richard M. McLaughlin

© 2007
Peiying Zuo
ALL RIGHTS RESERVED

ABSTRACT

PEIYING ZUO: Modeling the Airway Surface Liquid Regulation in Human Lungs.
(Under the direction of Timothy Elston and Richard Boucher)

The research in this dissertation is aimed at understanding the pathogenesis of Cystic Fibrosis, which is a life-threatening disorder that causes severe lung damage and nutritional deficiencies. Patients with cystic fibrosis exhibit deficient mucociliary clearance due to enhanced thickness and adherence of the mucus in their airway. In the past a few decades, significant progress has been made in understanding the cause of the disease as well as ways to treat it. Besides conventional treatments for cystic fibrosis, the addition of adenine triphosphate (ATP) to the airway surface of the lung was recently found to be effective to restore mucociliary clearance. Even as scientists begin to understand the signaling pathways that regulate the airway surface liquid (ASL), there are still many parts of this complex system that remain unclear. The ultimate goal of this work is to put together several important “puzzle pieces”, and try to understand how proper regulation of the ASL is achieved.

ACKNOWLEDGEMENTS

I am deeply indebted to my advisors, Drs. Timothy Elston and Richard Boucher, who guided this work and helped whenever I was in need. Without their constant support and encouragement, this work would not have been possible.

I am also very grateful to a group of fantastic people from Cystic Fibrosis Pulmonary Treatment & Research Center at UNC. The beautiful experimental results from Drs. Maryse Picher and Eduardo Lazarowski provided a nice starting point and backbone for this work. The enlightening discussions with Drs. Brian Button, Seiko Okada and Robert Tarran have helped me in understanding different aspects of this work. Without strict training by Dr. Jack Stutts and Mrs. Leslie Fulcher on Ussing chamber and cell culture techniques, I wouldn't have been able to present my own experimental data in this dissertation. I had a really good time working with all of them over these years.

Sincere thanks are also extended to the faculty members in the Department of Mathematics for their support; especially to my committee members Drs. Gregory Forest, Jingfang Huang, and Richard McLaughlin.

My parents, who raised me to be the person I am today, deserve the most acknowledgements. Finally, I thank my beloved husband, Yichao, for understanding, supporting, and loving me.

TABLE OF CONTENTS

LIST OF TABLES.....	vii
LIST OF FIGURES.....	viii
Chapter	
I. INTRODUCTION.....	1
1.1 History and motivation.....	1
1.2 Outline.....	9
II. EXTRACELLULAR NUCLEOTI(SI)DE AND NUCLEOSIDE METABOLISM.....	10
2.1 Introduction.....	10
2.2 Methods.....	11
2.3 Results.....	18
2.4 Discussion.....	30
III. ION/WATER TRANSPORT MODEL.....	45
3.1 Introduction.....	45
3.2 Mathematical equations.....	46
3.3 Parameter estimation.....	51
3.4 Model validation.....	53
3.5 Conclusion.....	55
IV. AIRWAY SURFACE LIQUID REGULATION.....	57
4.1 Introduction.....	57

4.2	Microelectrode studies	61
4.3	Experimental results with ATP.....	70
4.4	Experimental results with UTP.....	83
4.5	Modeling the response.....	85
APPENDICES.....		91
REFERENCES		105

LIST OF TABLES

Table

1. Comparison between parameters of ASL nucleotide release and metabolism functionally measured and estimated from the nonlinear model without fitting or including parameters of ADP and AMP release.....	22
2. Steady-state nucleotide concentrations calculated from the linear model without or with parameters of ADP and AMP release.....	22
3. Diffusion constants of ATP in different media.....	39
4. Comparison of <i>in vivo</i> measurements of membrane permeabilities to ions and water with estimated values.....	51
5. Comparison of variables at steady-state before and after parameter estimation.....	51
6. Experimental observations and numerical simulation calculated by the ion/water transport model in the experiment in which apical sodium channel is blocked by amiloride	52
7. Experimental scheme for measuring the chloride current with single-dose ATP in the apical side of the CF HBE cells.	66
8. Experimental scheme for measuring the chloride current with cumulative-dose ATP in the apical side of the CF HBE cells	66
9. Experimental scheme for measuring the sodium current with single-dose ATP in the apical side of the CF HBE cells.....	68
10. Experimental scheme for measuring the sodium current with cumulative-dose ATP in the apical side of the CF HBE cells	68
11. Experimental scheme for measuring the transmembrane current that is composed of both sodium and chloride ions.....	68
12. Different scenarios for testing the integrated model.....	87

LIST OF FIGURES

Figure

1. The structure of the human respiratory system	2
2. Gene location of CFTR.....	3
3. Regulation of PCL layers by active ion transport.....	6
4. Diagram of nucleotide transport/metabolism on the apical surface of human airway epithelia.....	12
5. Comparison of model prediction with experimental measurements for steady state [ATP] and [ADO].....	16
6. Model validation of the transient and steady-state concentration profiles generated by the nonlinear model without data fitting.....	19
7. Model validation of the transient and steady-state concentration profiles generated by data fitting using the Matlab least square program and without (A, B) or with (C, D) a fixed rate of ATP release.....	21
8. Validation of the transient and steady-state concentration profiles generated by data fitting using the nonlinear model including parameters of ADP and AMP release.....	23
9. Sensitivity analysis of the nonlinear model including ADP and AMP release for low-affinity NS AP and high-affinity E-NTPDase.....	25
10. Relative contribution of Ecto 5'-NT and NS AP to airway adenosine regulation	27
11. Layered structure of the ASL in human lungs.....	34
12. The activities of nucleotides and nucleosides in the ASL.....	36
13. The averaged ATP concentration in the ASL when varying the diffusion rate in mucus layer D_M with respect to the diffusion rate in PCL D_P	40
14. Initial condition of aerosol ATP delivery to the ASL.....	41
15. The local ATP concentration at epithelial cell membrane numerically solved from the partial differential equation system.....	42
16. The transport processes in human airway epithelium.....	44
17. Voltage-clamp circuit representing the equilibrium state of transmembrane currents.....	48

18. Comparison of the <i>in vivo</i> measurement (black) and simulation results (red) for ion concentration and membrane potentials before (A) and after (B) the parameter estimation.....	50
19. Simulation of ATP depletion in human airway.....	53
20. The signaling pathways activated by ATP and adenosine in the normal and CF human epithelia.....	56
21. Polycarbonate snapwells for cell culturing.	61
22. Profusion Ussing chamber setup for measurement of transepithelial short circuit current.....	64
23. Measurements of sodium current induced by cumulative doses of ATP on P2 epithelial cells from CF patients.....	67
24. Measurements of chloride current with cumulative doses of ATP ranging from 10^{-9} M to 10^{-4} M.....	70
25. Measurements of chloride current with single dose of ATP ranging from 10^{-6} M to 10^{-4} M.....	70
26. Measurements of chloride current with cumulative doses of ATP ranging from 10^{-6} M to 10^{-4} M.....	72
27. Quantitative analysis of the chloride current measurement with a single dose of ATP.	73
28. Quantitative analysis of the chloride current measurement with cumulative doses of ATP.....	74
29. Cumulative dose-response curves for sodium current with ATP induced by ATP (10^{-9} M to 10^{-4} M) on P1 cultures of CF bronchial epithelial cells.....	74
30. Measurements of sodium current measurement with a single apical dose of ATP on CF epithelial cells.....	76
31. Quantitative analysis of the sodium current measurement with single dose of ATP on P2 CF epithelial cells.....	76
32. Sodium current measurements with cumulative doses of ATP on apical surface of CF epithelial cells.....	77
33. Quantitative analysis of the data from sodium current measurement with cumulative doses of ATP.....	77

34. Single dose–response of mixed current ($I_{Na+I_{Cl}}$) to ATP ranging from 10^{-6} M to 10^{-4} M on P2 epithelial cells.....	78
35. Measurement of sodium current induced by various doses of ATP on P0 (A, B, C), P1 (D, E, F) and P2 (G, H, I) cultures of bronchial epithelial cells...	80
36. Measurements of chloride current induced by various doses of ATP on P0 (A, B, C), P1 (D, E, F) and P2 (G, H, I) cultures of bronchial cells.....	81
37. Measurements of chloride current and mixed current induced by various doses of UTP on P2 human epithelial cells.....	82
38. Measurements of sodium current measurements induced by various doses of UTP on H441 cells.....	82
39. Hypertonic saline test on the ion/water transport model with parameters from CF airways.....	88

ABBREVIATION

AC	Adenylyl cyclase
ADO	Adenosine
ADP	Adenosine diphosphate
AMP	Adenosine monophosphate
AP	Alkaline phosphatase
ASL	Airway surface liquid
ATP	Adenosine triphosphate
CaCC	Calcium-activated chloride channel
cAMP _i	Intracellular cyclic-AMP
CF	Cystic fibrosis
CFTR	Cystic fibrosis transmembrane regulator
CNT	Concentrative Na ⁺ -dependent nucleoside transporter
DAG	Diacylglycerol
Ecto-AK	Ecto-adenylate kinase
Ecto 5'-NT	Ecto 5'-nucleotidase
ENaC	Epithelial sodium channel
E-NPP	Ecto-nucleotide pyrophosphatase/phosphodiesterase
HBE	Human bronchial epithelial
HPLC	High-performance liquid chromatography
HNE	Human nasal epithelial
KBR	Krebs-bicarbonate ringer
MTE	Murine tracheal epithelial
INO	Inosine
IP ₃	Inositol 1, 4, 5-trisphosphate

MCC	Mucociliary clearance
NS AP	Non-specific alkaline phosphatase
ENTPDase	Ecto-nucleoside triphosphate diphosphohydrolase
PCL	Periciliary layer
PIP ₂	Phosphatidylinositol 4, 5-biosphosphate
PKA	Protein kinase A
PKC	Protein kinase C
PLC	Phospholipase C
UTP	Uridine triphosphate

CHAPTER 1

INTRODUCTION

1.1 HISTORY AND MOTIVATION

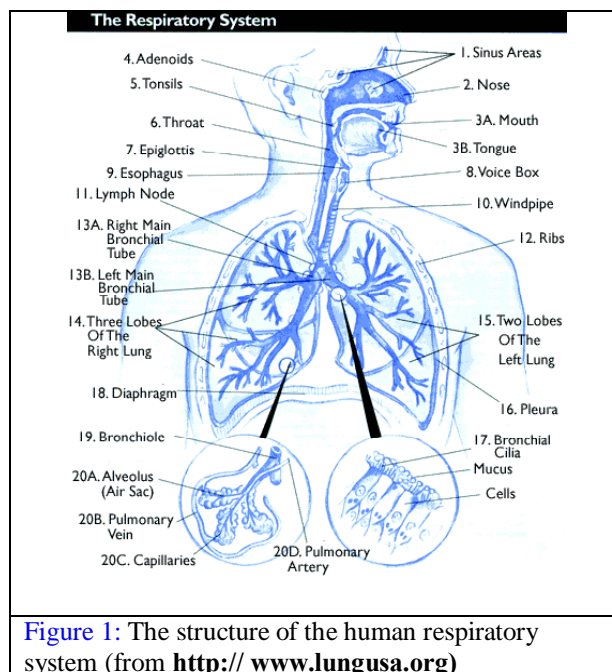
The principal function of the human lung is to transport oxygen from the atmosphere into the bloodstream, and to excrete carbon dioxide from the bloodstream into the atmosphere. Respiration occurs in a series of steps. Air is brought into the body via the airways, from the nose to the pharynx, the larynx, the trachea, bronchi, bronchioles and the alveolar sacs forming the terminal branches of the respiratory tree ([Figure 1](#)). The exchange of gases is accomplished by the sacs of specialized cells that form millions of tiny, exceptionally thin-walled air sacs called alveoli.

The airways also present natural defense mechanisms against infections. The ciliated epithelial surfaces of the airways are shielded by a mucus layer which traps inhaled particles and is continuously removed from the airways by ciliary beating activity. The mucus, secreted by superficial epithelium and goblet cells, is normally clear and thick filtering air during inhalation. During times of infection, mucus can change color as a result of trapped bacteria, while in some other diseases such as cystic fibrosis, a consistency change can occur due to water loss and high salt concentrations.

Lung disease is the number three killer in America, responsible for one in seven deaths. Along with other breathing problems, it is also the number one killer of babies younger than one year. Today, more than 35 million Americans are living with chronic

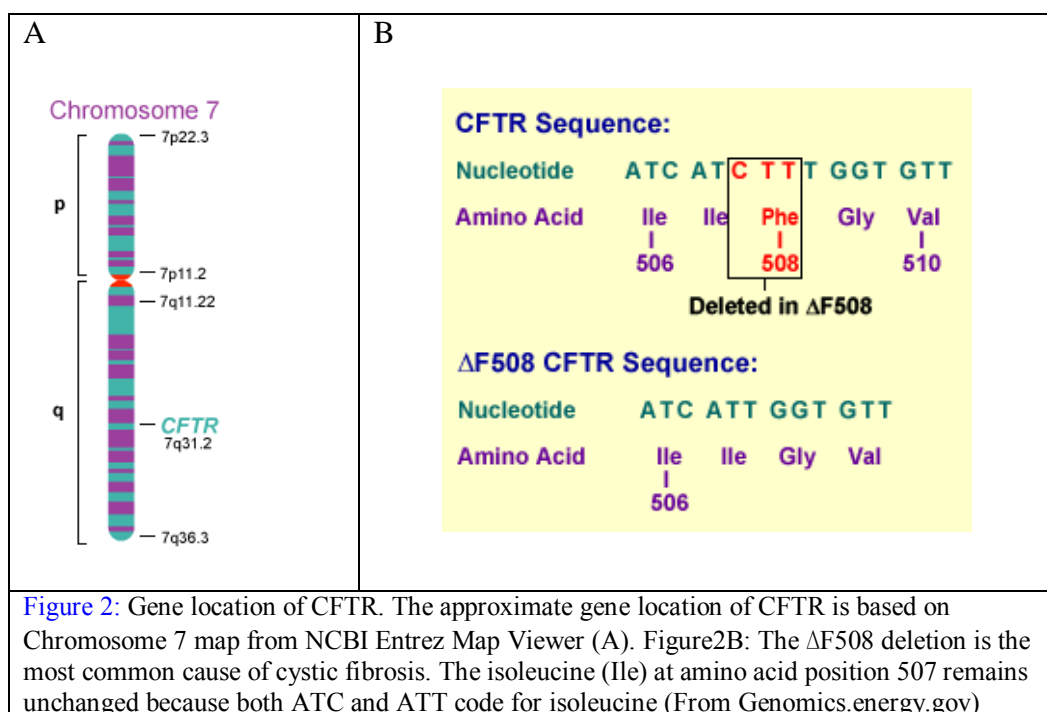
lung diseases such as asthma, emphysema and chronic bronchitis. In this dissertation, our focus is the lung disease called cystic fibrosis.

In medieval folklore, infants with salty skin, a symptom of cystic fibrosis, are



considered "bewitched" because they routinely die an early death. As sciences advanced, more about this disease has gradually been revealed. Cystic fibrosis (CF) is an inherited chronic disease that affects the lungs and digestive systems of about 30,000 children and adults in the United States (70,000 worldwide). It is most prevalent amongst European and Ashkenazi Jews. One in twenty-two people of European descent carries one gene for CF, making it the most common genetic disease among them. CF does not follow the same pattern in all patients but affects different people in different ways and to varying degrees. It affects the entire body, but symptoms begin mostly in the lungs. Some common symptoms include coughing, repeated lung infections, shortness of breath, poor growth, intestinal blockage, and infertility, all dominated by functional abnormalities in the glands that produce or secrete sweat and mucus. Sweat cools the body; mucus lubricates the respiratory, digestive, and reproductive systems and prevents tissues from

drying out, protecting them from infection. The lungs of CF patients produce excess thick, sticky mucus that clogs the airways, causing breathing problems and providing a breeding ground for bacteria to grow, which leads to frequent lung infections, damages to the lungs and contributes to early death. Thick fluid may also clog pancreatic ducts and prevent digestive fluids from reaching the small intestine, which causes digestive problems and slows growth. The conventional treatments for CF-related lung complications are chest percussion or other ways of clearing mucus. Antibiotics are often used to fight infection. There is no cure for CF and most patients die young – many in their 20s and 30s from lung failure. A Lung transplant is often necessary as CF progresses. Besides the conventional treatments, scientists are also working on finding a gene-based therapies based on the identification of CF gene two decades ago.



The identification of cystic fibrosis disease is traced back to the 1930s when it was first referred to as “cystic fibromatosis with bronchiectasis”. Andersen *et al.* developed the first comprehensive description of cystic fibrosis symptoms in 1938. About fifteen years later di Sant’ Agnese formally reported excessive amounts of salt in the CF

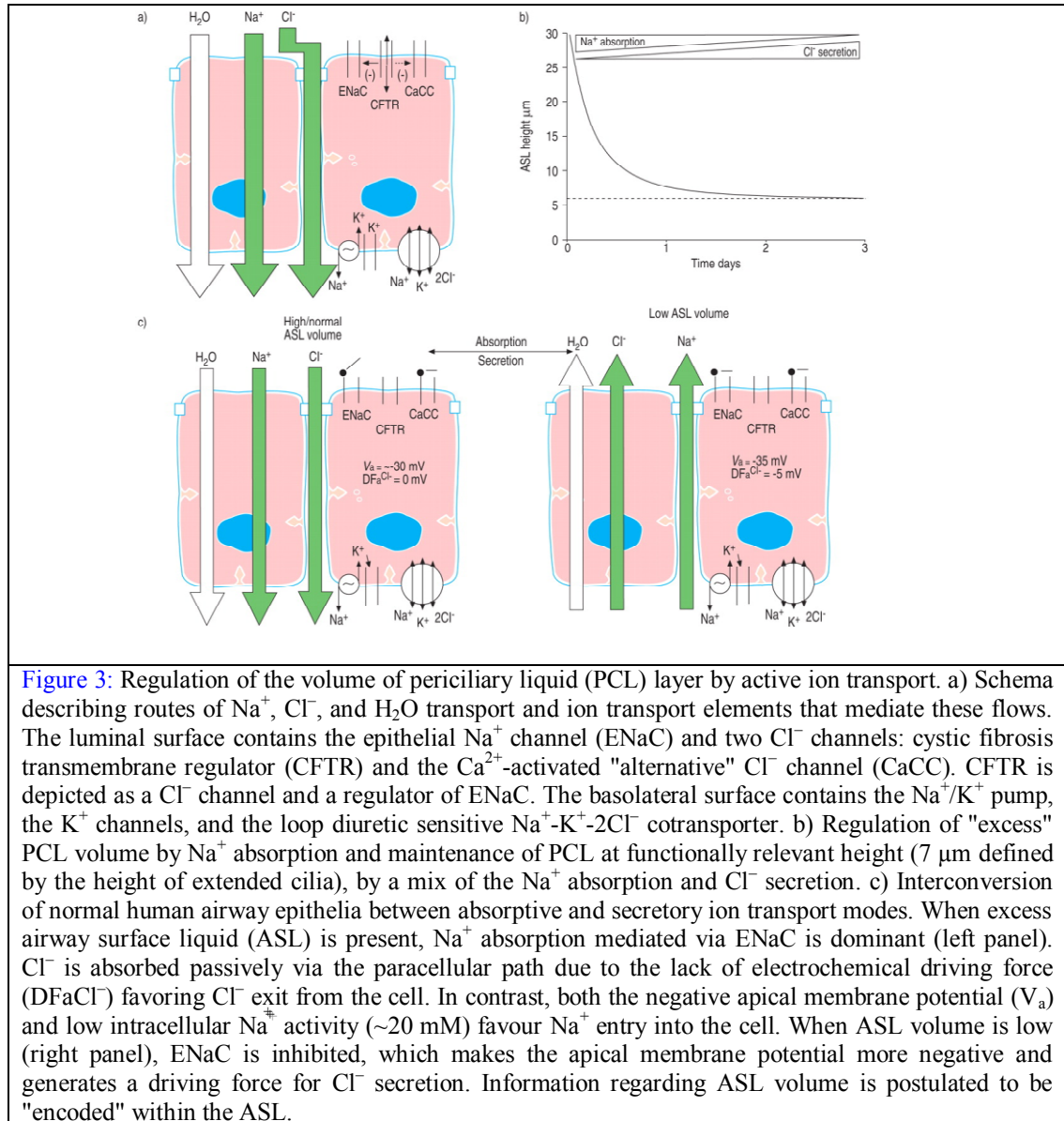
patients' sweat. In 1985, Tsui and co-workers [1, 2, 3] discovered the gene responsible for CF and named its protein product "Cystic Fibrosis Transmembrane Conductance Regulator (CFTR)" which was mapped to the long arm of chromosome 7q (Fig2A). Both copies of the gene need to be defective for a person to develop the disease. CFTR is an essential protein found in the epithelial cells that line the body's internal passageways, including the lungs, pancreas, colon, and genitourinary tract. It is responsible for moving chloride ions (Cl⁻) through the cell membrane. In 70% to 80% of all CF cases, three of the base pairs in the gene are deleted and the amino acid that the triad codes for (phenylalanine) is not generated. The abnormal protein is called $\Delta F508$ CFTR (Fig2B). The other 20% to 30% of CF cases result from one of hundreds of other possible mutations that can lead to abnormal CFTR function.

The finding of the CF gene makes gene therapy a natural candidate for treatment of cystic. Gene therapy is the insertion of genes into an individual's cells and tissues to treat a disease. Cystic fibrosis ultimately could be cured if safe and effective methods are found to replace the defective CFTR gene with an intact gene in affected tissues. In the case of cystic fibrosis, gene therapy would involve inhaling a spray that delivers normal DNA to the lung. During such a treatment, shuttle vehicles called vectors deliver a functional copy of the defective gene-in this case, CFTR-either to cells throughout the airways. Once the new CFTR gene has entered the cell, the biochemical machinery must recognize it and use it as a template for the production of functional protein. However, despite an impressive amount of research in this area, there is little evidence to suggest that an effective gene-transfer approach for the treatment of CF lung disease is imminent. The inability to produce such a therapy reflects in part the learning curve with respect to vector technology and the failure to appreciate the capacity of the airway epithelial cells

to defend themselves against the penetration by moieties, including gene-therapy vectors, from the outside world.

Meanwhile, the general recognition that CF lung disease reflects a failure of the innate defense of airways against bacterial infection leads to a search focusing on identifying the nature of the normal innate defense of the airways against bacterial infections and how mutations in the CF transmembrane conductance regulator (CFTR) gene perturb these mechanisms. It is generally believed that airway surface dehydration produces leads to mucus adhesion, inflammation and bacterial biofilm formation [4, 5, 6]. The characterization of well-differentiated cultures of airway epithelial cell culture revealed that the airway surface liquid (ASL) is divided into a well-defined periciliary liquid (PCL) layer and a mucus layer. Recent studies have shown that liquid can be added to, or removed from, the mucus layer without altering the height of the PCL layer. Specifically, the studies showed that removing approximately 50% of the liquid from the ASL compartment led to selective reduction in the volume of the mucus layer, with preservation of the PCL layer, and at least partial preservation of mucus transport. Conversely, when the ASL volume was doubled, liquid entered the mucus layer, the PCL layer maintained its volume, and interestingly, the mucus transport rates increased. Further studies revealed that when 70% or more of the volume was removed from the ASL compartment, the mucus layer could no longer effectively “donate” liquid to the PCL layer, volume was lost from the PCL, and mucus transport ceased. The upper limit of volume addition to the mucus layer was not determined in these studies. One implication of these findings is that as liquid *in vivo* converges onto a single airway from two smaller airways, the excess liquid deposited on the single airway from two distal airways may be transiently “stored” in the mucus layer, with preservation of PCL layer height and mucus transport. Presumably the excess liquid (salt and water) will be

removed by transepithelial ion transport from the mucus layer as the ASL moves up the single airway. In contrast, when water loss occurs at the surface of proximal airways due to exercise-induced evaporation, the volume is selectively lost from the mucus layer, with preservation of PCL and mucus transport.



Despite the good understanding of the role of the mucus layer as a reservoir, there are still surprisingly large gaps in our knowledge of the physiology and biophysics of this layer. For example, it is still not clear how this layer is formed *in vivo*, nor, what are the processes that maintain it as a physical layer. Older theories, suggesting that the mucus

layer was created by the thixotropic¹ action of beating cilia, appear to be inaccurate.

There are very likely important phase transitions that occur as a function of the concentration of the gel-forming mucins in ASL. Furthermore, as noted above, it is not known what the water storage capacity of the mucin layer is, or the biophysical principles that govern the capacity of this layer to absorb or donate liquid. Finally, it's not yet clear how the addition of liquid to airway surfaces increases mucus transport, as the biophysical properties of the mucus layer may be less important than the properties of the PCL layer.

The principal determinant of ASL volume is the mass of the salt on the airway surface [7]. This fact reflects the highly water permeable nature of the airways epithelium, that rapidly restores/maintains ASL volume in a near-isotonic state [8]. The mass of salt in the ASL is determined in part by the movement of liquid along epithelial surfaces and in part by the active ion transport mechanisms located within that airway region. Recent studies have emphasized the importance of the role of the PCL layer volume (height) in the maintenance of effective mucus clearance. A useful model for studying PCL physiology has been the well-differentiated culture that has had the mucus layer removed and a volume of liquid that mimics the properties of PCL placed on its surface. A convenient paradigm has been to start experiments with an “excess” of PCL that might mimic the height found at the convergence point of two airways. As shown in [Figure 3](#), normal human airway epithelia absorb rapidly the excess PCL. But as the PCL layer approaches physiology height (7μm), active volume absorption ceases and a steady state is reached.

Since the original detection of a raised potential difference (PD) across CF airway epithelia *in vivo* [9], there has been the notion that abnormal electrolyte transport is a key

¹ Thixotropic, adjective form of thixotropy. Thixotropy is the property of various gels of becoming fluid when disturbed (as by shaking)

component of CF lung pathogenesis. Early PD studies detected an increase in the amiloride²-sensitive component of the PD, which suggested an accelerated Na⁺ transport. However, the PD measurements also detected a failure to secrete Cl⁻ ions, under basal conditions and β -adrenergic³ stimulation, which predicted a second defect [10].

Subsequent studies with freshly excised tissues and cultured cells established evidence for both Na⁺ transport (upregulated) and Cl⁻ transport (downregulated) defects in CF airway epithelia compared with normal cell cultures. It suggested that the CFTR protein has a dual function in airway epithelia, i.e., to conduct Cl⁻ ions and to regulate Na⁺ channel. The absence of CFTR thus causes an up-regulation of Na⁺ absorption through ENaC and a failure of Cl⁻ secretion via CFTR. This finding lead to novel therapeutic approaches for the CF lung disease. Other than conventional anti-infective and the anti-inflammatory drugs, the alternative approach is to restore normal ion transport properties in CF airway epithelia. Compounds that appear to possess actions that inhibit excessive Na⁺ transport and trigger Cl⁻ secretion are nucleoside triphosphates: ATP or UTP. They interact with specific receptors on apical epithelial surfaces and activate signaling pathways leading to the inhibition of ENaC-mediated Na⁺ absorption and stimulation of Ca²⁺-activated Cl⁻ secretion by CaCC in normal and CF airway epithelia [11, 12, 13]. These cellular responses cause liquid efflux and an increase in ASL volume on CF airway epithelia. Similarly, recent data suggest that the local formation of adenosine, a dephosphorylation product of ATP interacting with A_{2B} receptors on the apical surface, stimulates the activity of CFTR.

Extracellular nucleoside triphosphates and nucleosides not only participate in signaling transduction processes on airway surfaces, but are also actively regulated by

² Amiloride blocks the epithelial sodium channel (ENaC) thereby inhibiting sodium reabsorption in the distal convoluted tubules and collecting ducts in the kidneys.

³ β -adrenergic³ receptors are a class of G protein-coupled receptors. They stimulate chloride secretion in epithelial cells.

various enzymes in the ASL. Because ASL ATP and UTP concentrations affect Na^+ and Cl^- currents, and thus PCL height, we can think of the biochemical network involving the nucleotides (ATP and/or UTP) and their dephosphorylated products as an electronic circuit regulating mucociliary clearance. Because the enzymes that catalyze nucleotide metabolism have been identified and biochemically characterized, an emerging idea is to develop a predictive mathematical model that describes in detail the behavior of this biochemical network, and then couple it to a model of ion conductances across the epithelium.

1.2 OUTLINE

This dissertation consists of three major parts: the biochemical network model that describes the degradation of ATP, the ion and water transport model, and results from electrophysiological experiments that are required to couple the two models. Chapter 1 gives a brief introduction on the physiological background of this problem. Chapter 2, 3 and 4 cover each of the three topics respectively. Chapter 2 mostly focuses on the biochemical network in a homogenous solution. However, we also discuss some results from a spatial model of this network to address some interesting characteristics of ATP regulation in the ASL and its potential application in pharmacological drug study of cystic fibrosis.

CHAPTER 2

EXTRACELULLAR NUCLEOTIDE AND NUCLEOSIDE METABOLISM

2.1 INTRODUCTION

Mucociliary clearance (MCC) constitutes the first line of defense against the establishment of chronic airway infection. Inhaled pathogens are intercepted by a mucin layer, maintained above ciliated epithelia by a periciliary (PCL) layer. Together, mucin and PCL form the ASL, which is continuously displaced upward by cilia beating activity. In lung diseases, like cystic fibrosis and primary cilia dyskinesia, dysfunctional MCC leads to severe complications related to airway obstruction and tissue damage by inflammatory responses to persistent infections [14,15]. Adenine nucleotides have been shown to stimulate all major epithelial functions supporting MCC through cell surface P2 receptors: electrolyte/ water efflux by ENaC to maintain optimum ASL height [15], mucus secretion [16,17] and cilia beating activity [18, 19]. They are secreted by the epithelium under basal conditions [20, 21] and at higher rates in response to mechanical stress such as pathogen interaction, rhythmic breathing or coughing [21- 24]. Nucleotide-mediated epithelial responses are terminated by cell surface enzymes converting ATP into adenosine [26- 28]. This nucleoside initiates a second wave of signaling through A_{2B} receptor-mediated cilia beating [29] and ion/water efflux by the cystic fibrosis transmembrane regulator (CFTR) [30].

Despite the importance of this regulatory system for airway defenses, it has not been possible to design a mathematical model to describe this system due to the

unavailability of quantitative information regarding ASL nucleotide concentrations and release rates, as well as the kinetic properties of the enzymes and uptake mechanisms. In the past decade, extensive work has been conducted to characterize basal and stimulated ATP release on human airway epithelia [20, 21, 23-25, 32, 33]. In addition, members from all three families of ectoATPases [ecto-nucleoside triphosphate diphosphohydrolases (E-NTPDases), alkaline phosphatases (APs) and ecto-nucleotide pyrophosphatase/phosphodiesterases (E-NPPs)] [34,35] have been identified on the apical surface of human bronchial epithelial cells [26-28,36-38], along with an ecto-adenylate kinase (Ecto-AK; $2\text{ADP} \leftrightarrow \text{ATP} + \text{AMP}$) [39,40]. The enzymes supporting the conversion of AMP to adenosine were identified as ecto 5'-nucleotidase (Ecto 5'-NT) and non-specific alkaline phosphatase (NS AP) [26], whereas airway adenosine is eliminated by adenosine deaminase 1 and concentrative nucleoside transporters (CNT2 and CNT3) [41].

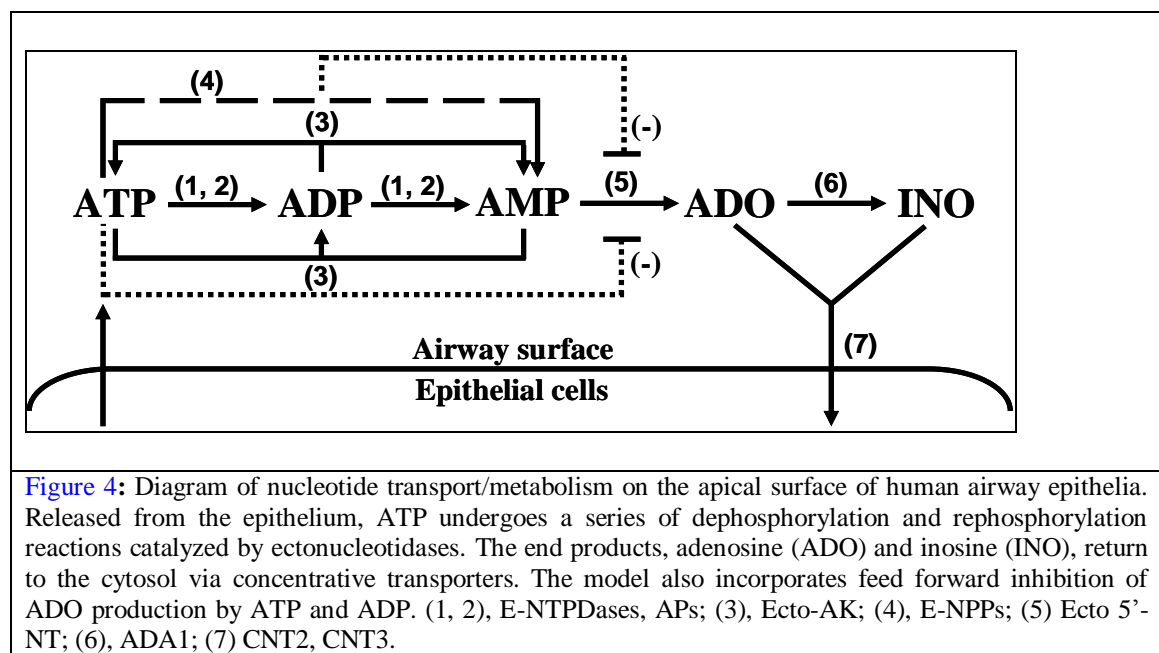
A mathematical model of nucleotide regulation on the apical surface of human airway epithelia was built based on the above empirical data. The kinetic coefficients were optimized by fitting the model's output to experimental parameters of ATP metabolism [26,38,40], adenosine/ inosine uptake [41], nucleotide release and cell surface concentrations [25,32] . Sensitivity analyses reproduced major aspects of airway nucleotide regulation, including the respective contributions of high- and low-affinity ectonucleotidases to the regulation of steady-state and transient nucleotide concentration. This study provides a first mathematical approach to the investigation of an important defense mechanism in human airways.

2.2 METHODS

Functional Measurements of ATP Levels and Metabolism

The model was validated by functional assays conducted on polarized primary

cultures of human bronchial epithelial cells grown at air-liquid interface, as previously described [42]. Steady-state ATP levels were measured by luminometry using soluble luciferase or chimeric *Staphylococcus aureus* protein A-luciferase (SPA-luc) attached to antigens on the epithelial surface [32]. The time-courses of ATP metabolism were obtained from high-performance liquid chromatography (HPLC) analysis of apical buffer samples collected over time after the addition of 1-1000 μ M ATP to the apical surface [27]. The kinetic parameters of airway NS AP for ATP and ADP were obtained as we previously described for AMP [26] in the presence of 0.5 mM Ap₅A to prevent transphosphorylation events through ecto-AK activity [30].



Kinetic Model of Airway ATP /Adenosine Regulation

This section outlines the theory and methodology behind the mathematical model designed to simulate nucleotide regulation on the apical surface of human airway epithelia. A biochemical network was derived using quantitative information gathered from the literature on nucleotide release [25,32] and metabolism [26-28,36,38] by cultured human bronchial epithelial cells (Figure 4). Because UTP levels are about 15%

that of ATP [43] in the ASL, the influence of uridine nucleotides on ATP metabolism was considered negligible. Therefore, the reactions supporting ATP dephosphorylation to adenosine and adenosine deamination are:



Michaelis-Menten kinetics is used to model these reaction rates, in the form:

$$\text{reaction rate} = \frac{V_{\max,j}[S]}{K_{M,j} + [S]} \quad (2.6)$$

where [S] is the substrate concentration, and $V_{\max,j}$ and $K_{M,j}$ designate the maximum reaction velocity and Michaelis constant, respectively. Because several reactions are catalyzed by more than one enzyme, the subscript j is used to index the multiple enzymes. Adenosine and inosine uptake by CNTs also follows Michaelis-Menten kinetics [41]. In contrast, the reversible Ecto-AK reaction:



which involves two substrates, was assumed to follow a Ping-Pong mechanism [44]:

$$\text{reaction rate} = \frac{V_{\max,forward}}{1 + K_{ATP}/[ATP] + K_{AMP}/[AMP]} - \frac{V_{\max,backward}}{1 + 2K_{ADP}/[ADP]} \quad (2.8)$$

The Ping-Pong mechanism is a generalization of Michaelis-Menten kinetics that relies on the same underlying assumptions.

Experimental evidence indicates that ATP and ADP competitively bind to enzymes that catalyze AMP dephosphorylation [26,45]. The following equation was used to model this effect:

$$\text{reaction rate} = \frac{V_{\max,j} [AMP]}{K_{M,j} \left(1 + \frac{[ATP]}{K_{i,ATP}} + \frac{[ADP]}{K_{i,ADP}} \right) + [AMP]} \quad (2.9)$$

Although it is possible that the inhibition constants $K_{i,ATP}$ and $K_{i,ADP}$ may differ for ecto 5'-NT and NS AP, a single value was assigned for simplicity.

The remaining elements to incorporate into the model are the rate of ATP release and steady-state ASL nucleotide concentrations. In accordance with experimental observations [25], the basal (unstimulated) rate of ATP release (J_{ATP}) was considered constant. However, one of the functions of nucleotide release is to stimulate fluid efflux, which in turn, may affect ASL nucleotide concentrations. Under steady-state conditions, while basal release rates do not sustain ATP levels sufficiently high to activate P2 receptors, the steady-state adenosine level generated from ATP metabolism stimulates fluid efflux into the ASL by the A_{2B} receptor-CFTR pathway [30]. The equation was therefore derived to take into account time-dependent ASL volume changes during basal ATP release. We considered this case in which ATP is released into the ASL layer at a rate of J_{ATP} molecules per second and then hydrolyzed by enzyme E. The surface area of the epithelium is denoted by A, and $[E]_T$ represents the surface density of E generally expressed in moles/cm². If V indicates the volume, the equation governing ASL ATP concentration is:

$$\frac{d[ATP]}{dt} = \frac{J_{ATP}}{V} - \frac{\frac{K_{cat}A}{V} [E]_T [ATP]}{K_M + [ATP]} - \frac{[ATP]}{V} \frac{dV}{dt} \quad (2.10)$$

where the last term in the equation models changes in ATP concentration due to the changing volume. The fact that ATP flux and V_{\max} , designated by $k_{cat} (A/V) [E]_T$, scale inversely with volume predicts that steady-state ATP levels are independent of ASL

volume. The biochemical steps describing ASL nucleotide metabolism are modeled by the equations:

$$\begin{aligned} \frac{d[ATP]}{dt} = \frac{1}{V} & \left(J_{ATP} - \frac{V_{\max}^{(1)}[ATP]}{K_M^{(1)} + [ATP]} - \frac{V_{\max}^{(2)}[ATP]}{K_M^{(2)} + [ATP]} - \frac{V_{\max}^{(3)}[ATP]}{K_M^{(3)} + [ATP]} - \frac{V_{\max}^{(10)}[ATP]}{K_M^{(10)} + [ATP]} \right. \\ & \left. - \frac{V_{\max,forward}}{1 + \frac{K_{ATP}}{[ATP]} + \frac{K_{AMP}}{[AMP]}} + \frac{V_{\max,backward}}{1 + \frac{2K_{ADP}}{[ADP]}} - [ATP] \frac{dV}{dt} \right) \end{aligned} \quad (2.11)$$

$$\begin{aligned} \frac{d[ADP]}{dt} = \frac{1}{V} & \left(\frac{V_{\max}^{(1)}[ATP]}{K_M^{(1)} + [ATP]} + \frac{V_{\max}^{(2)}[ATP]}{K_M^{(2)} + [ATP]} + \frac{V_{\max}^{(3)}[ATP]}{K_M^{(3)} + [ATP]} - \frac{V_{\max}^{(4)}[ADP]}{K_M^{(4)} + [ADP]} - \frac{V_{\max}^{(5)}[ADP]}{K_M^{(5)} + [ADP]} \right. \\ & \left. + \frac{2V_{\max,forward}}{1 + \frac{K_{ATP}}{[ATP]} + \frac{K_{AMP}}{[AMP]}} - \frac{2V_{\max,backward}}{1 + \frac{2K_{ADP}}{[ADP]}} - [ADP] \frac{dV}{dt} \right) \end{aligned} \quad (2.12)$$

$$\begin{aligned} \frac{d[AMP]}{dt} = \frac{1}{V} & \left(\frac{V_{\max}^{(4)}[ADP]}{K_M^{(4)} + [ADP]} + \frac{V_{\max}^{(5)}[ADP]}{K_M^{(5)} + [ADP]} + \frac{V_{\max}^{(10)}[ATP]}{K_M^{(10)} + [ATP]} - \frac{V_{\max,forward}}{1 + \frac{K_{ATP}}{[ATP]} + \frac{K_{AMP}}{[AMP]}} + \frac{V_{\max,backward}}{1 + \frac{2K_{ADP}}{[ADP]}} \right. \\ & - \frac{V_{\max}^{(6)}[AMP]}{K_M^{(6)} \left(1 + \frac{[ATP]}{K_{i,1}} + \frac{[ADP]}{K_{i,2}} \right) + [AMP]} - \frac{V_{\max}^{(7)}[AMP]}{K_M^{(7)} \left(1 + \frac{[ATP]}{K_{i,1}} + \frac{[ADP]}{K_{i,2}} \right) + [AMP]} \\ & \left. - \frac{V_{\max}^{(8)}[AMP]}{K_M^{(8)} \left(1 + \frac{[ATP]}{K_{i,1}} + \frac{[ADP]}{K_{i,2}} \right) + [AMP]} - [AMP] \frac{dV}{dt} \right) \end{aligned} \quad (2.13)$$

$$\begin{aligned} \frac{d[ADO]}{dt} = \frac{1}{V} & \left(- \frac{V_{\max}^{(9)}[ADO]}{K_M^{(9)} + [ADO]} - \frac{V_{i,1}[ADO]}{K_{i,1} + [ADO]} + \frac{V_{\max}^{(6)}[AMP]}{K_M^{(6)} \left(1 + \frac{[ATP]}{K_{i,1}} + \frac{[ADP]}{K_{i,2}} \right) + [AMP]} \right. \\ & + \frac{V_{\max}^{(7)}[AMP]}{K_M^{(7)} \left(1 + \frac{[ATP]}{K_{i,1}} + \frac{[ADP]}{K_{i,2}} \right) + [AMP]} + \frac{V_{\max}^{(8)}[AMP]}{K_M^{(8)} \left(1 + \frac{[ATP]}{K_{i,1}} + \frac{[ADP]}{K_{i,2}} \right) + [AMP]} \\ & \left. - [ADO] \frac{dV}{dt} \right) \end{aligned} \quad (2.14)$$

$$\frac{d[INO]}{dt} = \frac{1}{V} \left(\frac{V_{\max}^{(9)}[ADO]}{K_M^{(9)} + [ADO]} - \frac{V_{i,2}[INO]}{K_{i,2} + [INO]} - [INO] \frac{dV}{dt} \right) \quad (2.15)$$

The independence of nucleotide concentrations on ASL volume under steady-state conditions, determined by setting time derivatives to zero, was verified by simulations and functional assays. The model predicts that an increase in ASL volume acutely reduces

ATP and ADP concentrations, followed by a rapid return to steady-state levels (Figure 5A). This model feature was validated experimentally using cultures of human bronchial epithelial cells (Figure 5B). Steady-state ATP levels, measured 60 min after the addition of 10-500 μ l phosphate-buffered saline to the apical surface [32], were not affected by liquid volume.

When fitting the model, random sets were generated using a multivariate Gaussian distribution with means equal to the experimental data and standard deviations equal to 25% of the mean. These parameter sets were used as initial guesses in MATLAB nonlinear least square routines. After the modeling fitting, the estimated parameter sets are collected and residuals are compared (Table 1). A set that corresponds with the minimum residual is chosen to be the best fitting.

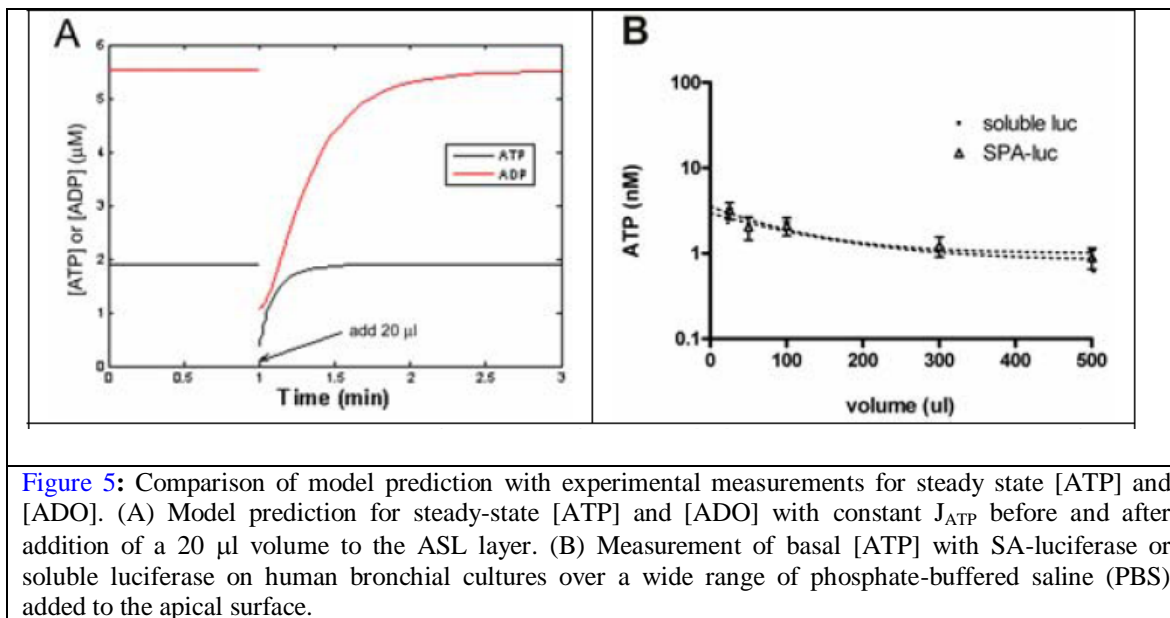


Figure 5: Comparison of model prediction with experimental measurements for steady state [ATP] and [ADO]. (A) Model prediction for steady-state [ATP] and [ADO] with constant J_{ATP} before and after addition of a 20 μ l volume to the ASL layer. (B) Measurement of basal [ATP] with SA-luciferase or soluble luciferase on human bronchial cultures over a wide range of phosphate-buffered saline (PBS) added to the apical surface.

Linear Model for the Steady-State Nucleotide Concentrations

Experimental observations indicated that, under physiological conditions, steady-state nucleotide concentrations are orders of magnitude lower than the K_M values of the

enzymatic reactions [25]. Therefore, to a good approximation, the Michaelis-Menten reaction rates can be simplified (linearized) as follows:

$$\sum_j \frac{V_{\max,j}^{(k)} [S]}{K_{M,j}^{(k)} + [S]} \sim \left(\sum_j \frac{V_{\max,j}^{(k)}}{K_{M,j}^{(k)}} \right) [S] = P^{(k)} [S] \quad (2.16)$$

where the parameter $P^{(k)}$ denotes the sum of the ratios of $V_{\max,j}^{(k)}$ to $K_{M,j}^{(k)}$ for all the enzymes that catalyze the same reaction. The expressions for adenosine and inosine uptake can be simplified in a similar way. Furthermore, model simulations revealed that the non-linear parameters, the reversible Ecto-AK reaction given in Eq.(2.9) and the inhibition of AMP hydrolysis by ATP and ADP (Table 1), do not significantly affect the steady-state behavior of the model (*data not shown*). They were, therefore, excluded from the linear model. Using these simplifications, Eq.(2.11) -(2.15) can be approximated under steady-state conditions by the following set of linear algebraic equations:

$$J - P_1 [ATP]_{ss} = 0 \quad (2.17)$$

$$P_1 [ATP]_{ss} - P_2 [ADP]_{ss} = 0 \quad (2.18)$$

$$P_2 [ADP]_{ss} - P_3 [AMP]_{ss} = 0 \quad (2.19)$$

$$P_3 [AMP]_{ss} - P_4 [ADO]_{ss} - U_1 [ADO]_{ss} = 0 \quad (2.20)$$

$$P_4 [ADO]_{ss} - U_2 [INO]_{ss} = 0 \quad (2.21)$$

where U_1 and U_2 result from linearizing the expressions for adenosine (Eq. (2.20)) and inosine (Eq. (2.21)) uptake, respectively.

Sensitivity Analysis

An important tool for analyzing differential equation models of biochemical pathways is sensitivity analysis. This technique determines the influence each parameter has on the system and identifies which components of the pathway can be perturbed to produce the

largest effect. Briefly, if the elements of the vector $\mathbf{x}(t)$ are solutions to the model equations:

$$\frac{d\mathbf{x}}{dt} = f(\mathbf{x}, t ; \mathbf{p}) \quad (2.22)$$

where the elements of the vector \mathbf{p} are the model parameters, the ratio

$$S_{i,j}(t) = \frac{\frac{\partial x_i(t)}{\partial p_j}}{\frac{x_i(t)}{p_j}} = \frac{\text{Percent change in } x_i(t)}{\text{Percent change in } p_j} \quad (2.23)$$

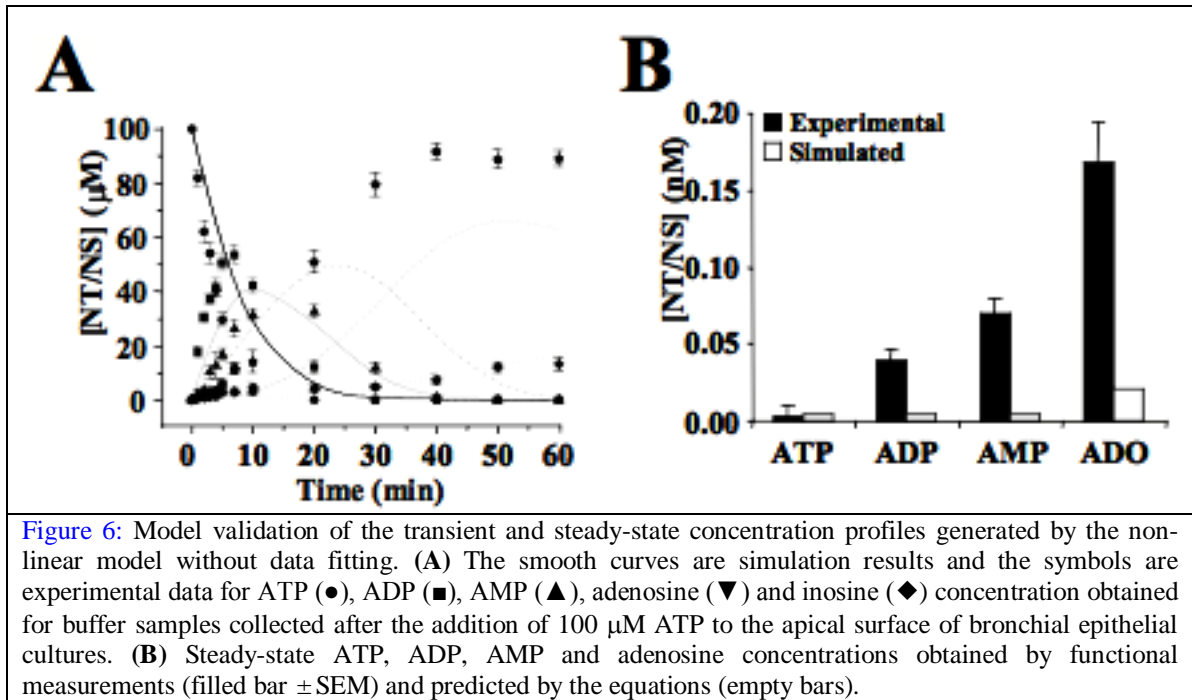
=is used as a measure of the sensitivity of the i^{th} model variable to perturbations in the j^{th} parameter value. The sensitivities $S_{i,j}(t)$ are time dependent and require knowledge of the quantity $\partial x_i(t)/\partial p_j$. The partial derivatives $\partial x_i(t)/\partial p_j$ satisfy a set of M by N differential equations that involve the time-dependent Jacobian of the model equations and the quantity $\partial f_i(\bar{\mathbf{x}}(t), t ; \bar{\mathbf{p}})/\partial p_j$. After determining the best parameter set for the non-linear model of ASL nucleotide regulation, sensitivity analyses were performed to test the importance of high- and low-affinity enzymes on the regulation of transient and steady-state concentration profiles, as well as the physiological relevance of the feed forward inhibition of adenosine production by ATP.

2. 3 RESULTS

Analysis of the Linear Steady-State Model

We started our investigations using the multi-component model shown in [Figure 4](#) and described by Eq.(2.11) -(2.15). Experimental measurements were available for all model parameters, except for the K_M of AMP hydrolysis by Ecto-AK (Eq.(2.8); k_{f12} in [Table 1](#)) and inosine uptake. Initially, these were taken as free parameters to fit time-dependent changes in nucleotide ASL concentrations after the addition of 100 mM ATP.

Under these conditions, considerable discrepancies were found between the model simulation and experimental data for both transient [Figure 6A] and steady-state [Figure 6B] concentration profiles.



The model was considerably improved by using the experimental data as initial guesses, then fitted using the nonlinear least square routine of the MATLAB software (Mathworks, Natick, MA). This simulation reproduced closely the transient (Figure 7A) and steady-state (Figure 7B) concentration profiles. Furthermore, among the 14 experimental V_{\max} , only two remained \geq 2-fold different from estimated values: the low-capacity ATPase activity (v1) and adenosine deamination (v9) (Table 1). However, large discrepancy (15-fold) persisted between measured and predicted rates of basal ATP release (Table 1). Comparable values were obtained by different research groups using various methods [23,25,32], thereby ruling out experimental error. On the other hand, if the rate of ATP

release was held fixed and the other parameters left free to be determined by fitting the data, the model reproduced the transient behavior of the system after the addition of 100 μM ATP (Figure 7C), but not the steady-state concentration profile (Figure 7D).

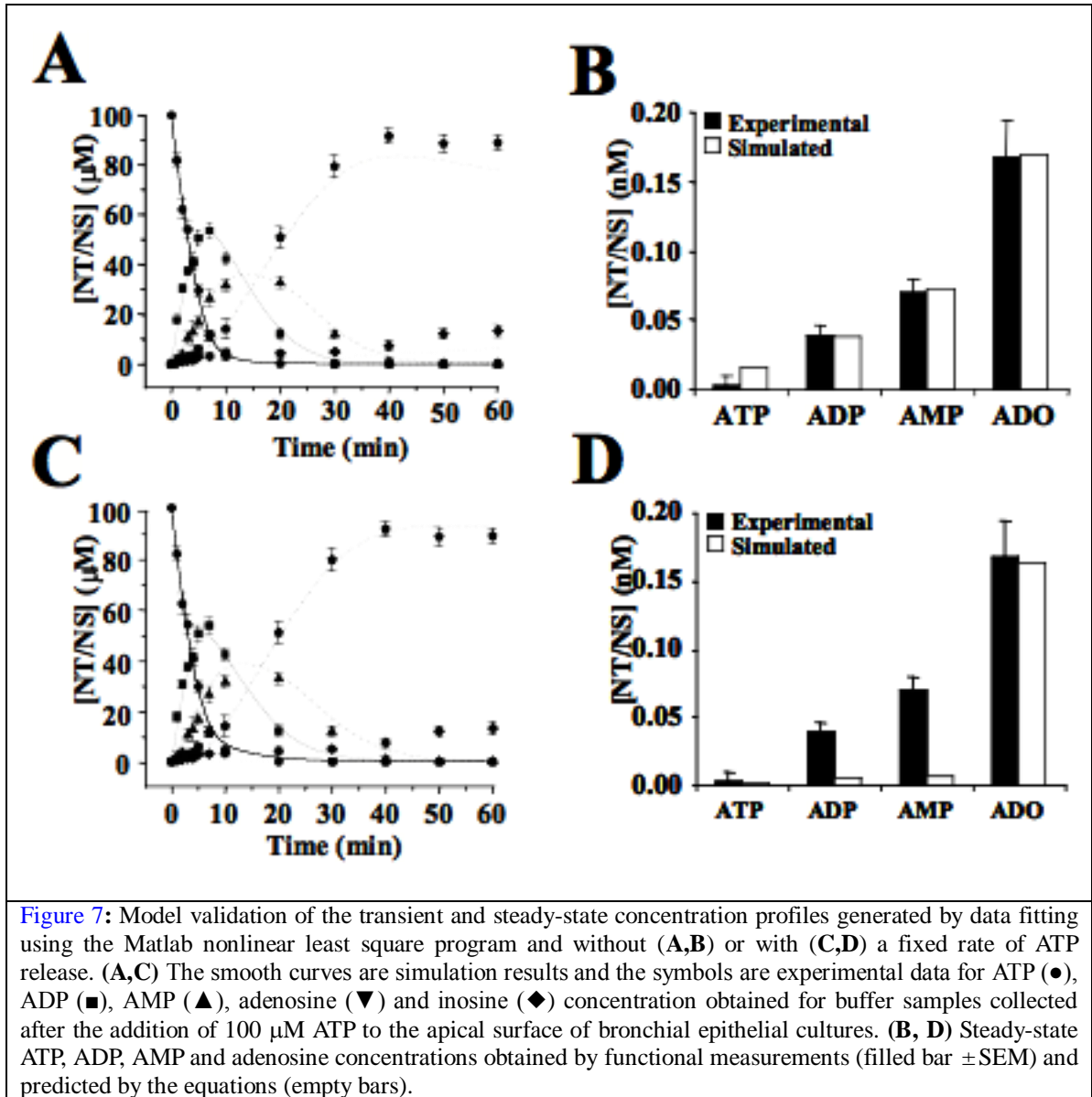


Figure 7: Model validation of the transient and steady-state concentration profiles generated by data fitting using the Matlab nonlinear least square program and without (A,B) or with (C,D) a fixed rate of ATP release. (A,C) The smooth curves are simulation results and the symbols are experimental data for ATP (●), ADP (■), AMP (▲), adenosine (▼) and inosine (◆) concentration obtained for buffer samples collected after the addition of 100 μM ATP to the apical surface of bronchial epithelial cultures. (B, D) Steady-state ATP, ADP, AMP and adenosine concentrations obtained by functional measurements (filled bar \pm SEM) and predicted by the equations (empty bars).

Model simulations were conducted to test whether the non-linear equations, describing ecto-AK (Eq.(2.8)) and the feed forward inhibition of AMP dephosphorylation (Eq.(2.9)), influence steady-state nucleotide concentrations. The forward and backward reaction rates

of Ecto-AK were approximated based on the 35-fold higher steady-state AMP concentration compared to ATP (Table 2), while the inhibition of AMP dephosphorylation still followed the nonlinear scheme given by Eq. (2.9). This manipulation did not influence the steady-state concentration profile. Therefore, we developed an approximate linear model to simulate steady-state nucleotide levels and the basal rate of ATP release (Eq. (2.17)-(2.21)). The simulation from nonlinear model suggested a minor contribution to the steady state from the reversible reaction, the inhibition of ATP and ADP to AMP hydrolysis and the reaction of ATP converting to AMP. Therefore these three mechanisms were neglected from the linear model.

We first calculated the reaction rate constants P_i 's and U_i 's in the linear model from the experimental measurements of the Michaelis Menten parameters. When these rate constants were plugged into the linear equations, this model was also inconsistent with the experimental rate of ATP release (Table 2). Then we tried the opposite approach by plugging the experimental level of all the metabolites except the unavailable INO level into the model and solving for parameter set. The ATP release rate and uptake rates of adenosine and inosine are assumed to be constant parameters in this procedure. When we used this rate constants derived from solving the linear equation to calculate the inosine concentration at steady state, we reached a negative value, which is biologically impossible (*data not shown*). Altogether, these maneuvers suggested that no choice of parameter values could capture the empirical data and raised the possibility that the model was missing a key component.

Reactions	Parameters	Experimental Data	REF	Estimations (No ADP-AMP release)	Estimations (ADP-AMP release)
ATP → ADP	v1 k1	2.1	[38]	8.2	5.1
	v2 k2	17	[38]	9.5	23.5
	v3 k3	8.1	[38]	12.2	15.0
	v4 k4	129	[38]	142.8	126.5
	v5 k5	16.8	[38]	23.5	22.6
ADP → AMP	v6 k6	405	[38]	415.2	313.9
	v7 k7	1.4	[38]	2.4	1.5
	v8 k8	8	[38]	6.4	4.9
	v9 k9	9.1	[38]	9.7	9.2
	v10 k10	94	[38]	114.0	90.6
AMP → ADO	v11 k11	1.8	[26]	2.0	2.7
	v12 k12	14	[26]	18.9	11.6
	v13 k13	4.2	[26]	5.6	5.3
	v14 k14	36	[26]	43.5	34.4
	v15 k15	9.8	[26]	12.5	12.9
ADO → INO	v16 k16	717	[26]	708.1	908.5
	v17 k17	0.8	[41]	0.2	0.5
	v18 k18	25	[41]	26.5	31.5
	v19 k19	0.9	[36]	1.2	1.4
	v20 k20	22	[36]	10.2	15.4
ATP + AMP → 2ADP	v21 k21	3.8	[40]	1.8	3.0
	v22 k22	23	[40]	21.6	34.6
	v23 k23	N/A	[40]	20.3	29.5
	v24 k24	1.8	[40]	1.3	1.3
	v25 k25	43	[40]	43.9	59.0
ATP + AMP ← 2ADP	v26 k26	0.0012	[25]	0.0183	0.0014
	v27 k27	N/A			0.0135
	v28 k28	N/A			0.0144
	v29 k29	0.45	[41]	0.3	0.3
	v30 k30	17.3	[41]	2.8	1.7
INO uptake	v31 k31	N/A			0.45
	v32 k32	N/A			11.6
	v33 k33	7	[40]	64.6	28.2
	v34 k34	10	[40]	57.5	33.1
	v35 k35				

Table 1: Comparison between parameters of ASL nucleotide release and metabolism functionally measured and estimated from the linear model without fitting or including parameters of ADP and AMP release. Unknown experimental values are labeled “N/A”. The units for V_{\max} and K_M are $\text{nmoles} \cdot \text{min}^{-1} \cdot \text{ml}^{-1}$ and μM , REF designates the references.

	ATP	ADP	AMP	ADO
Empirical data	2.2	38.7	70.2	168
Linear model	5.2	4.4	4.6	20.5
Linear model with ADP/AMP release	5.2	54.1	112.4	501.5

Table 2: Steady-state nucleotide concentrations calculated from the linear model without or with parameters of ADP and AMP release.

Predicted release of ADP and AMP

Our current knowledge of nucleotide release mechanisms is limited to ATP

because the ectonucleotidase inhibitor cocktail [32] interferes with measurements of ADP

and AMP by ethenyl derivatization and fluorescence chromatography (Lazarowski, E.R., pers. comm.). However, emerging studies suggest that mechanical stimulations induce the release of ATP, ADP and AMP through exocytosis as a general mechanism in mammalian cells, including polarized epithelia [17, 20]. During maturation, secretory vesicles accumulate ATP and UDP-sugars in concentrations up to 50-fold above cytosolic concentrations, which are converted to ADP and UDP, and eventually to AMP and UMP [47]. Therefore, vesicle fusion to the apical membrane would release ATP, ADP and AMP. These observations motivated the addition of terms describing ADP and AMP release to the mathematical model. Constant fluxes for ADP and AMP were added to the linear equations (Eq. (2.17)-(2.21)) and adjusted so that the model generated steady-state concentrations similar to the experimental data (Table 2). With these modifications, the model accurately captured the basal rate of ATP release and steady-state nucleotide concentrations, except for a two-fold higher adenosine concentration. Estimated release rates for ADP ($0.013 \mu\text{M} \cdot \text{min}^{-1}$) and AMP ($0.014 \mu\text{M} \cdot \text{min}^{-1}$) were ten-fold higher than for ATP, which would be consistent with their relative steady-state levels [88].

Reanalysis of the Full Model

This multi-enzyme model with nonlinear Michaelis-Menten kinetics (Eq.(2.11) -(2.15)) was revisited with the parameters of ADP and AMP release determined above. The new model closely reproduced both transient and steady-state behaviors. First, the predicted metabolic profile for $100 \mu\text{M}$ ATP followed closely the experimental data, except for a slight deviation in adenosine accumulation after 30 min (Figure 8A). This discrepancy is explained by the assumption of Michaelis-Menten kinetics, which requires the substrate concentration to be higher than the K_M of the reaction (Ecto 5'NT; $14 \mu\text{M}$, Table 1). Second, this model eliminated the 15-fold difference between measured and estimated

rates of ATP release (Figure 8B). Finally, this model provided the best fit of all V_{\max} and K_M values (Table 1), except for 2- to 3-fold differences in the feed-forward inhibition constants. Collectively, these data demonstrate that the mathematical model closely reproduces the complex biochemical network regulating adenine nucleotides on human airway epithelia.

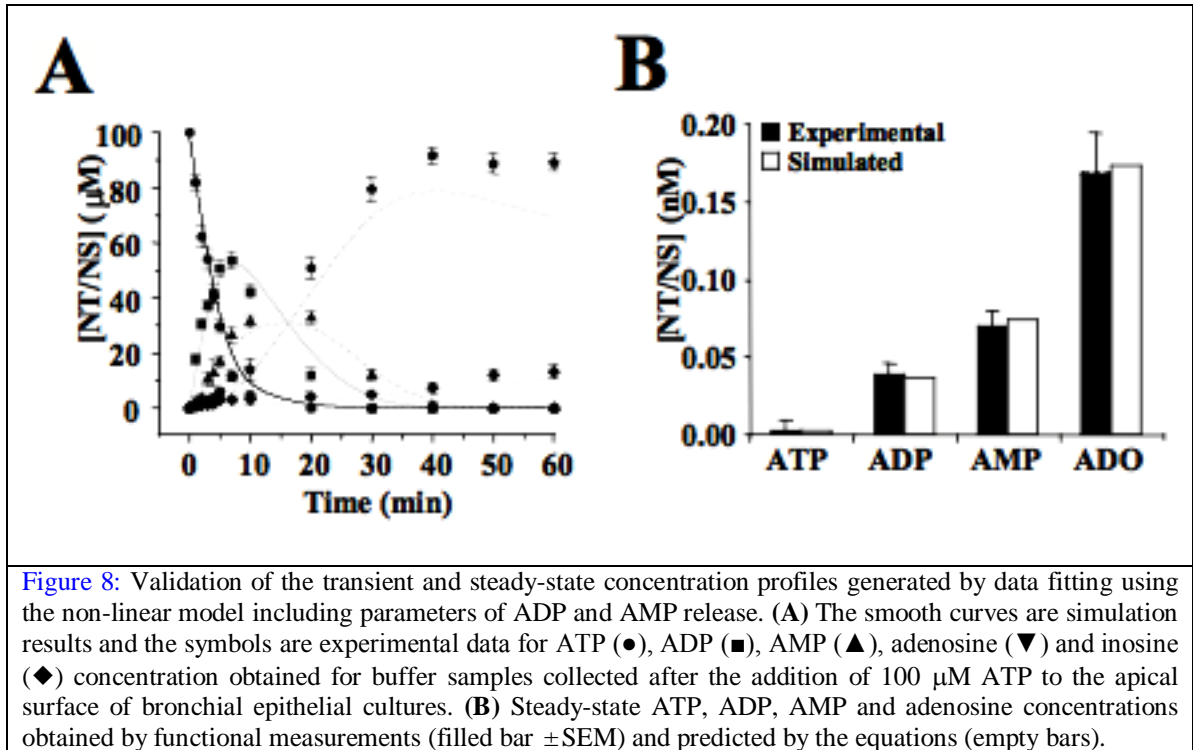


Figure 8: Validation of the transient and steady-state concentration profiles generated by data fitting using the non-linear model including parameters of ADP and AMP release. **(A)** The smooth curves are simulation results and the symbols are experimental data for ATP (●), ADP (■), AMP (▲), adenosine (▼) and inosine (◆) concentration obtained for buffer samples collected after the addition of 100 μM ATP to the apical surface of bronchial epithelial cultures. **(B)** Steady-state ATP, ADP, AMP and adenosine concentrations obtained by functional measurements (filled bar \pm SEM) and predicted by the equations (empty bars).

Sensitivity Analyses

The capacity of the computational model to reproduce the non-linear components of ASL nucleotide regulation was tested by sensitivity analysis of high-affinity Ecto-AK. Figure 9A shows that blocking Ecto-AK (vf11, kf11, kf12 vr12 and kr13; Table 1) accelerates the metabolism of ATP in the 0.1-1.0 μM range, as demonstrated by functional

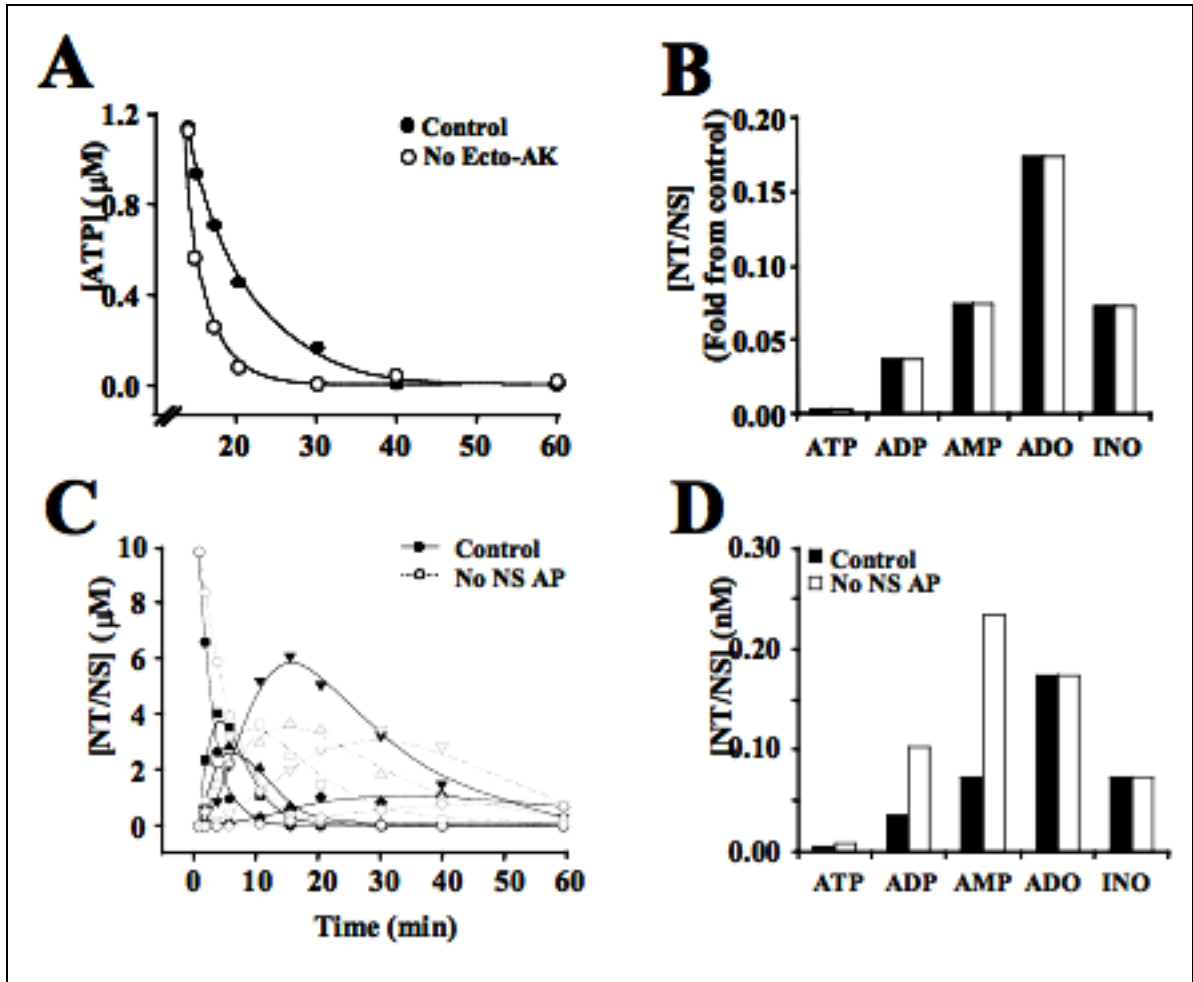


Figure 9: Sensitivity analysis of the non-linear model including ADP and AMP release for low-affinity NS AP and high-affinity E-NTPDase 1. (A, C) Time-dependent concentration profiles from 10 μM ATP before (solid line, filled symbols) and after (dashed line, open symbols) blocking Ecto-AK or NS AP parameters. The lines are simulations and the symbols experimental data obtained by monitoring the metabolism of 10 μM ATP on bronchial cultures in the absence/presence of inhibitors of Ecto AK (0.5 mM Ap_5A) or NS AP (10 mM levamisole) ($N = 3$; SEM omitted for clarity; ●○, ATP; ■□, ADP; ▲△, AMP; ▼▽, ADO; INO, ◇◆). The simulations also tested the impact of blocking (B) Ecto-AK or (D) NS AP inhibition on steady-state nucleotide concentrations, expressed as fold change after blockage.

assays conducted in the absence or presence of 0.5 mM Ap_5A [40]. Accordingly, Ecto-AK activity is not predicted to influence steady-state nucleotide concentrations (Figure 9B). These data suggest that the role of airway Ecto-AK would be to prolong P2 receptor-mediated responses within an optimum range of ATP concentrations [41].

Sensitivity analyses were also conducted to ascertain the contribution of NS AP to the regulation of ASL nucleotides. Although considered a low-affinity enzyme ($K_M > 300 \mu\text{M}$) when assayed at pH 9-10 [49,51], NS AP has been shown to exhibit both low ($K_M >$

400 μM) and high ($K_M \sim 12\text{-}20 \mu\text{M}$) affinities for adenine nucleotides at pH 7.5 in various tissues [52-54], including airway epithelia [26]. We previously determined that airway NS AP hydrolyzes AMP with K_M values of 36 μM and 717 μM [26]. Since the kinetic parameters of airway NS AP for ATP and ADP were unavailable, we performed these experiments on primary cultures of human bronchial epithelial cells, as we previously described [26]. Two sets of kinetic parameters were identified for ATP and ADP hydrolysis (Table 3), with K_M values in the ranges reported for total airway ectoATPase (k_1 and k_3) and ectoADPase (k_4 and k_5) activities (Table 1). The impact of blocking NS AP activity on ASL nucleotide regulation was simulated for a physiological ATP concentration (10 μM) [55-57] by reducing the fitted rate constants for ATP (v_1 , v_3) and ADP (v_4 , v_5) hydrolysis by the V_{MAX} values of NS AP (Table 3) and setting the parameters of NS AP for AMP hydrolysis (v_7 , v_8) [26] at zero. Figure 9C shows that blocking NS AP reduces the rate of ATP elimination, as well as ADP and AMP accumulation, by 2- and 3-fold. A stronger effect is predicted on adenosine production, depicted by a 4-fold decrease in accumulation rate and a 2-fold decrease in maximum concentration. These simulation data were closely reproduced by functional assays on bronchial epithelial cultures performed in the absence/presence of 10 mM levamisole [26] (Figure 9C). Furthermore, this sensitivity analysis predicts that NS AP influences steady-state ADP and AMP, but not ATP or adenosine (Figure 9D). Collectively, sensitivity analyses and functional assays suggest that NS AP contributes significantly to the regulation of transient and steady-state ASL nucleotide concentrations, with potential effects on the amplitude and duration of P1 (adenosine) receptor-mediated responses following mechanical stimulation.

The relative contribution of NS AP and ecto 5'-NT to the production of airway adenosine was investigated by sensitivity analyses comparing time-courses of adenosine

accumulation from 1-1000 μM ATP. The simulations were conducted before and after blocking the kinetic parameters of Ecto 5'-NT (v_6 , k_6 ; Table 1) or NS AP as above (Figure 9), and validated experimentally by paired functional assays on bronchial epithelial cultures before and after inhibiting Ecto 5'-NT (10 mM concanavalin A) [26,58] or NS AP (10 mM levamisole) [26,59]. The simulations closely reproduced the adenosine profiles obtained from bronchial cultures, as shown in Figure 10A-C for 0.1-10 μM ATP. These experiments also confirmed that both enzymes contribute significantly to the production of ASL adenosine from physiological ATP concentrations locally encountered after a mechanical stimulation [55-57]. Interestingly, the rate of adenosine accumulation from Ecto 5'-NT, but not from NS AP, decreased with increasing ATP concentration, resulting in a reversal of their relative contributions.

A mathematical model designed to describe the regulation of adenine nucleotides on endothelial cells provided evidence for a physiological role of feed forward inhibition by ATP on the regulation of vascular adenosine levels [60,61]. To test this possibility in the airways, the above time-courses of adenosine accumulation from ATP were repeated before and after blocking the feed forward inhibition constants (k_{i1} , k_{i2} ; Table 1). Based on the vascular model, the data were first analyzed in terms of initial delay to the accumulation of 0.3 μM adenosine, which approximates the EC_{50} of $\text{A}_{2\text{B}}$ receptors for CFTR activation on human bronchial epithelial cells [29,30]. Figure 10C shows that the lag phase to 0.3 μM adenosine was not affected by feed forward inhibition at physiological ATP concentrations ($\leq 10 \mu\text{M}$) [55-57]. Although not functionally relevant in the airways, the 5-fold reduction in lag phase predicted for Ecto 5'-NT with 1 mM ATP is in agreement with this enzyme's response on endothelial cells [60,61]. The simulations were also analyzed for the impact of feed forward inhibition on the conversion rate of AMP to adenosine. The model predicts that Ecto 5'-NT is significantly

inhibited by physiological ATP concentrations (1-10 μ M) [55-57], because blocking feed forward inhibition increased the rate of AMP hydrolysis by 3-fold (Figure 10E). This regulatory mechanism is expected to considerably affect the overall rate of adenosine production on airway epithelia after a mechanical stress, as shown by the significant effect on total ectoAMPase activities (Figure 10E). In contrast, NS AP activity was not affected by ATP concentrations. This sensitivity analysis demonstrates, for the first time, that the feed forward regulation of ASL adenosine is specific for Ecto 5'NT. On the other hand, the simulations showed that both enzymes regulate steady-state adenosine levels (Figure 10F), in agreement with their relative activities in the presence of 0.1 μ M ATP (Figure 10A). The lack of effect on the steady-state adenosine level suggests an efficient regulation by cell surface elimination. Altogether, these sensitivity analyses demonstrate that the proposed computerized model reproduces the linear and non-linear components of ASL nucleotide regulation, and provides novel information that will improve our understanding of nucleotide-mediated signaling in human airways.

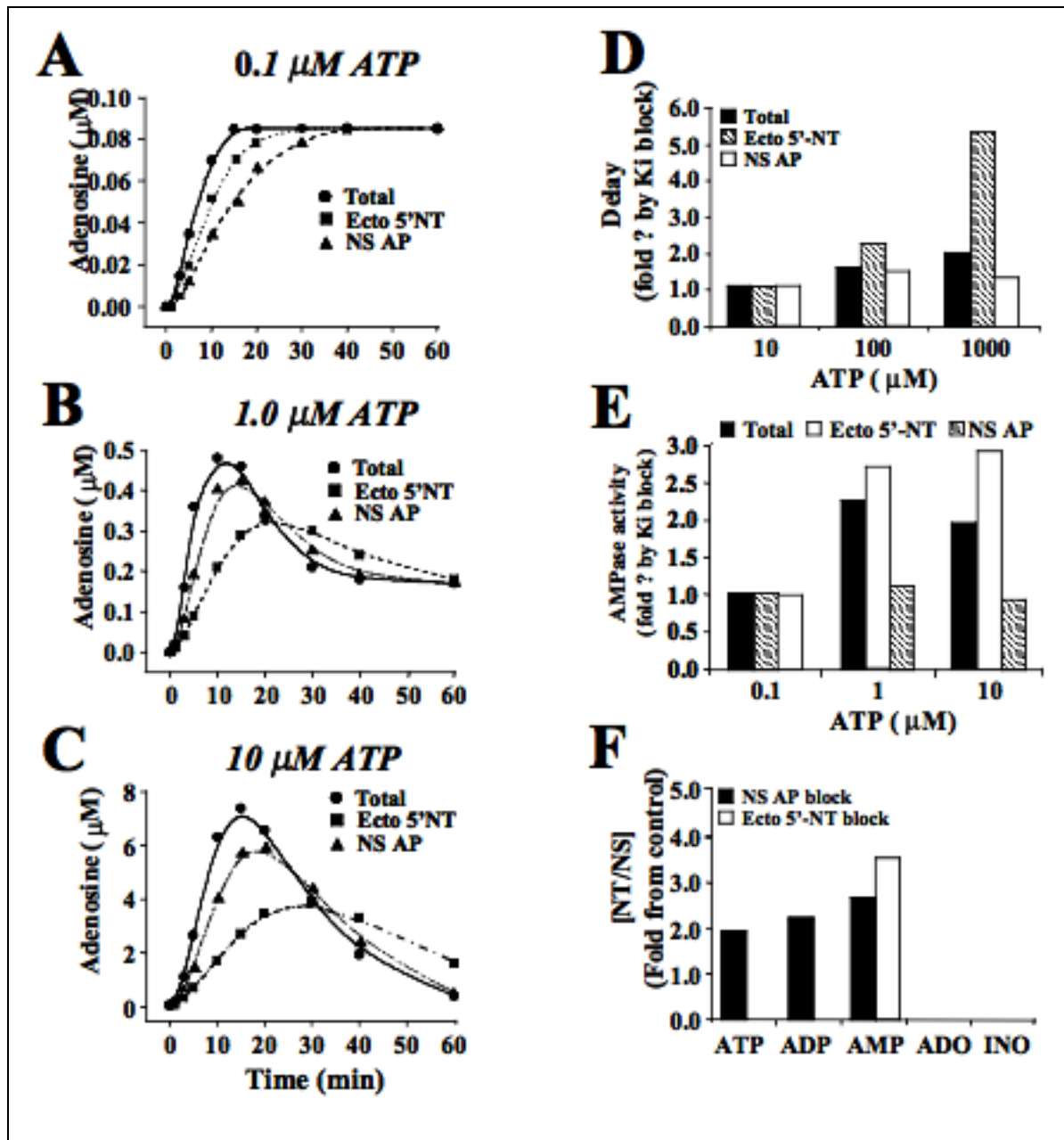


Figure 10: Relative contribution of Ecto 5'-NT and NS AP to airway adenosine regulation. (A-C) Simulated (lines) time-courses of adenosine accumulation from 0.1-10 μM ATP without/with isolating Ecto 5'-NT or NS AP activity by reciprocal blockage. The symbols are experimental data from HPLC analysis of ADO accumulation on bronchial epithelial cultures from 1 or 10 μM ATP with/without an inhibitor of Ecto5'-NT (10 mM concanavalin A) or NS AP (10 mM levamisole). The time-course simulations were analyzed for the impact of feed forward inhibition by ATP on (D) the delay to 0.3 μM adenosine and (E) the initial linear rate of ADO production from AMP. (F) Impact of blocking NS AP or Ecto 5'-NT activity on steady-state nucleotide levels (* N = 3-5; SEM < 10% of the mean, omitted for clarity).

2. 4 DISCUSSION

The importance of understanding the dynamic changes in nucleotide concentrations taking place on airway epithelia after a mechanical stimulation is highlighted by the pivotal role ascribed to purine signaling in the regulation of bacterial clearance [16,19]. The continuous (basal) release of ATP from airway epithelia into the ASL [20] constitutes a metabolic source of adenosine [26-28], maintaining baseline MCC through A_{2B} receptor-mediated ion/water efflux by CFTR and cilia beating activity [25,30]. Mechanical stress, such as physical interaction with a pathogen, recruits additional defense mechanisms through enhanced ATP release and P2 receptor-mediated ion/water efflux by the Ca²⁺-activated Cl⁻ channels, mucin secretion to confine the particle, and accelerated cilia beating activity to clear the infection [14]. The airways alertness is then rapidly restored by the conversion of ATP to adenosine. Purine signaling on airway epithelia, therefore, represents an exceptional example of the intricate relationships that evolved between nucleotide regulation and purinoceptor activation to protect the airways against the development of a chronic infection.

This study presents the first mathematical model of ASL nucleotide regulation on the apical surface of human airway epithelia. The equations incorporate the linear reactions mediating the sequential dephosphorylation of ATP to adenosine, the reversible Ecto-AK activity, the feed forward inhibition of adenosine production by ATP and ADP, adenosine conversion to inosine, ATP release and adenosine/inosine uptake. All kinetic parameters were extrapolated from functional experiments conducted on the apical surface of polarized primary cultures of human bronchial epithelial cells. The simulations closely reproduced the steady-state nucleotide concentrations and the transient concentration profile measured on cultured bronchial epithelial cells after the addition of 100 μ M ATP. However, regardless of the fitting strategy, a 15-fold difference remained

between the simulated and experimental rates of ATP release, suggesting that the model was missing a key component.

Recent efforts to elucidate the mechanisms of ATP release led to the proposition that adenine nucleotides other than ATP are also secreted from mammalian cells [47]. Mechanical stress has been shown to stimulate vesicular ATP release in a variety of mammalian cells, including endothelial and epithelial cells [17,46-48]. For instance, disruption of vesicle trafficking by brefeldin A inhibited basal and mechanically-stimulated ATP release from oocytes [62]. Secretory vesicles accumulate ATP and UDP-sugars at concentrations 50-fold higher than in the cytosol [47]. During maturation, they are converted to ADP and UDP, respectively, and eventually to AMP and UMP [47]. Vesicle fusion to the apical membrane is, therefore, expected to release not only ATP, but also ADP and AMP. Accordingly, modification of the model to include parameters of ADP and AMP release provided the best fit of experimental transient and steady-state concentrations profiles, and resolved the differences between predicted and estimated rates of ATP release.

The mathematical model reproduced an important property of ASL nucleotide regulation, which is the independence of steady-state nucleotide concentrations on dynamic changes in ASL volume. A volume doubling, which corresponds to the maximum response of the ASL to mechanical stress [23], disrupted the steady-state ATP concentration during < 3 min. Hence, the model simulation predicts that a single mechanical stimulation will sustain P2 receptor activation during < 3 minutes before purinergic signaling returns to baseline A_{2B} receptor-mediated MCC. Since ATP, but not adenosine, induces mucin release [63,64], this rapid “on-and-off” switch system may represent a protective mechanism against mucin overproduction and airway obstruction. In addition, as P2 receptor-mediated MCC constitutes an emergency response to airway

insults, the rapid cessation of each signal may represent an evolutionary means to optimize the airways alertness to subsequent invasions.

The complexity of the multi-enzyme system suggests that several ectonucleotidases compete for the same metabolic steps (NS AP: $\text{ATP} \rightarrow \text{ADP} \rightarrow \text{AMP}$; E-NTPDase1 or 3: $\text{ATP} \rightarrow \text{ADP} \rightarrow \text{AMP}$; E-NPPs; $\text{ATP} \rightarrow \text{AMP}$) [35]. This apparent redundancy may be resolved by sorting the ectonucleotidases in two kinetically-distinct groups regulating different nucleotide concentrations: high-affinity (E-NTPDase 1, E-NPPs, ecto-AK, NS AP) and low-affinity (AP, NTPDase 3, NS AP) [38,65]. Among them, the reversible transphosphorylating reaction of ecto-AK ($\text{ATP} + \text{AMP} \leftrightarrow 2\text{ADP}$) has been suggested to prolong the effective concentrations of the P2 receptor agonist, ATP, on the apical surface of human airway epithelia [40]. This proposition was confirmed in the present study by sensitivity analysis and functional assays against 10 μM ATP. The inhibition of Ecto-AK activity suppressed ATP elimination within 1.0-0.1 μM , which maximally activates P2Y₂ receptors on human airway epithelia [31]. Collectively, these findings demonstrate that the computerized model was able to capture the contribution of Ecto-AK to the biochemical network regulating ASL nucleotides.

Non-specific alkaline phosphatase represents a unique enzyme, exhibiting both low ($K_M > 400 \mu\text{M}$) and high ($K_M \sim 12\text{-}20 \mu\text{M}$) affinities for adenine nucleotides when assayed at physiological pH [26,52-54]. We previously showed that airway NS AP hydrolyzes AMP with K_M values of 717 μM and 36 μM [26]. In order to determine the role of NS AP in the regulation of ASL nucleotides, we determined the kinetic parameters of NS AP toward ATP and ADP on primary cultures of human bronchial epithelial cells. In agreement with the known characteristics of NS AP, two parameter sets were identified for each substrate, with low and high affinities, respectively. Based on this information, sensitivity analyses were conducted by blocking all kinetic parameters of NS AP for ATP,

ADP and AMP, and validated by functional assays conducted with the selective inhibitor, levamisole, on primary cultures of human bronchial epithelial cells. The corresponding simulation reproduced the impact of NS AP inhibition on the transient concentration profile generated by an ATP level ($10\ \mu\text{M}$) reached locally in response to mechanical stress [55-57]. The elimination of $10\ \mu\text{M}$ ATP was reduced by 20%, as previously demonstrated with a higher substrate concentration ($1\ \text{mM}$ ATP) [27]. Altogether, these data suggest that NS AP plays a minor role in the regulation of ASL ATP. On the other hand, the simulations and experimental data indicated that blocking NS AP causes larger perturbations on the transient adenosine profile, with a 4-fold decrease in the accumulation rate and a 2-fold decrease in maximum concentration. The lower impact on ATP than adenosine is consistent with the biochemical properties of purified NS AP, exhibiting relative maximal velocities in the following order: $\text{AMP} > \text{ADP} > \text{ATP}$ [49,66]. Altogether, these results suggest that NS AP regulates the amplitude and duration of P1 (adenosine) receptor-mediated responses following mechanical stimulation.

In the vascular system, the complex purinergic regulation of thrombus formation motivated the development of a mathematical model describing the regulation of nucleotide metabolism on endothelial cells [60,61]. The vessel walls are exposed millimolar ADP and ATP concentrations locally discharged by activated platelets. While ADP activates nearby platelets through P2Y_1 and P2Y_{12} receptors, ATP and adenosine suppress platelet activation through P2X_1 and A_{2A} receptors, respectively [67,68]. Platelet aggregation and thrombus formation are regulated by adenine nucleotide metabolism taking place on nearby endothelial cells by the coordinated activities of E-NTPDase 1 and Ecto 5'-NT [69]. Gordon et al. demonstrated that the dynamic changes in nucleotide concentrations taking place on endothelial surfaces exposed to $> 100\ \mu\text{M}$ nucleotides could only be simulated if the model included parameters of feed forward inhibition of

adenosine production by ADP [60]. In essence, extensive local nucleotide release, due to tissue damage and platelet degranulation, creates a time gap between ADP- and adenosine-mediated responses to allow sufficient time to consolidate the thrombus while minimizing spread beyond the site of damage. Biochemical assays conducted on purified enzyme preparations showed that Ecto 5'-NT is inhibited by ATP and ADP [70,71]. The regulation of adenosine on airway epithelial surfaces is further complicated by the presence of an additional ectonucleotidases supporting the cell surface conversion of AMP to adenosine: NS AP. We therefore tested whether feed forward inhibition plays a significant role in the regulation of adenosine by the complex biochemical network of airway epithelia. However, since most P2 receptor-mediated responses are initiated by ATP, rather than ADP [18], the present study focused on the ability of mechanically-induced ATP to regulate adenosine production.

The computational model and functional assays both demonstrated the existence of a significant negative relationship between ATP concentration and adenosine accumulation. The time lag required for the accumulation of 0.03 μM adenosine, which approximates the EC_{50} of $\text{A}_{2\text{B}}$ receptors for CFTR activation [29,30], was significantly increased by ATP concentrations $> 100 \mu\text{M}$. While these results are consistent with the vascular model [60,61], airway epithelial surfaces are not expected to encounter nucleotide concentrations above 10 μM under normal conditions [55-57]. Possibility remains that this regulatory mechanism may become relevant during massive ATP release, from extensive epithelial damage or bacterial killing, in chronic lung diseases such as emphysema.

Feed forward inhibition became physiologically relevant for ASL nucleotide regulation when analyzed in terms of the rate of adenosine accumulation. Model simulations and experimental data showed that 1-10 μM ATP significantly inhibits Ecto

5'-NT activity, as previously reported on airway epithelia [26]. In contrast, NS AP was unaffected by ATP concentration on human airway epithelia. The overall effect on ASL adenosine regulation was a reversal in the relative contribution of the two enzymes at ATP concentrations $\geq 1 \mu\text{M}$, as the concentration profile for adenosine accumulation became dictated primarily by NS AP. These results are in contradiction with the previously reported dominance of Ecto 5'-NT established on these epithelial surfaces for $100 \mu\text{M}$ AMP [26], which did not account for the feed forward inhibition by ATP. The present study illustrates the importance of investigating the physiological role of a single ectonucleotidase within an integrative setting including all factors regulating ASL nucleotides. This feed forward mechanism, in biochemical networks where NS AP is absent, may be important to prevent A_{2B} receptor desensitization [72]. On the other hand, chronic lung diseases, including cystic fibrosis, chronic pulmonary disease and primary ciliary dyskinesia, are characterized by enhanced NS AP activity and expression [27]. The lack of feed forward regulation of NS AP may contribute to the vulnerability of the airways to the development of chronically-elevated adenosine in pathological conditions associated with excessive ATP release, which is known to exacerbate inflammation and tissue damage [73].

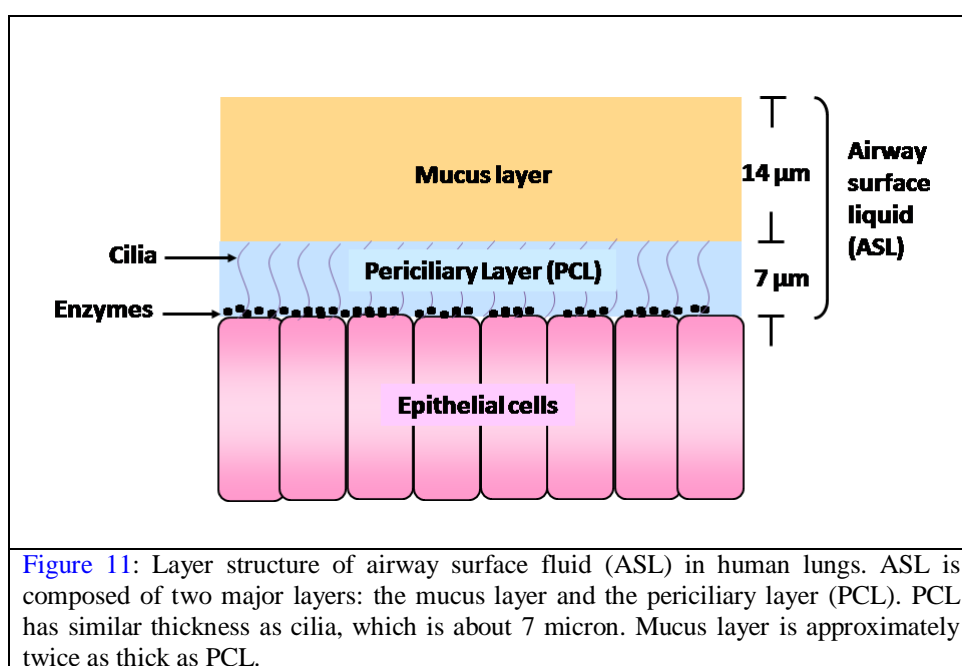
In conclusion, this study provides a robust mathematical model for the regulation of two powerful signaling molecules: ATP and adenosine. The model predicts that P2 and A_{2B} receptor-mediated epithelial responses will be sequentially activated by an insult, according to the relative concentrations of ATP and adenosine within the ASL layer. The present study also demonstrates that the physiological importance of a single ectonucleotidase may be tissue specific, depending on the biochemical network regulating extracellular nucleotides and on the local concentrations encountered under normal and pathological conditions. This demonstration constitutes a first step toward the

understanding of nucleotide-mediated MCC. In the near future, these equations will be refined to include parameters describing the regulation of P2 and P1 receptor activation, as well as the epithelial responses supporting bacterial clearance.

2. 5 FUTURE APPLICATION

Layered Structure of Airway Epithelium

Under *in vivo* condition, the airway epithelium in human lung is covered by two liquid layers: the periciliary layer (PCL) and the mucus layer (Figure 11). Among them, the periciliary layer (PCL) is the closest to the epithelial cell membrane. Nature designs the PCL in a way that it has approximately same height of cilia, a hair-like organelle that is rooted on epithelial membrane, so that cilia can conduct constant beating in the PCL. The force on the tip of cilia transports the mucus layer atop, along with the bacteria trapped in the mucus, in an upward motion and eventually out of our body through nose and throat. In physiology, the mucus layer and PCL, together, is called airway surface liquid, or ASL.



Epithelial cells are able to secrete enzymes to its membrane, which form a very thin layer within PCL (Figure 11). When ATP is released from epithelial cells, it diffuses through the enzyme layer first, where it interacts with enzymes and gets hydrolyzed. At the same time, some ATP molecules are able to escape and diffuse upward through the rest part of PCL and then to mucus layer. When the local concentration of ATP close to the epithelial cell membrane becomes less and less, ATP molecules beyond the enzyme layer will diffuse downward due to the concentration gradient (Figure 12).

Model Equations

As diffusion tends to drive ATP and its metabolites away from enzyme layer to prevent it from getting degraded, we are interested in how diffusion could possibly affect the metabolism of ATP and the metabolites. Therefore we built up a partial differential equation system that describes the motion of ATP in the ASL. Because only the total amount of enzymes has been measured, and we have no idea about the distribution of enzymes at epithelial cell membrane under *in vivo* conditions, we assume even distribution for enzymes in the spatial model. That means the diffusion happens only in the vertical direction, or the direction of ASL height. The thickness of different layers in this model is specified according to the *in vivo* measurements [86]. Due to the lack of information on thickness of enzyme layer, it is assumed to be 3 μm .

Eq. (2.24) describes the motion of the five species of nucleotides and nucleosides in the model. The variable \bar{C} is a vector, representing the concentrations of all the metabolites in the ASL. The activity of all the species in the enzyme layer $[0, L_E]$ is described by reaction-diffusion equation. Reaction diffusion systems are mathematical models that describe how the concentration of one or more substances changes under the

influence of two processes: chemical reactions in which the substances are converted into each other, and diffusion which causes the substances to spread out in space.

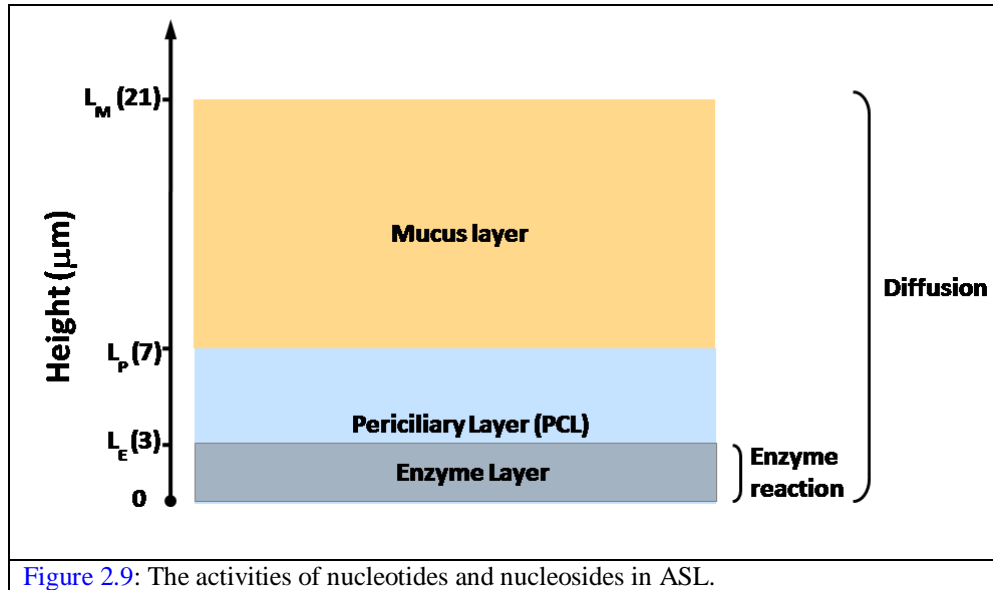


Figure 2.9: The activities of nucleotides and nucleosides in ASL.

Mathematically, reaction–diffusion systems take the form of semi-linear parabolic partial differential equations. In Eq. (2.24), $D_p \frac{\partial^2 \vec{C}}{\partial y^2}$ and $R(t, \vec{C})$ are related to diffusion along the ASL height and reaction in the enzyme layer, respectively. In the rest of the PCL and mucus layer, ATP and its metabolites follow Brownian diffusion. Therefore only the diffusion equation is used to describe their motion in these two regions. The property of PCL and mucus are quite different from each other. The former is has a texture that is similar to water (true?), while the mucus layer is more like gel. The value of D_p , the diffusion constant in the PCL, was chosen to be the same as the ATP diffusion rate in bulk water while its diffusion in mucus layer, D_M , was assumed to be 10 times slower. The difference between ATP, ADP, AMP, and nucleoside adenosine (ADO) is the numbers of phosphate and adenosine (ADO) and inosine (INO) only differ in an amino group. Therefore we assume they have the same diffusion coefficient. The model equations are:

$$\begin{cases} \frac{\partial \check{C}}{\partial t} = D_p \frac{\partial^2 \check{C}}{\partial y^2} + R(t, \check{C}) & y \in [0, L_E] \\ \frac{\partial \check{C}}{\partial t} = D_p \frac{\partial^2 \check{C}}{\partial y^2} & y \in [L_E, L_p] \\ \frac{\partial \check{C}}{\partial t} = D_M \frac{\partial^2 \check{C}}{\partial y^2} & y \in [L_p, L_M] \end{cases} \quad (2.24)$$

To solve the equations requires the specification of boundary conditions (Eq. (2.25)). The boundary conditions of the equation system are set up in such a way that there is constant exchange in epithelial cell membrane describing the release of nucleotides and uptake of adenosine (ADO) and inosine (INO). At the other end of boundary, i.e., the surface of ASL, zero flux is assumed. We also assume continuous flux between each two of the three layers. The initial condition is defined according to the situation we want to simulate.

$$\begin{cases} -D_p \frac{\partial \check{C}}{\partial t} \Big|_{y=0} = J \\ -D_M \frac{\partial \check{C}}{\partial t} \Big|_{y=L_M} = 0 \\ -D_p \frac{\partial \check{C}}{\partial t} \Big|_{y=L_E^-} = -D_p \frac{\partial \check{C}}{\partial t} \Big|_{y=L_E^+} \\ -D_p \frac{\partial \check{C}}{\partial t} \Big|_{y=L_p^-} = -D_M \frac{\partial \check{C}}{\partial t} \Big|_{y=L_p^+} \end{cases} \quad (2.25)$$

Numerical Methods

Operator-Splitting method is a common way to numerically solve reaction/convection diffusion equations, where reaction/convective and diffusive forces are accounted for in separate sub-steps. It is widely used in solving initial value problems for partial differential equations. That involves more than one operator on the right-hand side of the equation. We tried to use the Strang Operator Splitting Method, which is a second order numerical scheme (for details, see Appendix 1). Due to the discontinuity of

the reaction term along y axis, the noise around discontinuity gets larger with time and eventually grows unbounded. To minimize the noise, we have to start with a really small Δt or big Δx . Small time steps result in a fairly big matrix and time-consuming matrix operation. Big space steps lead to rough lattice and less information about the spatial distribution of nucleotide and nucleoside concentrations. However, the diffusion model doesn't favor a rough lattice. If we consider a 21 microns (μm) height for ASL and the enzyme layer is only a couple of microns, the size of grid can not exceed 1 micron. This results in slow computation. Meanwhile, the nonlinearity of the boundary condition for adenosine and inosine uptake makes the Strang Splitting Method less applicable to our problem.

The deficiency of Splitting Method led us to try other numerical methods for solving reaction-diffusion equations. We switched to a Finite Element Method, which is a method for solving the equations by approximating continuous quantities, such as the flux, at discrete points, regularly spaced on a grid or mesh. Because finite element methods can be adapted to problems of great complexity and unusual geometry, they are an extremely powerful tool in the solution of important problems in heat transfer, fluid mechanics, and mechanical systems. We use a modeling package called COMSOL Multiphysics (formerly FEMLAB) to solve the reaction-diffusion equation system. COMSOL Multiphysics is a software for solving different types of PDE's with finite element method in conjunction with adaptive meshing and error control as well as with a variety of numerical solvers, which allows us to use really fine grid in the enzyme layer and rougher grid in other regions.

Justification of Model Simplification for the *in vitro* Experiments

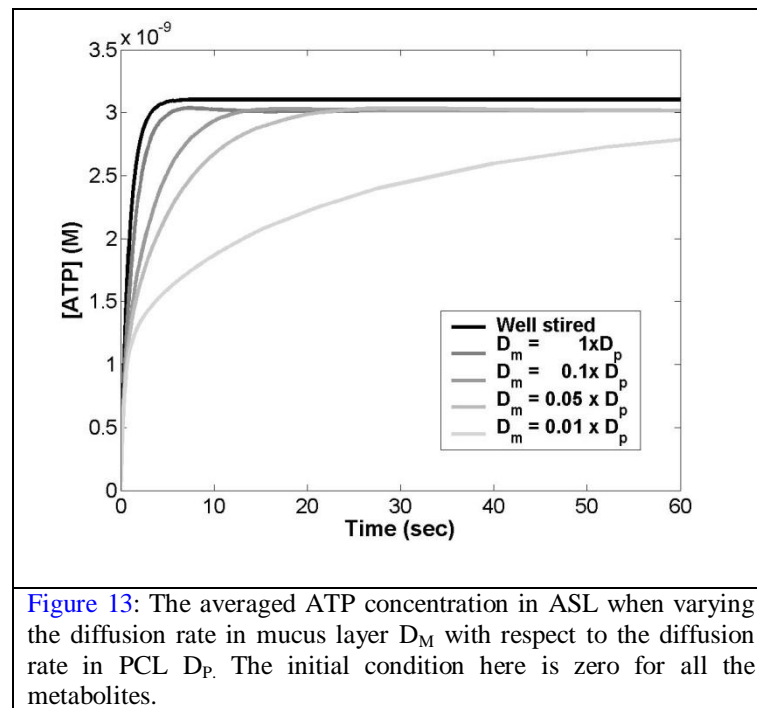
The *in vivo* studies showed that most of enzymes that catalyze nucleotide metabolism were localized at the surface of epithelial cells in a layer about two microns high. Considering the height of airway surface liquid (7-21 microns 86), which is about 10 to 20 times higher, it is reasonable to expect the existence of vertical gradients in [NT/NS]. As the diffusion constant of the molecules also determines if a spatial model is needed, we estimated the time required for an ATP molecule to diffuse across the ASL. Table 3 shows various diffusion coefficients for a ATP molecule in different media. As can be seen from Table 3, ATP diffuses in endothelium-fluid interface from pig aortic endothelial cells at a slightly slower rate than it does in bulk water. For a medium with higher viscosity similar to the cytoplasm, the speed is reduced by half. This means the speed for a single ATP molecule to diffuse in the PCL is on the order of $10^{-6} \text{ cm}^2 \cdot \text{sec}^{-1}$. Because no one has ever measured ATP diffusion in the mucus layer, we first consider the case in which ATP diffuses equally fast in mucus as in PCL. By the relation $T \sim O(L^2/D)$, the time it takes to diffuse from the cell membrane to the surface of ASL could be estimated to be a couple of seconds. Compared to the time for a pharmacological dose of ATP (100 μm) to hydrolyze in ASL, which is about 10 seconds, the ASL can be considered a well-mixed solution and diffusion in this case is neglectible.

Media in which ATP diffuses	Diffusion Coefficients (cm^2/sec)	References
Cytoplasm	1.5×10^{-6}	[74]
Bulk water	3×10^{-6}	[75]
Endothelium-fluid interface from pig aortic endothelial cells	2.36×10^{-6}	[76]

Table 3: Diffusion constants of ATP in different media

We then considered the situation in which ATP diffuses at a different rate than it does in the PCL. Considering the mucus layer is similar to gel, it is very likely the ATP diffuses slower in this layer. We varied the diffusion rate D_M compared to D_P , the

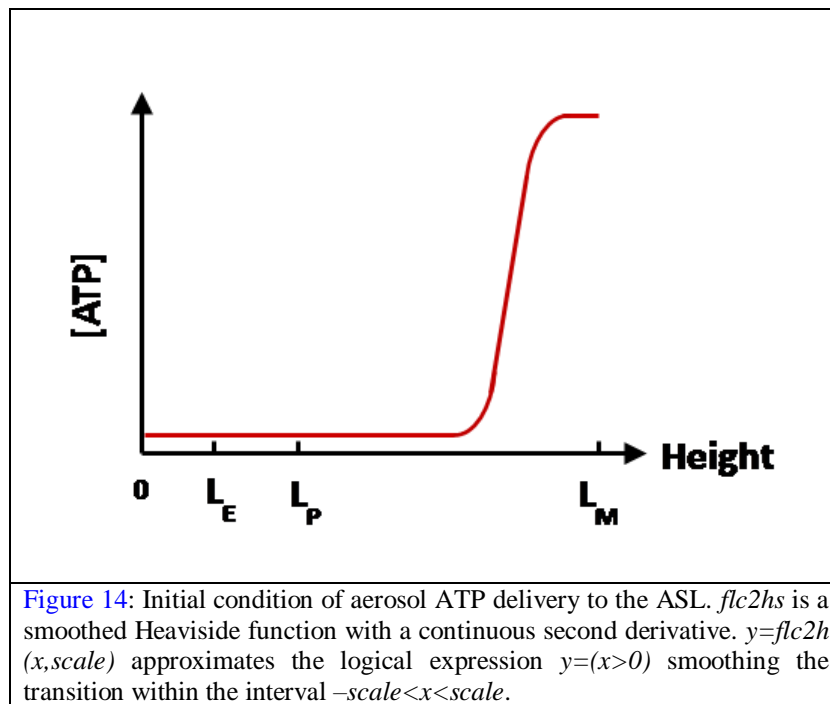
diffusion in PCL and observed the behavior of the averaged ATP concentration in ASL shown in Figure 13. As we slow down the diffusion of ATP in mucus layer, the time for ATP to reach the steady state becomes longer. However, not until the diffusion in mucus layer is 100 times slower than that of PCL, does the average ATP level in ASL show much of a difference. This simulation, along with the calculation earlier, provides strong justification for neglecting diffusion in the in vitro experiments we are about to model. In those experiments, the mucus layer was removed for the convenience of measuring the ATP level. With the presence of only the PCL, the media can be considered as well stirred solution and only enzyme reactions are necessary to describe the dynamics of ATP and its metabolites.



Simulation for Aerosol Delivery

One of the future applications for the ATP regulation model is to study the aerosol drug delivery to the airway of CF lungs. However, one symptom of CF is the

accumulation of mucus layer due to the infection and inflammation. In this case, the mucus layer is so thick that diffusion will affect the ATP delivery to the airway surface and eventually to the interaction with membrane receptors. The validation of ATP regulation model without spatial consideration enables us to use it as the reaction term in the spatial model we derived earlier. The initial condition here is assumed to be a step function representing a layer of ATP at the ASL surface and steady state elsewhere. To minimize the numerical error introduced by the discontinuity in the initial condition, we use the function *flc2hs* in COMSOL Multiphysics to smooth out the jump (Figure 14).



We numerically solve the equations and calculated the local [ATP] at the epithelial membrane where receptors locate. Figure 15 shows that with high mucus height, ATP is diluted in the larger volume so the [ATP] at cell surface is too low to activate the receptor (The effective range of activation is 1uM to 100nM). This simulation will be very helpful for studying the effective dose of ATP when designing the inhaling drugs for CF.

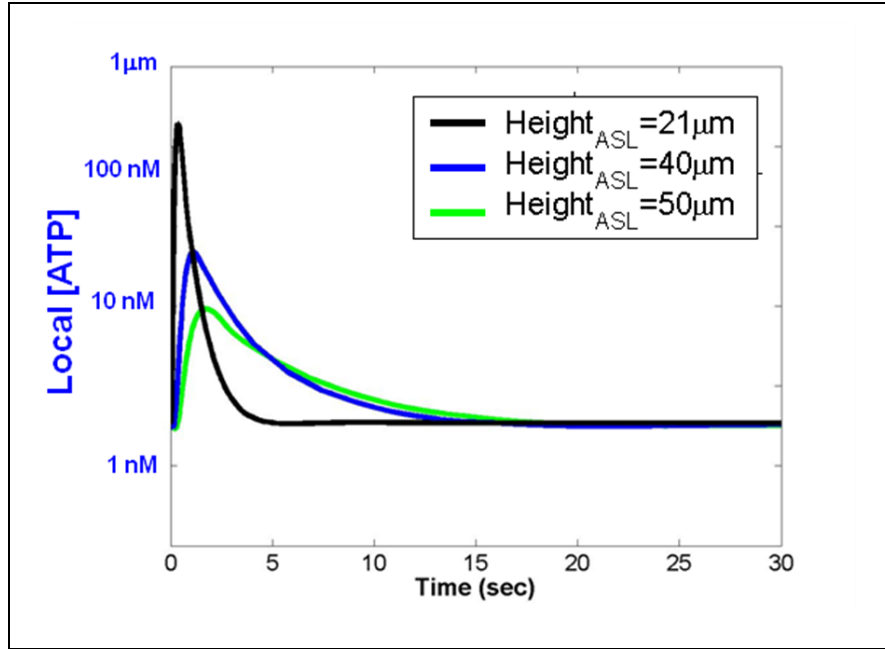


Figure 15: The local ATP concentration at epithelial cell membrane numerically solved from the partial differential equation system. The three curves represent the numerical solution when we vary the ASL thickness while keeping the PCL height fixed.

CHAPTER 3

ION/WATER TRANSPORT MODEL

3.1 INTRODUCTION

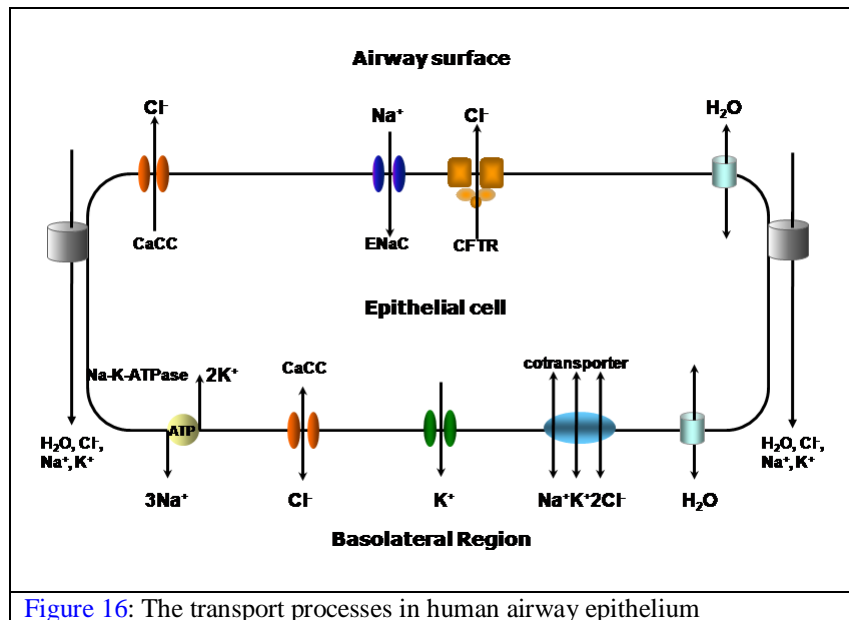
Epithelial cells make up the lining of the lungs, pancreas, liver, digestive tract and reproductive system, and are also found in the sweat glands and sinuses. As mentioned earlier, one of the symptoms of CF is to have salty sweat due to the impaired salt absorption in the sweat duct, caused by the absence or malfunction of CFTR Cl^- channel in the apical membrane of duct cells [77]. One of many treatments for CF is saline inhalation. Two studies published by Donaldson and Boucher *et al.* [78] reported that CF patients who inhaled hypertonic saline solution at least twice a day were hospitalized half as often for lung problems and showed significantly improved mucus clearance. Hypertonic saline increases the ion gradient in the ASL and therefore leads to re-hydration of the airway surface. The potential therapeutic drug we are interested in, ATP, restores the ASL through a different mechanism but with same result. ATP binds to membrane-bound receptors and activates a second chloride secretion pathway by opening Calcium-activated Chloride Channel (CaCC). This mechanism also results in an enhanced ion gradient in the airway surface and contributes to the re-hydration of the ASL.

The balance of airway surface liquid across the epithelial cell membrane involves the complicated interactions of various transport processes. The three major types of transport processes in this system are passive diffusion down electrochemical gradients, cotransport, and active transport, which consumes energy. These transport processes are

inter-related through direct or indirect ways. They act in concert to produce a strongly coupled and highly nonlinear system. Therefore, to understand this system requires mathematical modeling.

We built a computational model based on a model for the epithelium of dog trachea proposed by Novotny and Jakobsson [79,80]. We have converted the original ion and water transport model of Novotny *et al.* into MatLab and re-set the input parameters to match the data from human bronchial epithelial cells reported by Willumsen *et al.* [81-85]. To humanize the system, basolateral membrane chloride channels were included in the model.

3.2 MATHEMATICAL EQUATIONS



The model of human airway epithelium is composed of three compartments: the airway surface, intracellular region and basolateral region (Figure 16). Transport processes across the apical membrane are characterized by passive sodium and chloride movement. The basolateral membrane contains passive potassium and chloride transport,

along with active sodium-potassium transport and sodium-potassium-chloride cotransport. Both membranes are permeable to water except the paracellular pathway, which only transports salt.

Passive ion transport not only depends on concentration gradients, but also the membrane potential difference and therefore is considered eletrodiffusion. To model this effect, we used the Goldman-Hodgkin-Katz equation (Eq (3.1)), which describes the current produced by an ion species moving from compartment x to y. The current depends on the transmembrane potential V_m , the concentrations in each compartment ($C_{i,x}$ and $C_{i,y}$), the permeability of the membrane to this ion (P_i), and the absolute temperature. This formula also has several constants such as the valence of ion z_i , the Faraday constant F and the ideal gas constant R . The ion flux is:

$$J_{Pass,i,x \rightarrow y} = \frac{-P_i Z_i F V}{RT} \left(\frac{C_{i,x} - C_{i,y} \exp\left(\frac{Z_i F V_m}{RT}\right)}{1 - \exp\left(\frac{Z_i F V_m}{RT}\right)} \right) \quad (3.1)$$

The flow of water only depends on the ion gradients and transmembrane permeability to water molecules. Therefore the mathematical representation of water flux takes a simple form as in Eq. (3.2).

$$J_{H_2O,x \rightarrow y} = P_{H_2O} \left(\sum_i C_{i,x} - \sum_i C_{i,y} \right) \quad (3.2)$$

where the $\sum_i C_{i,x}$ and $\sum_i C_{i,y}$, are total ion concentrations including the impermeant anions in the two compartments. The active transport of sodium and potassium through energy-dependent pumps is modeled according to Michaelis-Menten kinetics with a pump ratio of three sodium ions per two potassium ions. A term was included to represent the

dependence of the pump on membrane potential ($5 \times 10^{-3} V_{m,B} + 1.25$). This term was derived from the pump reversal potential. This leads to the following expressions for active ion fluxes:

$$J_{pump,baso \rightarrow cell} = J_{pump,max} \left(\frac{[Na^+]_{cell}}{[Na^+]_{cell} + K_{pump,Na}} \right)^3 \left(\frac{[K^+]_{baso}}{[K^+]_{baso} + K_{pump,K}} \right)^2 \left(5 \times 10^{-3} V_{m,B} + 1.25 \right) \quad (3.3)$$

$$J_{pump,Na,baso \rightarrow cell} = -3J_{pump,baso \rightarrow cell} \quad (3.4)$$

$$J_{pump,K,cell \rightarrow baso} = 2J_{pump,baso \rightarrow cell} \quad (3.5)$$

The flux through cotransporter was modeled according to Michaelis Menten theory (Eq. (3.6)) as well. $J_{cot,max}$ is the maximum ionic flux through the cotransporter (in $\text{mol.m}^{-2}.\text{s}^{-1}$). The cotransporter ratio is one sodium ion to one potassium ion to two chloride ions. Therefore the ion flux through this pathway remains electro-neutral at all times. The flux through the cotransporter is:

$$J_{cot,x \rightarrow y} = J_{cot,max} \left(\frac{[Na^+]_x}{[Na^+]_x + K_{cot,Na}} \cdot \frac{[K^+]_x}{[K^+]_x + K_{cot,K}} \cdot \frac{[Cl^-]_x}{[Cl^-]_x + K_{cot,Cl,1}} \cdot \frac{[Cl^-]_x}{[Cl^-]_x + K_{cot,Cl,2}} - \frac{[Na^+]_y}{[Na^+]_y + K_{cot,Na}} \cdot \frac{[K^+]_y}{[K^+]_y + K_{cot,K}} \cdot \frac{[Cl^-]_y}{[Cl^-]_y + K_{cot,Cl,1}} \cdot \frac{[Cl^-]_y}{[Cl^-]_y + K_{cot,Cl,2}} \right) \quad (3.6)$$

The rate of change of the ion concentrations in each compartment is given by the sum of the fluxes into that compartment. For example, the rate equation for sodium concentration in cytoplasm is described by Eq (3.7). where $J_{pass,Na,a \rightarrow c}$ and $J_{pass,Na,b \rightarrow c}$ are passive sodium flux from apical and basolateral regions, while $3J_{pump,Na,b \rightarrow c}$ and $J_{cot,b \rightarrow c}$ are active transport and cotransport sodium fluxes, respectively. The intracellular cell volume is included in the equation to account for dilution effects caused by the water flux.

$$\frac{d[Na^+]_c}{dt} = \frac{1}{Vol_c} \left(J_{pass,Na,a \rightarrow c} + J_{pass,Na,b \rightarrow c} + 3J_{pump,Na,b \rightarrow c} + J_{cot,b \rightarrow c} - \frac{dVol_c}{dt} [Na^+]_c \right) \quad (3.7)$$

Following the same consideration, we build up a system of equations, which describes the ion concentrations and volume in each compartment. A complete list of equations in the model is shown in Appendix II.

The relaxation times for different process in this model are quite different from each other. The fastest time scale in the system is that for the membrane potential to respond to changes in ion concentration. The membrane potential responds with a characteristic time on the order of milliseconds determined by the resistance-capacitance time constant of the membrane. The time scale for water movement is slightly faster than 1 second and that for changes in ion concentrations is on the order of tens of seconds. Therefore the system is stiff. We used ode15s, the stiff ODE solver in MATLAB to numerically solve the system.

At equilibrium, the transmembrane currents satisfy Kirchhoffs loop and node laws, such that if the cell were represented by the electrical circuit in [Figure 17](#), then at any junction of the circuit the algebraic sum of the currents must be zero (Eq. (3.8)). In this figure, I_A , I_B and I_P are the currents across the apical membrane (positive into the cell), the basolateral membrane (positive into the cell), and the paracellular pathway (positive toward basolateral surface), respectively. $V_{m,A}$, and $V_{m,P}$ are the apical and transepithelial membrane potentials referenced to the mucosal surface. $V_{m,B}$ is the basolateral membrane potential referenced to the submucosal mucosal surface.

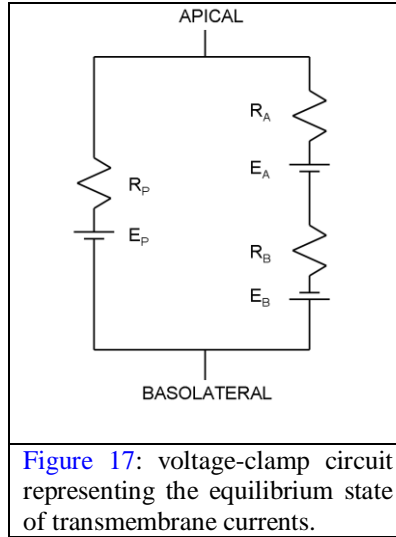


Figure 17: voltage-clamp circuit representing the equilibrium state of transmembrane currents.

$$\begin{cases} I_a(V_{m,A}) + I_p(V_{m,P}) = 0 \\ I_b(V_{m,B}) - I_p(V_{m,P}) = 0 \\ V_{m,P} = V_{m,A} - V_{m,B} \end{cases} \quad (3.8)$$

At each time step t , we first solve the nonlinear equation system (Eq (3.8)) for the equilibrium state of membrane voltages based on the ion gradients and membrane potentials from previous time step. These new values are then used as constants in the equations describing the rate of change in ion concentrations and volumes. We make sure the units of the fluxes in the equations are consistent. All fluxes, amounts, and volumes were normalized to the epithelial surface area. Fluxes were in units of moles per second per square meter, amounts in each compartment in moles per square meter, and volumes of each compartment in cubic meters per square meter. The equilibrium value for apical volume per surface area was chosen to be $7 \mu\text{m}$, so that the apical fluid has a height equal to the length of the cilia [86,87]. For cell, the equilibrium cell volume per surface area was chosen to be $20 \mu\text{m}$, the volume of the cell if it were cylindrical with dimensions shown in electron micrographs [86,87] .

Our strategy is to benchmark the modified Novotny model of ion and water fluxes without including nucleotide regulation. In the absence of such regulation, the Novotny

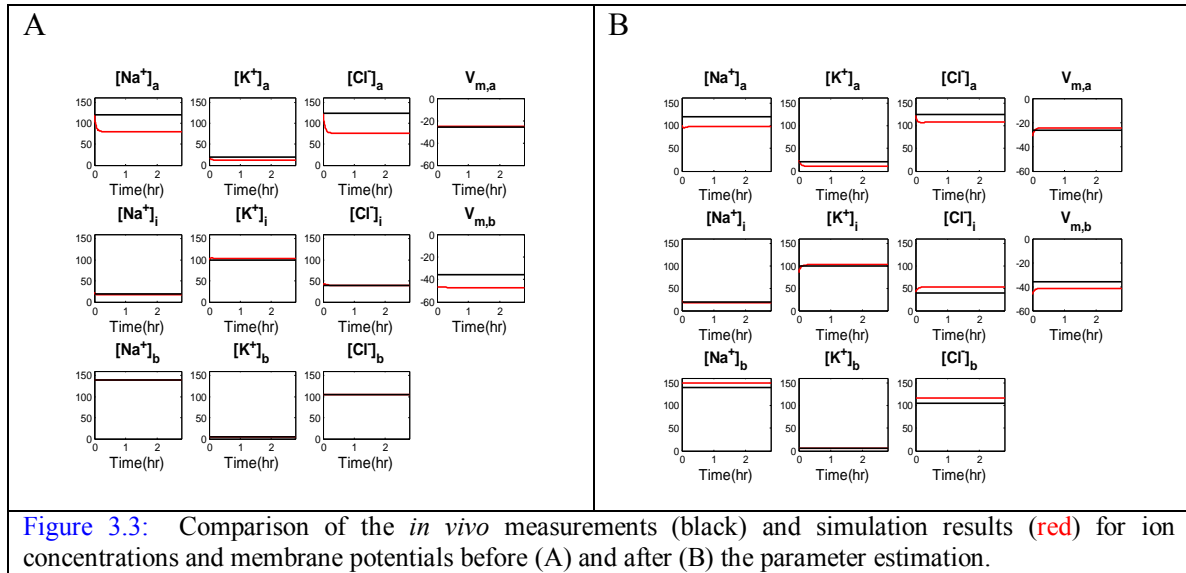
model leads to a state of either complete absorption or unbounded increase in the ASL. Although the former has been observed from experiment, the unbounded ASL volume is an unphysiological feature. To overcome this effect, Novotny added volume regulation to the permeability of the apical membrane Cl^- channel and to the maximum flux of the basolateral membrane cotransporter. Unfortunately, they did not specify a mechanism for how the channels and transporters could detect apical and cell volumes and assumed a linear coupling to the volume with prescribed upper and lower bounds on the permeability and maximum flux. In Chapter 4, we are going to address this problem and assume a more realistic nonlinear coupling that does not require specifying artificial upper and lower bounds. The ultimate goal is to develop a model that is capable of homeostatic regulation by coupling the ion and water flux model to the nucleotide regulation model.

3.3 PARAMETER ESTIMATION

The model described above is initial-condition-dependent, meaning that varying the initial ion concentrations in each compartment will produce different steady state concentrations, volumes and membrane potential. Mathematical analyses revealed that this feature is a consequence of the quasi-steady state approximation used for the membrane potential. Therefore, we searched for parameter sets that are biologically meaningful and produce steady state that is consistent with the experimental observations.

We fixed the apical and intracellular volumes and ran the simulation to steady state. If the steady state is close to the experimental observations, we then let the volume change as a result of concentration gradients. The ion channel permeabilities ([Table 4](#)) were collected from literature [81-85] on human epithelium. When these values were used in the simulations, the model produced discrepancies in the steady state of ions and

membrane potentials (Figure 18A). Therefore, we optimized the permeabilities such that the model produced steady state that matches the experimental observations (Figure 18B, Table 5).



As shown in Table 5, the parameter estimation produces a set of ion concentrations and membrane potentials that has smaller difference from the *in vivo* measurements. There is significant decrease in the discrepancies in the apical chloride concentration and basolateral membrane potential. However, the apical sodium concentration remains 16% lower than the *in vivo* condition, despite a small improvement after the estimation. On the other hand, the differences of the estimated permeabilities (Table 4) and *in vivo* measurement are all less than 2 folds, suggesting the model equations do not have major defects. It is well known that the movement of chloride across the apical membrane involves the CFTR Cl^- channel; however, conductive pathways for Cl^- movement across the basolateral membrane have been little studied. Willumsen *et al.* [84] had found out that Cl^- transport across the basolateral membrane in the CF epithelium occurs mainly

through the bumetanide⁴-sensitive cotransport system but also through a Cl⁻ conductance, which suggested that a chloride channel is available to the CF airways. We took this into consideration and estimated this permeability along with other parameters. The estimated basolateral chloride permeability is 3.5×10^{-8} m/s, which is slightly smaller than the apical permeability to Cl⁻. We will compare this estimation with experimental measurements when it is available.

Apical Membrane ($\times 10^{-8}$ m/s)			Basolateral Membrane ($\times 10^{-8}$ m/s)			Paracellular Membrane ($\times 10^{-8}$ m/s)		
	Exp.	Opt.		Exp.	Opt.		Exp.	Opt.
$P_{Na,a}$	1.60	1.30	$P_{Na,b}$	0	0	$P_{Na,p}$	1.20	1.41
$P_{K,a}$	0	0	$P_{K,b}$	10.5	9.98	$P_{K,p}$	3.14	3.08
$P_{Cl,a}$	2.60	4.19	$P_{Cl,b}$	0	3.50	$P_{Cl,p}$	1.20	1.00
$P_{H_2O,a}$	8650	10200	$P_{H_2O,b}$	8650	7940	$P_{H_2O,p}$	0	0

Table 4: Comparison of *in vivo* measurements of membrane permeabilities to ions and water with estimated values.

	Airway Surface		Cytoplasm		Basolateral Region	
	Exp.	Opt.	Exp.	Opt.	Exp.	Opt.
[Na ⁺]	120 mM	101 mM	20 mM	23 mM	140 mM	149 mM
[K ⁺]	20 mM	24 mM	100 mM	84 mM	5 mM	5.4 mM
[Cl ⁻]	125 mM	123 mM	40 mM	41 mM	105 mM	116 mM
V _m	-26 mV	-24 mV			-36 mV	-41 mV

Table 5: Comparison of variables at steady state before and after parameter estimation.

3.4 MODEL VALIDATION

We then validated the model by testing it against the *in vitro* experiments [81-85], in which the salt concentrations in bilateral compartments were perturbed. Data from human

⁴ Bumetanide is a potent diuretic that used to inhibit the Na⁺-K⁺-2Cl⁻ cotransporter.

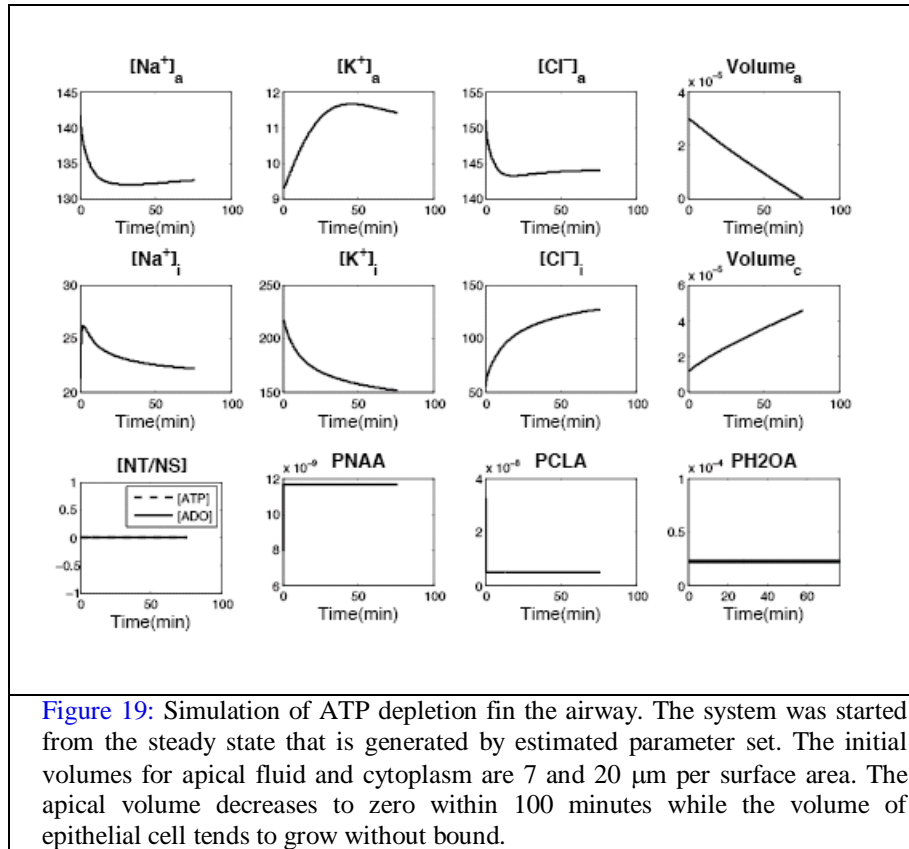
nasal epithelial cells were chosen because there are little experimental measurements from human bronchial cell available. The nasal membrane permeabilities to ions are also very similar to bronchial cells. All of these the experiment was conducted using an Ussing chamber setup so that both the apical and basolateral volumes are fixed. So when modeling the experiments, we set these two parameters constants and only change the initial condition of the ions in different compartments. Shown in Table 6 is the comparison of the measurements from one experiment [82] and the simulation results from the model. In this experiment [82], apical addition of amiloride (10^{-4}M) hyperpolarized the apical membrane potentials and decreased transepithelial current. The dose used for amiloride (10^{-4}M) has been tested to able to block nearly 100% of the sodium flux across the apical membrane on the area of the cell culture. To simulate this condition, we set the apical sodium permeability to zero and ran the model to steady state. Our model successfully predicted the trend of change in membrane potentials ($V_{m,A}$, $V_{m,B}$) and transmembrane short current (I_{eq}) after the blocking of apical sodium channel.

		$V_{m,A}$ (mV)	$V_{m,B}$ (mV)	I_{eq} ($\mu\text{A}/\text{cm}^2$)
Exp.	Control	-25.9	-37.7	-38.7
	Amiloride	-36.6	-41.8	-14.8
Sim.	Control	-31.6	-50.0	-28.9
	Amiloride	-60.0	-66.2	-14.6

Table 6: Experimental observations and numerical simulation using the ion water transport model in the experiment where apical sodium is blocked by amiloride.

We then started from the model from steady state and allowed the volumes in apical and cytoplasm region vary. Without any regulation mechanisms in the model, the simulation results shows a decreasing apical volume (Figure 19), which agrees with the *in vivo* observation of un-regulated human airway [88]. Due to the increased ion concentration inside the cell, its volume in the increases without bound in the simulation.

In reality, the cell couldn't grow forever. At a certain volume, the surface tension on the cell membrane fails to hold the cytoplasmic solution and the cell lyses. However, it is very likely that the cell volume can be regulated and kept under control when the airway surface liquid is subject to the ATP regulation.



3.5 CONCLUSION

The ion/water transport model was based on the physiological theory of ion/water transport. The procedure used to perform parameter estimation is very similar to that of ATP regulation model. We used the measure parameter values as initial guesses and searched for a set of parameters that could produce the best fit for the model compared to the resting level of ion concentrations and membrane potentials in the different compartments of airway epithelium. The positive prediction of the model, i.e., the blocking of apical sodium channel and test of default state without any regulation both

suggest that the ion/water model accurately captures key features of ion and water movement in the airway epithelium and therefore serves as a good model for integration with the ATP regulation model.

CHAPTER 4

AIRWAY SURFACE LIQUID REGULATION

In this chapter, we focus on studying the signaling pathways initiated by ATP and UTP in epithelial cytoplasm. A series of experiments designed to investigate different pathways are performed to show how triphosphate nucleotides (ATP and UTP) and their metabolite might, by up-regulating chloride secretion to the airway surface and inhibiting absorption of sodium ions back to cytoplasm, be potential therapeutic targets.

4.1 INTRODUCTION

The pathogenesis of cystic fibrosis is very complicated. As described in earlier chapters, it is characterized by abnormal regulation of the airway surface liquid (ASL). The results are achieved by the dual effects of down-regulation of chloride secretion due to the mutations in cystic fibrosis transmembrane conductance regulator (CFTR) as a chloride channel and hyper-absorption of epithelial sodium ions. Further experimental evidence showed that there is a second chloride channel in the apical membrane of airway epithelia, which is regulated by increases in intracellular free calcium (Ca^{2+}_i) [11-13]. There is experimental evidence showing the release of triphosphate nucleotides to the airway under normal condition. Along with their metabolites, they are able to initiate the autocrine and paracrine regulation on ion transport [90-92].

There are two major signaling pathways induced by ATP in normal epithelium (Figure 20). Intracellular ATP are secreted in response to diverse stimuli (local stress,

addendum) and are hydrolyzed by ecto-nucleotidases and other enzymes on airway epithelium to adenosine (ADO) and inosine (INO), which are taken back into the cytoplasm by transporter proteins (see

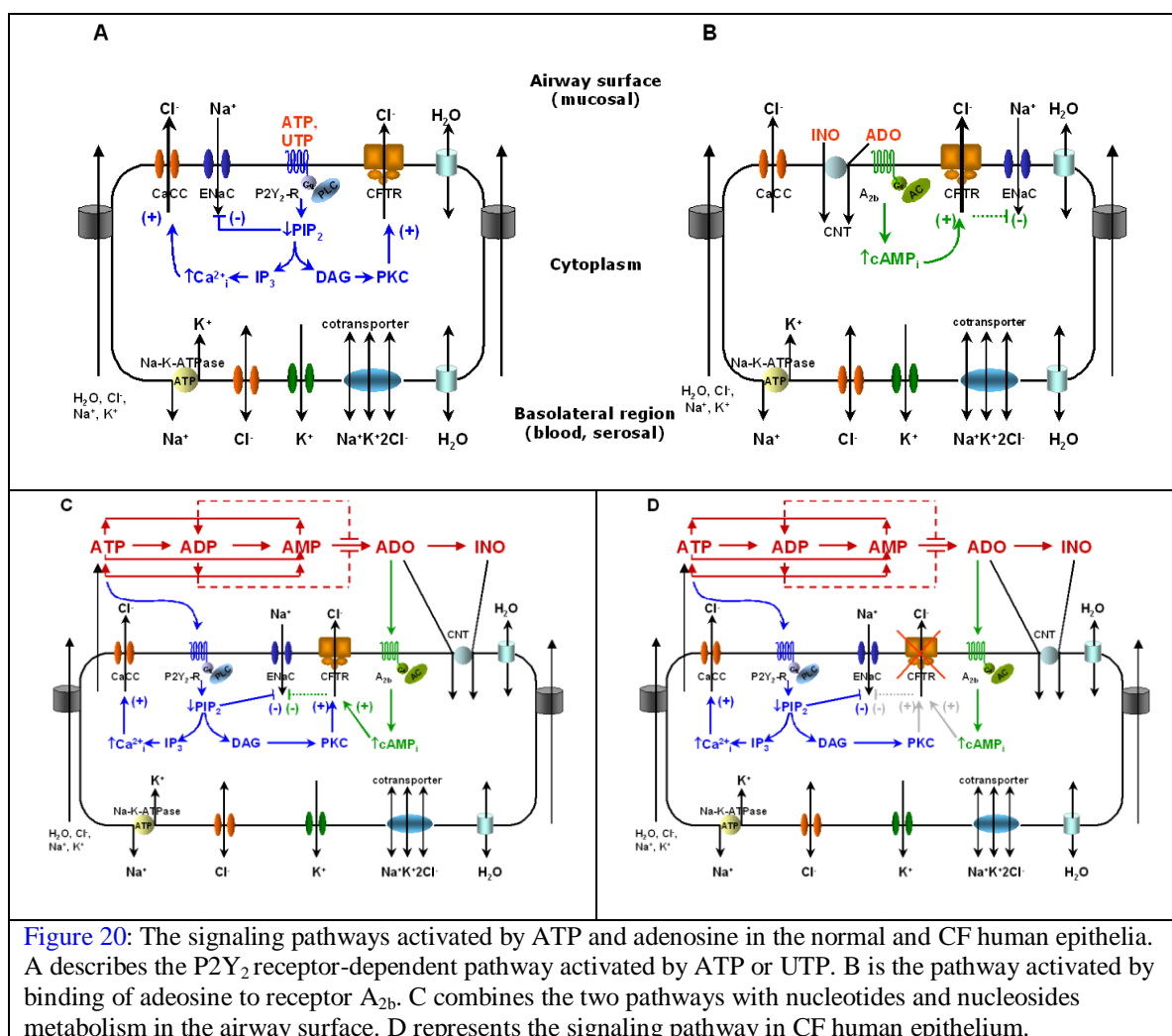


Figure 20: The signaling pathways activated by ATP and adenosine in the normal and CF human epithelia. A describes the P2Y₂ receptor-dependent pathway activated by ATP or UTP. B is the pathway activated by binding of adenosine to receptor A_{2b}. C combines the two pathways with nucleotides and nucleosides metabolism in the airway surface. D represents the signaling pathway in CF human epithelium.

Chapter 2). While on the airway surface, ATP binds to the purinergic receptor P2Y₂-R, which is a G-protein-coupled (G_q) receptor and activates its downstream target phospholipase C (PLC). Activated PLC hydrolyzes the membrane lipid phosphatidylinositol 4, 5-bisphosphate (PIP₂), producing inositol 1,4,5-trisphosphate (IP₃) and diacylglycerol (DAG). IP₃ is water-soluble and diffuses through the cytoplasm to the endoplasmic reticulum (ER), where it binds to and opens a channel that releases calcium from stores inside the ER. A calcium-sensitive chloride channel (CaCC) is then

activated and transports Cl^- ions from the cytoplasm to apical region. DAG, the other product of PIP_2 hydrolysis, interacts with both calcium and the protein kinase C (PKC) and mediates the chloride current through CFTR. This is the first pathway that not only up-regulates apical chloride currents by separate routes from PLC activation, but also inhibits ENaC due to the decrease in PIP_2 concentration [93-95]. The second pathway is initiated by adenosine (ADO) binding to the G-protein-coupled receptor A_{2b} . This receptor activates adenylyl cyclase (AC), which in turn raises the local concentration of intracellular cyclic-AMP (cAMP_i). cAMP_i activates protein kinase A (PKA), which by phosphorylation activates CFTR and inactivates the epithelial Na^+ channel (ENaC) [30]. There is evidence showing that activation of the epithelial Na^+ channel (ENaC) requires CFTR Cl^- channel function [96].

In CF airway epithelium, both the regulation of CFTR through PKC-dependent and cAMP_i -dependent pathways fail due to a lack of functional CFTR in apical membrane. However, the pathway of CaCC activation and ENaC remains intact and thus becomes a viable target for CF therapy. The regulation on these two types of ion channels by extracellular nucleotides and their metabolites has been shown to help recovery of the airway surface liquid (ASL) [97]. The signaling pathways acts like a link that ties extracellular nucleoti(si)des metabolism and the change of ion and water flow together. Therefore it is very important to study in detail the regulation of this pathway to enable the coupling of the two mathematical models described in the previous chapters.

Many previous studies have focused on this area. Paradiso and Boucher investigated $[\text{Ca}^{2+}_i]$ release and influx in polarized human nasal epithelial monolayers using ATP administration to stimulate P_2 purinoreceptors [98]. In Ca^{2+} -containing NaCl ringer solutions, ATP added to either the mucosal or serosal side induced an instant peak in $[\text{Ca}^{2+}_i]$. The intracellular calcium concentration then gradually decreased back to near the

basal levels. Ca^{2+} signaling was also studied in normal and CF human bronchial epithelial (HBE) by UTP and a similar intracellular calcium response was reported [99]. Cystic fibrosis airway epithelial Ca^{2+}_i signaling: the mechanism for the larger agonist-mediated Ca^{2+}_i signals in human cystic fibrosis airway epithelia.

The up-regulation of CaCC and down-regulation of ENaC have been studied together and separately in recent years. Mason *et al.* [100] studied the transepithelial short circuit current (I_{sc}), which reflects the regulation of both CaCC and ENaC in human normal and CF airway epithelium and presented representative tracings of the effect on I_{sc} of extracellular ATP applied to the apical or basolateral membrane. A study on the regulation of CaCC alone was conducted using the same cultures and pretreating the cells with amiloride to block ENaC. Measurements of the chloride current through CaCC resembled the Ca^{2+}_i response induced by extracellular ATP in either of the compartments. These two observations provide information on the individual responses of CaCC and ENaC. Later, measurements of the response for CaCC to UTP were reported by Tarran *et al.* [97], which showed a similar response to that of ATP but a bigger response in CF than normal murine tracheal epithelial (MTE) monolayers. This paper also showed evidence that CaCC plays a role in regulating ASL height in response to released agonists (e.g., mucosal nucleotides).

Despite a lot of research on signaling pathways in HNE cells, there is little work on HBE cells. Because our extracellular nucleotide and nucleoside metabolism model (Chapter 2) was built based on the measurements from HBE cells, we decided to use traditional bioelectrode techniques, i.e. modified perfusion Ussing chamber experiments, to investigate ion transport in these cells. And we used HBE cells from CF patients so that CaCC (Cl^- current) and ENaC (Na^+ current) pathways could be studied individually without any effect on I_{sc} from CFTR.

4.2 MICROELECTRODE STUDIES

To study how ATP affects ion and water flow across the membrane of epithelial cells, we designed a series of *in vitro* electrophysiological experiments to measure the regulation of ATP on the Calcium Activated Chloride Channel (CaCC) and Epithelial Na Channel (EnaC) individually. Initially, we wanted to qualitatively learn how ATP regulates these two channels. That is, how differently the channels respond to ATP, the time span of each response and how sensitive the channels are to an increasing dose of ATP. After more information was gathered, we studied ATP regulation quantitatively by measuring the dose response curves of ATP on the channels. These measurements characterize the interaction of ATP and mucosal membrane receptors and the signaling pathways they initiate. Therefore, this information is essential for integrating the biochemical network model and the ion/water flux model.

4.2.1 TISSUE CULTURING AND PREPARATION

All the cells used were CF bronchial epithelial cells. Bronchial specimens were obtained from CF subjects and removed for clinical reasons. All procedures were approved by the University of North Carolina Committee for the Protection of the Rights of Human Subjects.

Detachment from specimen/Thawing and plating

In brief, cells were detached from freshly resected specimens by incubation at 40°C in modified Eagle's medium (MEM) containing 0.1% Protease 14 (Sigma Chemical Co., St. Louis, MO) and 100 Mg/ml DNAase (Sigma Chemical Co.). Cells were isolated after 24-48 h by centrifugation (800 g), protease neutralized (10% FBS), after which the

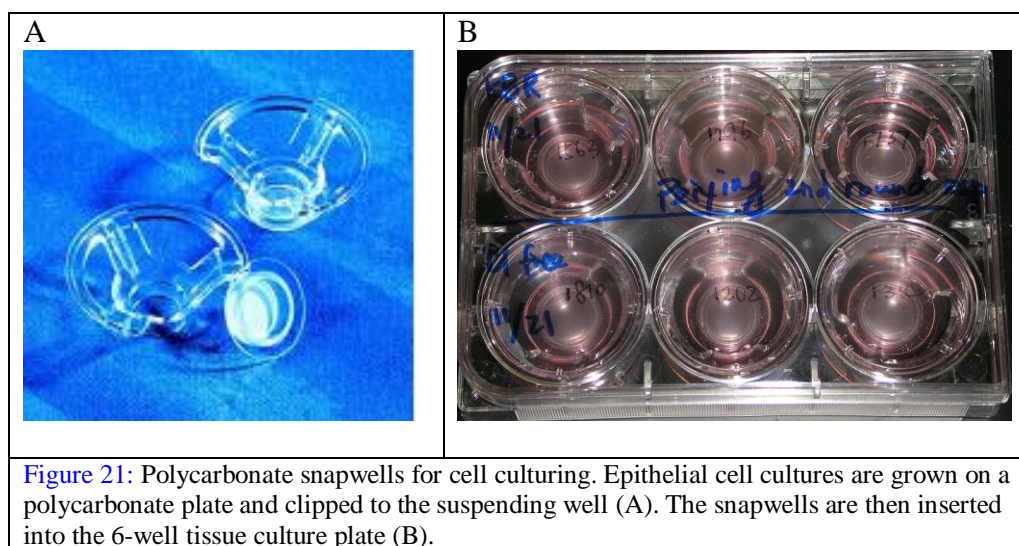
cells were washed twice in MEM and suspended in a base medium (Ham's F-12) that was supplemented with the following hormones and growth factors (F12-7Xm): insulin (5 pg/ml), cholera toxin (1 rig/ml), transferrin (7.5 pg/ml), hydrocortisone (10^{-6} M), triiodothyronine (T3, 3×10^{-8} M), endothelial cell growth substance (7.5 pg/ml), and retinoic acid (5×10^{-8} M). For those cells that were frozen before being used, they need to be thawed in 37 °C and then go through the same procedure above.

Human epithelial cells are considered to be precious since it's hard to get. Instead of being passaged to the snap-wells directly, freshly resected or previously frozen epithelial cells were firstly plated onto 100mm collagen coated (10mg Collagen type IV (Sigma C-7521 or Fisher # OB 1290-01S, .5mg/ml, 20 ml distilled water, 40ul concentrated Acetic Acid) plastic plates. The cells were washed every other day with phosphate-buffered saline (PBS) solution and then fed with BEGM. The total number of the cells increased through growing and dividing until cells became confluent (meaning they are densely distributed over the plate). By then enough number of cells were cultured for passaging to the snap-wells (0.25-0.3 millions cells/snap-well). This process might take a couple days to one week, and it makes sure that relatively small amount of cell cultures can be utilized for more experiments.

Passaging cells to snap-wells

After the cells reached confluence, the media was replaced with Trypsin solution containing 1mM EDTA and 0.1% trypsin (Sigma Chemical, St. Louis, MO) to detach the cells from the collagen coat. After incubation at 37 °C for 10 minutes, most cells were detached and were treated with an equal volume of Soybean Trypsin Inhibitor 1 mg/mL in F12 (STI) to neutralize Trypsin. The tube with the cell suspension was put into the

centrifuge at 1500RPM for 5 minutes. Then the supernatant was aspirated and re-suspended in the tube in a known volume of media (ALI for bronchial epithelial cells).



Cells were counted using Trypan Blue dye to determine viability before they were passaged onto substrata affixed to polycarbonate cups housed in six-well containers (Costar, Cambridge, MA) containing media in both basal and apical compartments. For the microelectrode studies, the substratum was a polymerized collagen sheet; for optical studies, it was a Falcon Cyclopore membrane (Becton Dickinson, Lincoln Park, NJ). The ideal amount of cells is approximately 0.25 million per snap-well. The media ALI is fed to both apical and basal compartments on the second day and then every other day until the cells reach confluence. After that, only the basal compartment needs media. Once a week cells were washed with phosphate-buffered saline (PBS) solution, which was aspirated after a few minutes. The cells were monitored daily by measurement of the transepithelial potential difference (V_t) using calomel electrodes interfaced to an electrometer (WPI EVO-M, Sarasota, FL). Cell preparations were routinely studied within 1-2 days of the development of the maximal V_t (21 ~28 days from passaging).

Depending on the time when epithelial cells are passaged, they are name as P0, the primary cells that are grown on the snapwells right after dissecting from specimen, P1, the primary cells after one passage to the 10mm plate and then to the snapwells, and P2, cells passaged twice in 10mm plate before growing in the snapwells. For bronchial epithelial cells from human lungs, they can be at most passaged twice before moving to the snapwells. Some research shows that the surface metabolism of ATP on cultured human airway epithelia decays through passage, and is reduced by more than 50% in passage 2 cells (Picher, M., pers. comm.) Therefore we also conducted a contrast study for different cell passage type in the experiments.

4.2.2 SOLUTIONS AND DRUGS

For the study of chloride currents, the epithelia were mounted in Ussing Chambers with Krebs-bicarbonate Ringer (KBR; in mM, 140 Na^+ , 120 Cl^- , 5.2 K^+ , 25 HCO_3^- , 2.4 HPO_4^{2-} , 0.4 H_2PO_4^- , 1.1 Ca^{2+} , 1.2 Mg^{2+} , and 5.2 gram glucose) on both the apical and basolateral sides. KBR solution resembles the fluid environment of the airway surface liquid and blood on top and underneath bronchial epithelial cells in human lungs. The CF lungs also have this property. Amiloride (Sigma) was present in the apical bath of all the experiments at 10^{-4} M to inhibit sodium absorption before addition of ATP, as it's an inhibitor of sodium channel ENaC (there is little sodium current through the basolateral membrane). Different concentrations of ATP were dissolved in KBR at 10^{-2} or 10^{-1} M and diluted into the appropriate bath. After this procedure, all the measured trans-epithelial current comes from chloride transport through CaCC, because 1) CFTR is mutated in the CF epithelial cells; 2) there are no potassium channel present in the apical membrane; 3) the apical and basal bath have the same composition so there will be no contribution of transepithelial current coming from shunt compartment.

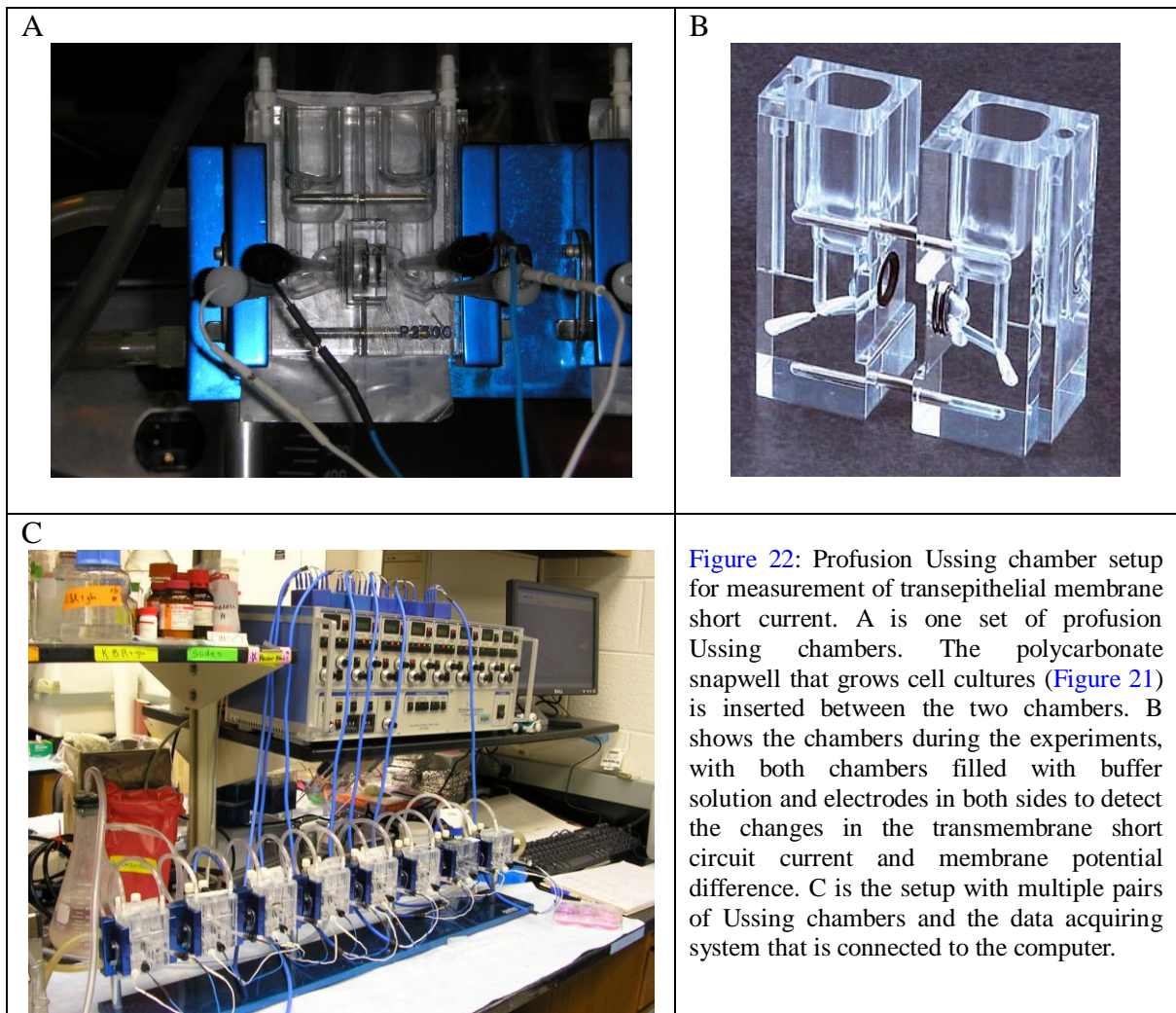
Chloride-free KBR was used in the study of sodium currents in order to distinguish from chloride currents. The only difference of this solution is the replacement of chloride ions with gluconate. To get rid of the influence of the chloride out flux from intracellular compartment, the epithelia needed to be mounted for at least 30 to 40 minutes before adding ATP.

Although potassium channels are rare in the apical membrane, postassium currents were observed in some epithelia after adding ATP [102]. Chloride-free KBR was then modified to include 5mM Ba^{2+} to inhibit potassium channel. Since Ba^{2+} reacts with SO_4^{2-} in the original solution and precipitates, the latter was replaced with Gluconate. (Protocols of making KBR, Chloride-free KBR and Chloride-free KBR with 5mM Ba^{2+} are shown in the appendix III)

4.2.3 USSING CHAMBERS

Polycarbonate Ussing chambers were milled to fit the plastic cups that supported the permeable collagen matrix on which the cells were grown, as described previously. The luminal and basolateral sides of the cultures were continually perfused with solutions that were warmed (37 °C) and gassed (95% O_2 -5% CO_2). Primary cultures were mounted vertically in modified Ussing chambers for the measurement (VCC 600 voltage clamp; Physiological Instruments, San Diego, CA) of transepithelial potential difference (V_t). The electrical potential of the basolateral side of the tissue with respect to the apical side was defined as positive.

The transepithelial PD (V_t) was measured by calomel electrodes connected to the half-chambers via 3M KC1 agar bridges. The luminal bridge served as the common ground for the macro- and microelectrode systems. A second pair of 3 M KC1 agar



bridges connected a pair of Ag-AgCl electrodes to the bath, which permitted passage of 0.5-s current pulses (I , $\sim 40 \text{ microAmp.cm}^{-2}$) every 6 s with a duration of 0.5 s via a stimulator [World Precision Instruments (WPI), 301-T] connected to a stimulus-isolation unit (WPI, 305). The transepithelial resistance (R_t) was calculated from the ohmic relationship between the deflection of V_t and the current passed. The equivalent short-circuit current (I_{eq}) was obtained from V_t and R_t according to Ohm's Law and continuously recorded (Acquire; Dataq Instruments) and stored on a computer hard drive. Because the transepithelial current voltage relationships are linear and time independent in the physiologic range of potentials, the I_{eq} accurately estimates the true short circuit current I_{sc} .

All protocols started with the measurement of the basal current I_{eq} , defined as a steady-state (< 5 % change) value for > 5 min, followed by drug additions. Drugs were added from concentrated stock solutions to either apical and/or basolateral bathing solutions. All compounds were added cumulatively, i.e., drugs were not removed before addition of subsequent doses or compounds.

4.2.4 MEASUREMENT OF TRANSEPITHELIAL CURRENTS WITH APICAL EXOGENOUS ATP

Since all the epithelial cells we used were from CF specimen with mutated CFTR and didn't perform its normal functions. Therefore what was measured was the chloride current through Calcium-Activated Chloride Channel (CaCC). Previously, experiments have shown that a certain concentration of ATP will stimulate the CaCC and increase the apical chloride permeability. To study the dose-response relationship between ATP and chloride current through CaCC, a single dose of ATP (10^{-9} to 10^{-4} M) was added to the apical side of solution for each set of chambers. The fashion of desensitization was studied by applying cumulative doses of ATP (10^{-9} to 10^{-4} M). The reason for the choice of the dose range is that 10^{-9} M (nanomolar) is the *in vivo* steady state level of ATP in the airway surface of human lungs while 10^{-4} M is a pharmacological level. The protocol for current measurements with cumulative doses of ATP not only helps us to understand current desensitization, but also provide more experimental data for single-dose measurements. The collection of the data from each chamber when their first dose of ATP is added is actually a single-dose measurement.

To measure the sodium current across the epithelial, the cell cultures were initially bathed with KBR solution and then switched to chloride-free KBR solution in both apical

Events	Chamber # 1	Chamber # 2	Chamber #3	Chamber # 4	Chamber # 5	Chamber #6	Chamber #7 **	Chamber #8 **
Amiloride (M)*	√	√	√	√	√	√	√	√
ATP	10 ⁻⁹ M	10 ⁻⁸ M	10 ⁻⁷ M	10 ⁻⁶ M	10 ⁻⁵ M	10 ⁻⁴ M	Control	Control

Table 7: Experimental scheme for measuring the chloride current with single doses of ATP in the apical side of the bronchial epithelium cells from CF lungs. 10⁻⁴M of amiloride was added to the apical side of epithelium to block sodium channel ENaC. Different doses of ATP were added to each chamber afterward to measure the induced transmembrane chloride current. Chamber #7 and #8 were used as control. The concentration shown in the table presents the level of the agents (amiloride or ATP) in the paical compartment AFTER each dose event, NOT the concentration added.

Events	Chambe r # 1	Chambe r # 2	Chambe r #3	Chambe r # 4	Chambe r # 5	Chambe r #6	Chambe r #7 **	Chambe r #8 **
Amiloride (M)*	√	√	√	√	√	√	√	√
ATP (10 ⁻⁹ M)*	√						Control	Control
ATP (10 ⁻⁸ M)*	√	√					Control	Control
ATP (10 ⁻⁷ M)*	√	√	√				Control	Control
ATP (10 ⁻⁶ M)*	√	√	√	√			Control	Control
ATP (10 ⁻⁵ M)*	√	√	√	√	√		Control	Control
ATP (10 ⁻⁴ M)*	√	√	√	√	√	√	Control	Control

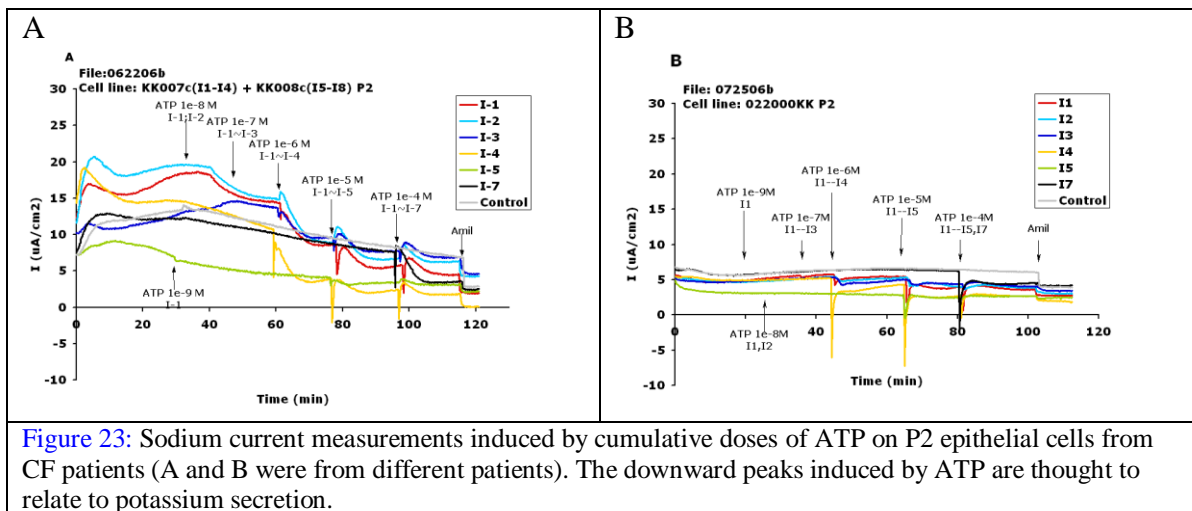
Table 8: Experimental scheme for measuring the chloride current with cumulative doses of ATP in the apical side of the bronchial epithelium cells from CF lungs. 10⁻⁴M of amiloride was added to the apical side of epithelium to block sodium channel ENaC. Increased doses of ATP were added to a single chamber afterward to measure the induced transmembrane chloride current and desensitization. Different chamber starts with different initial dose of ATP. Chamber #7 and #8 were used as control. The concentration shown in the table presents the level of the agents (amiloride or ATP) in the paical compartment AFTER each dose event, NOT the concentration added.

and basolateral compartments to eliminate the chloride current from measurement.

However, at least 40 minutes was needed for the intracellular chloride (~40 mM) to diffusion through the cytoplasmic membranes and I_{eq} to reach steady state. The I_{eq} measurements performed afterward were less affected by the chloride flux and could be considered as solely the sodium currents. 10⁻⁴M of amiloride was added to the chambers after the transmembrane current reached a new equilibrium to check if what we measured is mainly the sodium current.

Experimental evidence shows that ATP not only up-regulates CaCC but also acts as inhibits ENaC. In this way, the enhanced salt (Na⁺ and Cl⁻) level drives water flowing from cytoplasm to the apical side. This motivated the study of dose-response relationship

between ATP and sodium current through ENaC. Because ENaC reacts slower than CaCC (the shape of the peak and the relaxation time) upon ATP addition, two different types of experiments were done. Some of the earlier experiments showed that in bronchial epithelial cells from certain patients, ATP not only up-regulates ENaC, but also induces potassium secretion [103]. In several of sodium current measurements we performed, a downward peak was observed after ATP induction (Figure 23), which is thought to be a transepithelial outflow of potassium ions from cytoplasm.



The experiment schemes (Table 9 and 10) studies how single- and cumulative- dose of ATP with different concentrations affect the sodium currents.

Events	Chamber # 1	Chamber # 2	Chamber #3	Chamber # 4	Chamber # 5	Chamber #6	Chamber #7	Chamber #8
ATP (M)*	10^{-9}	10^{-8}	10^{-7}	10^{-6}	10^{-5}	10^{-4}	10^{-3}	Control
Amiloride (M)*	10^{-4}	10^{-4}	10^{-4}	10^{-4}	10^{-4}	10^{-4}	10^{-4}	10^{-4}

Table 9: Experimental scheme for measuring the sodium current with single dose of ATP in the apical side of the bronchial epithelium cells from CF lungs. The epithelial cells from CF patients were bathed in the Cl-free KBR solution until the transmembrane current reached equilibrium. Different doses of ATP were then added to each chamber to measure the change in transmembrane sodium current. 10^{-4} M of amiloride was added to the apical epithelium to check if the measured current was mainly through sodium channels.

Events	Chamber # 1	Chamber # 2	Chamber #3	Chamber # 4	Chamber # 5	Chamber #6	Chamber #7 **	Chamber #8 **
ATP (10^{-9} M)*	√						Control	Control
ATP (10^{-8} M)*	√	√					Control	Control
ATP (10^{-7} M)*	√	√	√				Control	Control
ATP (10^{-6} M)*	√	√	√	√			Control	Control
ATP (10^{-5} M)*	√	√	√	√	√		Control	Control
ATP (10^{-4} M)*	√	√	√	√	√	√	Control	Control
Amiloride (M)*	√	√	√	√	√	√	√	√

Table 10: Experimental scheme for measuring the sodium current with cumulative doses of ATP in the apical side of the bronchial epithelium cells from CF lungs. Increased doses of ATP were added to a single chamber to measure the induced transmembrane chloride current and desensitization. 10^{-4} M of amiloride was added to the apical epithelium to check if the measured current was mainly through sodium channels.

To simulate a situation that is similar to what happens *in vivo*, a third type of experiments was designed to measure the sodium current through ENaC and chloride current through CaCC together. In this case, epithelial cells will be mounted bilaterally in KBR solution and 10^{-4} M amiloride will be added in apical side following the dose of ATP. We only conducted single-dose experiments on this system.

Events	Chamber # 1	Chamber # 2	Chamber #3	Chamber # 4	Chamber # 5	Chamber #6	Chamber #7	Chamber #8
ATP (M)*	10^{-9}	10^{-8}	10^{-7}	10^{-6}	10^{-5}	10^{-4}	10^{-3}	Control
Amiloride (M)*	10^{-4}	10^{-4}	10^{-4}	10^{-4}	10^{-4}	10^{-4}	10^{-4}	10^{-4}

Table 11: Experimental scheme for measuring the transmembrane current that is composed of both sodium and chloride ions. The epithelial cells from CF patients were bathed in the regular KBR solution. Different doses of ATP were then added to each chamber to measure the change in transmembrane sodium current. 10^{-4} M of amiloride was added to the apical epithelium afterward to check the ratio of chloride current and sodium current.

4.3 EXPERIMENTAL RESULTS WITH ATP

4.3.1 MEASUREMENT OF CHLORIDE CURRENT

To get a basic idea about the response of CaCC to ATP using both a single dose and cumulative doses, we initially conducted cumulative doses experiment multiple times,

because this method not only provides single-dose data but also information on desensitization. We measured the chloride current with cumulative stimulation of ATP ranging from 10^{-9} M to 10^{-4} M several times on P1 cells (for details see 4.2.1). As shown in [Figure 23](#), it seems that the chloride channel CaCC starts to be effectively activated by ATP when its concentration is higher than 10^{-6} M (micro-Molar). This observation helps us to adjust our protocols for chloride current measurements to exclude the ATP doses under 10^{-6} M at later times. Doses higher than 10^{-4} M are beyond the pharmacological range and will be less useful for our study. So in the end the ATP doses we induced in the experiments are 10^{-6} , 10^{-5} and 10^{-4} M.

In general, the chloride current follows a quick drop in response to apical amiloride and remains at the lower level for the entire course of the experiment, which shows that amiloride binds to sodium channel in a very fast and tight way. The typical response to a single dose of ATP is a sharp peak (quick increase and decrease) within the first a few minutes. The peak later becomes wider and returns to a level that is very close to the one before adding ATP in 10~30 minutes, depending on the concentration of the dose. As the level of ATP increases, so does the relative height of the peak.

The experiments with cumulative doses indicate different rates of desensitization in P1 and P2 cells. Most of P1 cells and some of P2 cells have increase in peak on the second dose (10^{-5} M) and a huge reduction of the peak after the third one (10^{-4} M). The rest of P2 cells show a consistent reduction in peak after the increasing doses. We also found that the absolute values of response in most P2 cells are bigger than those from P1's. These two lines of evidences indicate that CaCC in P2 cells are more sensitive to ATP than P1's, so that it not only has a bigger response to each dose, but also becomes desensitized at a lower dose (10^{-5} M).

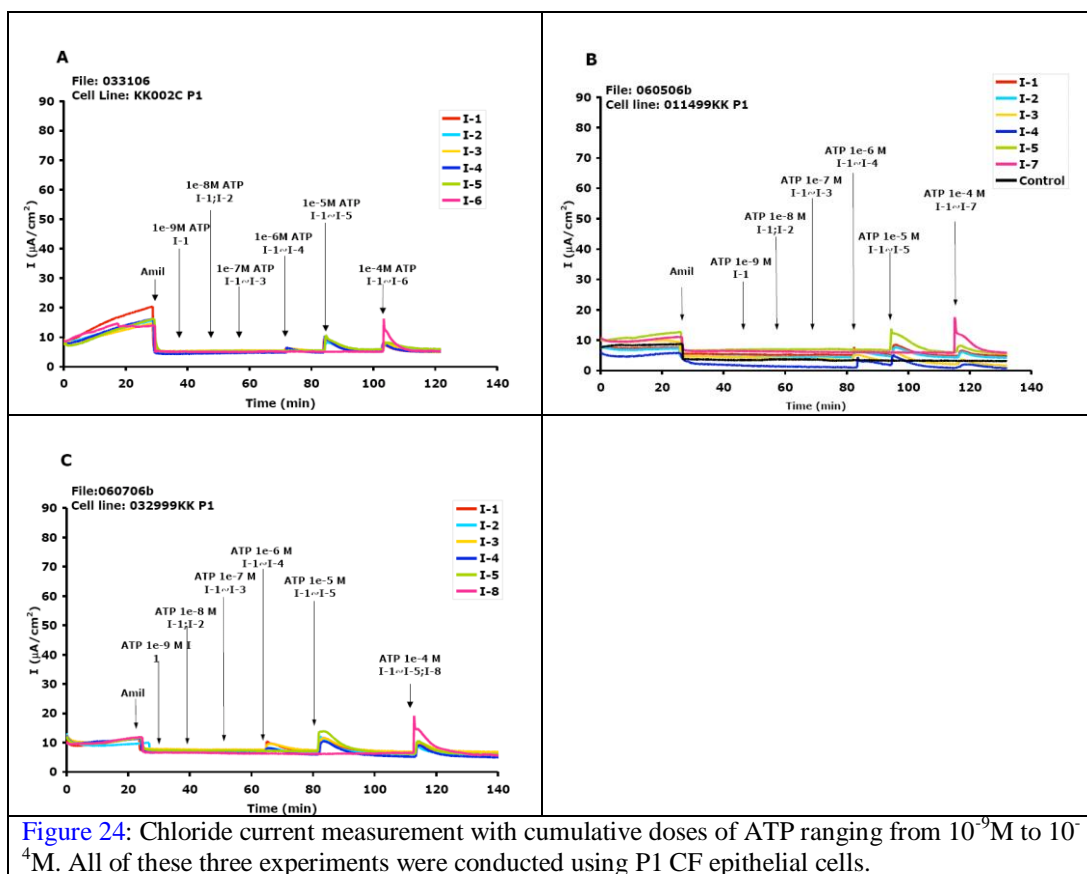


Figure 24: Chloride current measurement with cumulative doses of ATP ranging from 10^{-9} M to 10^{-4} M. All of these three experiments were conducted using P1 CF epithelial cells.

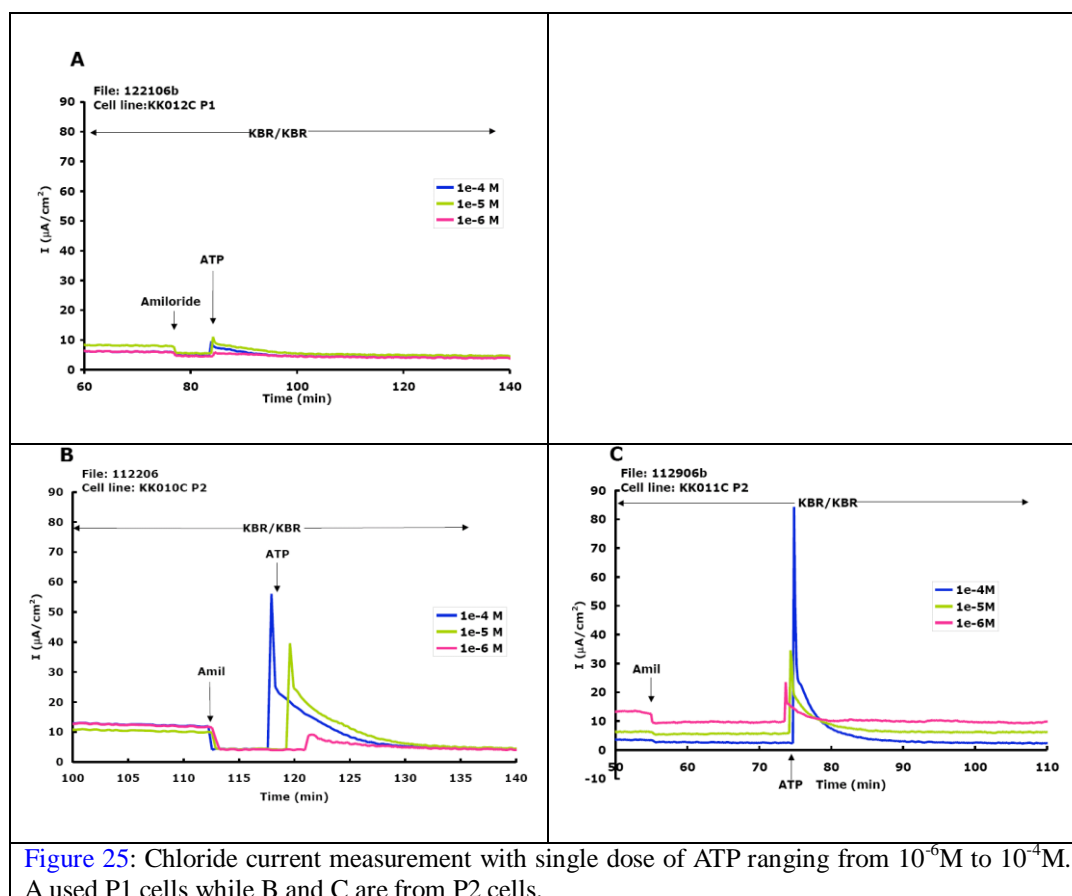


Figure 25: Chloride current measurement with single dose of ATP ranging from 10^{-6} M to 10^{-4} M. A used P1 cells while B and C are from P2 cells.

Besides the qualitative analysis of CaCC response to apical ATP (the shape of reponse, and time span), we also studied quantitatively the different aspects of the response. Two key questions we addressed in both types of experiments are: 1) whether the chloride current returns to its basal level following the addition of ATP; 2) what is the correlation between the response and the concentration of ATP. The first one addresses the concern that the signal initiated by ATP permanently changes the permeability of CaCC. The second question is obviously more important for studying the dose response relationship, which serves as a tie for integrating the biochemical network model (Chapter 2) with the ion/water flux model (Chapter 3). With this motivation, we first calculated the relative change of steady state level of the current before and after ATP addition (the first group of bars in [Figure 27A and B](#)) and the relative height of the peak induced by ATP (the second group of bars in [Figure 27A and B](#)) based on the data from experiments with single dose of ATP. The relative baseline was obtained from

$$\left(I_{new,ss} - I_{old,ss} \right) / I_{old,ss} \times 100\% \quad (4.1)$$

where “ss” stands for steady state. Similarly, the relative height of peaks was calculated as

$$\left(I_{peak} - I_{old,ss} \right) / I_{old,ss} \times 100\% \quad (4.2)$$

As the data in [Figure 27](#) show, the chloride current, on average, comes back to the previous baseline level after being induced by ATP within 30 minutes. And as the level of ATP increases, so does the relative height of the peaks. Although [Figure 27A](#) shows a rather small

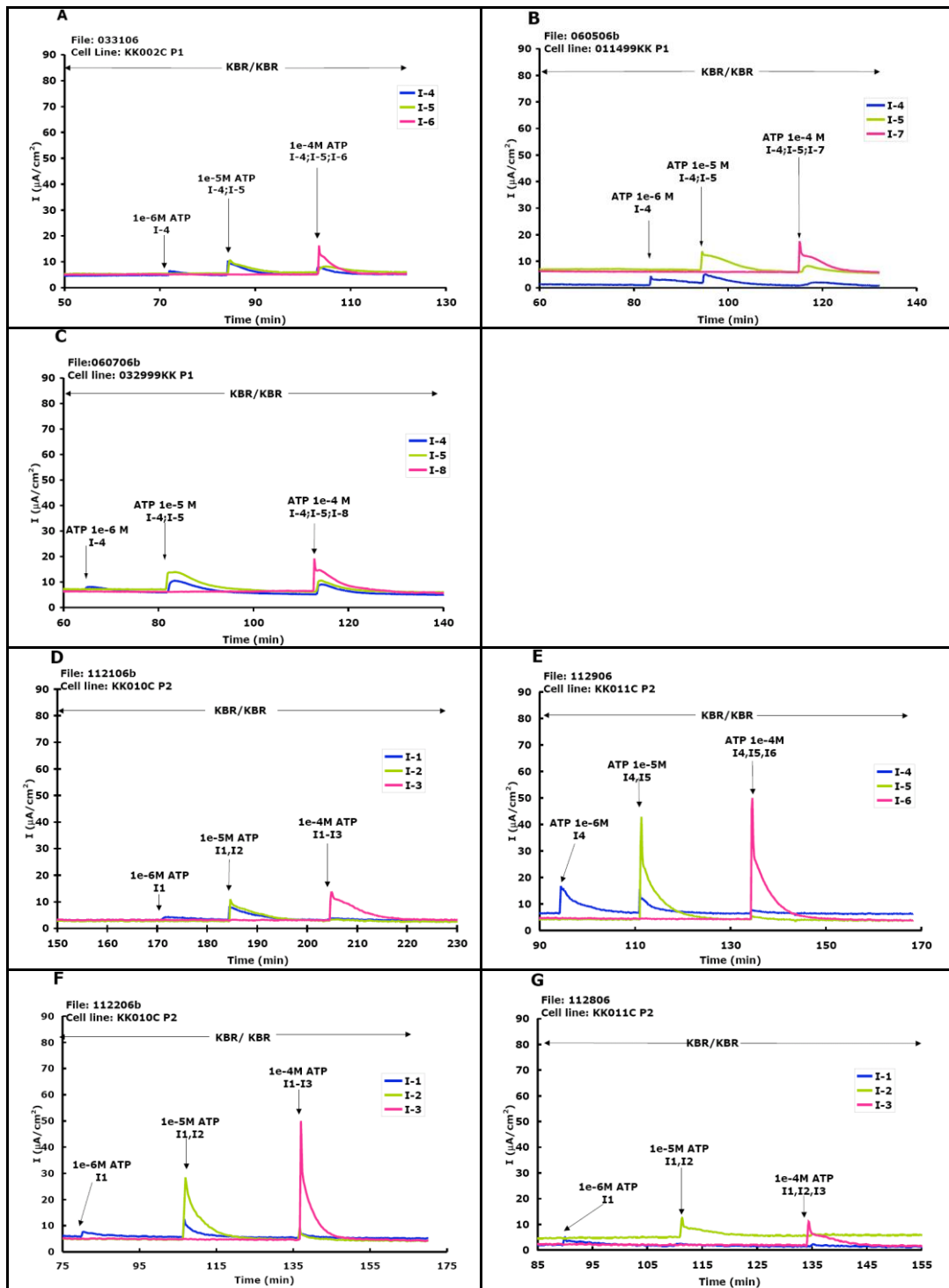
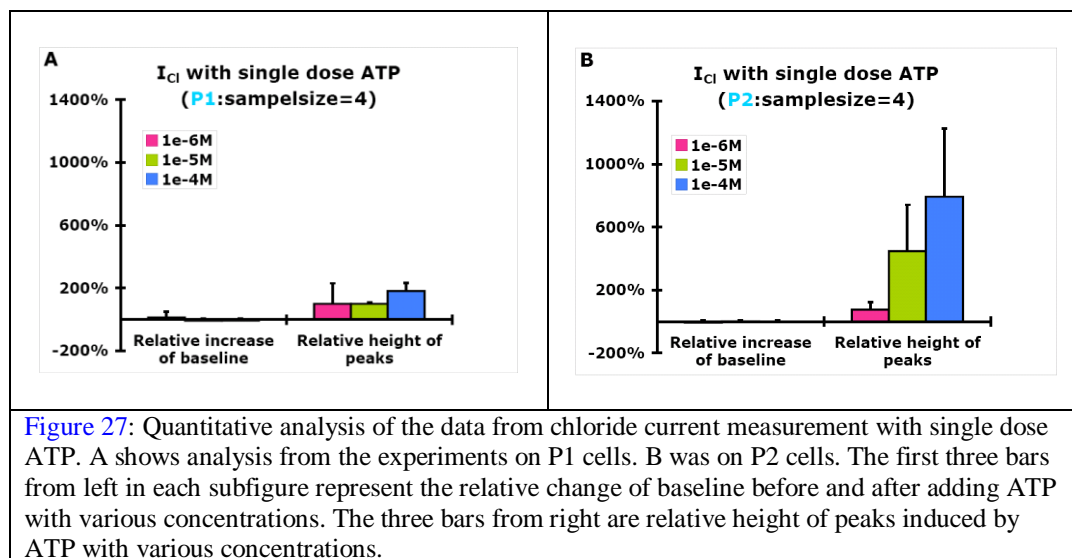


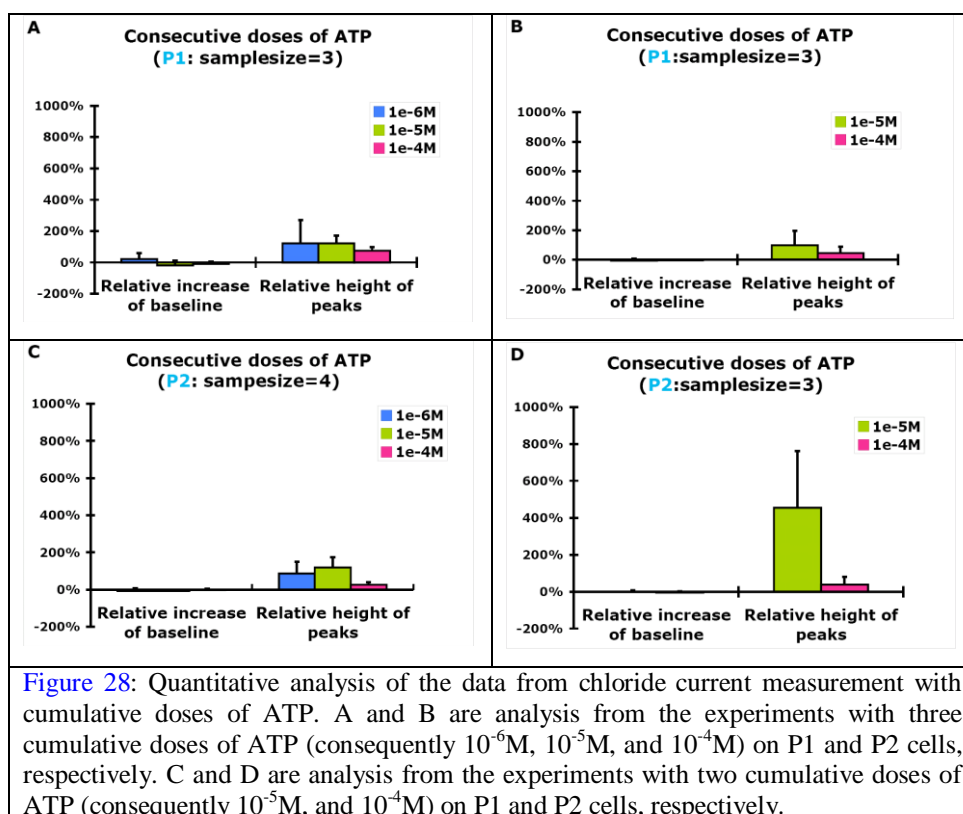
Figure 26: Chloride current measurement with cumulative doses of ATP ranging from 10^{-6} M to 10^{-4} M. A, B and C were obtained from P1 cells while D, E, F, G are from P2 cells. Notice all the figures are cut off from the moment after the apical side is induced with 10^{-4} M amiloride.

difference between dose 10^{-6} , 10^{-5} and 10^{-4} M in P1 cells, data from P2 cells (Figure 27B) indicate a very significant difference in the response to different doses. Although the sample size is still relatively small, this observation gives some hints that as cell passage

type varies, the dose response curve varies too. For example, in P1 cells, the dose response might have a jump at 10^{-4}M while in P2 cells. There is probably a steady increase right from 10^{-5}M all the way to 10^{-4}M .

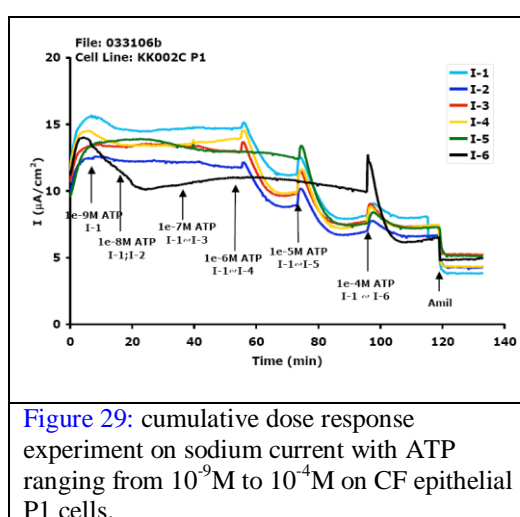


We also applied the same data analysis to experiments with cumulative doses of ATP. Two scenarios were studied: the experiments with three cumulative doses (consequently 10^{-6}M , 10^{-5}M , and 10^{-4}M), and ones with only two (consequently 10^{-5}M , and 10^{-4}M). When studied in an averaged fashion, data from the three-dose experiments show a very similar trend in the relative height of peaks on both P1 and P2 cells. That is, the chloride channel CaCC is desensitized gradually and has a big collapse after 10^{-5}M . Comparison of [Figure 28C and D](#) indicates again P2 cells are more sensitive to a given concentration of ATP in a certain range ($>10^{-7}\text{M}$, other wise no response whatsoever) than P1 cells, although the channels are desensitized back to the same level after 10^{-5}M .



4.3.2 MEASUREMENT OF SODIUM CURRENT

To briefly learn the response of sodium channel regulation by ATP, we conducted a cumulative dose-response experiment on P1 cells (Figure 29).



We observed a similar dose response range to ATP as in chloride current case. That is, doses lower than 10^{-6} M have little effect on the sodium current via ENaC channel. So we modified the experimental plan (4.2.4) of single dose- and cumulative dose-response experiments to use ATP with a smaller range from 10^{-6} M to 10^{-4} M. As shown in [Figure 29](#), the response of ENaC to ATP is different from that of CaCC in the following aspects ([Figure 24](#)): 1) The peak induced by the same dose of ATP within the first minute or two is much shorter. 2) On average the current reaches its minimum with in approximately 15 minutes after the dose of ATP. The minimum is always below the baseline. 3) After reaching a minimum value, the current either stays there or recovers back to a lower baseline. Although we don't have enough data from P1 cells for this type of experiments, the amplitude of peaks from data on P1 cells ([Figure 30A](#)) and P2 cells ([Figure 30B, C, D, E](#)) indicates that ENaC in P2's are possibly more sensitive to ATP. The drop of the current induced by 10^{-4} M amiloride, in comparison with the change in chloride current experiments, is quite small. That shows that ATP doses from 10^{-6} to 10^{-4} are able to turn off most of ENaC's in apical membrane. The quantitative analysis on data in [Figure 31](#) and collected data from cumulative dose-response experiments in [Figure 4.14](#) shows a similar inhibition effect in the relative change of baseline (three bars from left in [Figure 31](#)) for the three doses. Similar to the chloride current experiments, the peaks induced by ATP for different doses (middles group in [Figure 31](#)) increases as the dose increases. Although the recover is very significant from [Figure 30F](#) and [Figure 32A](#), the quantitative analysis (three bars from right in [Figure 31](#)) indicates a very small recovery on average, the definition of which is as follows:

$$\left(I_{new,ss} - I_{min} \right) / I_{new,ss} \times 100\% \quad (4.1)$$

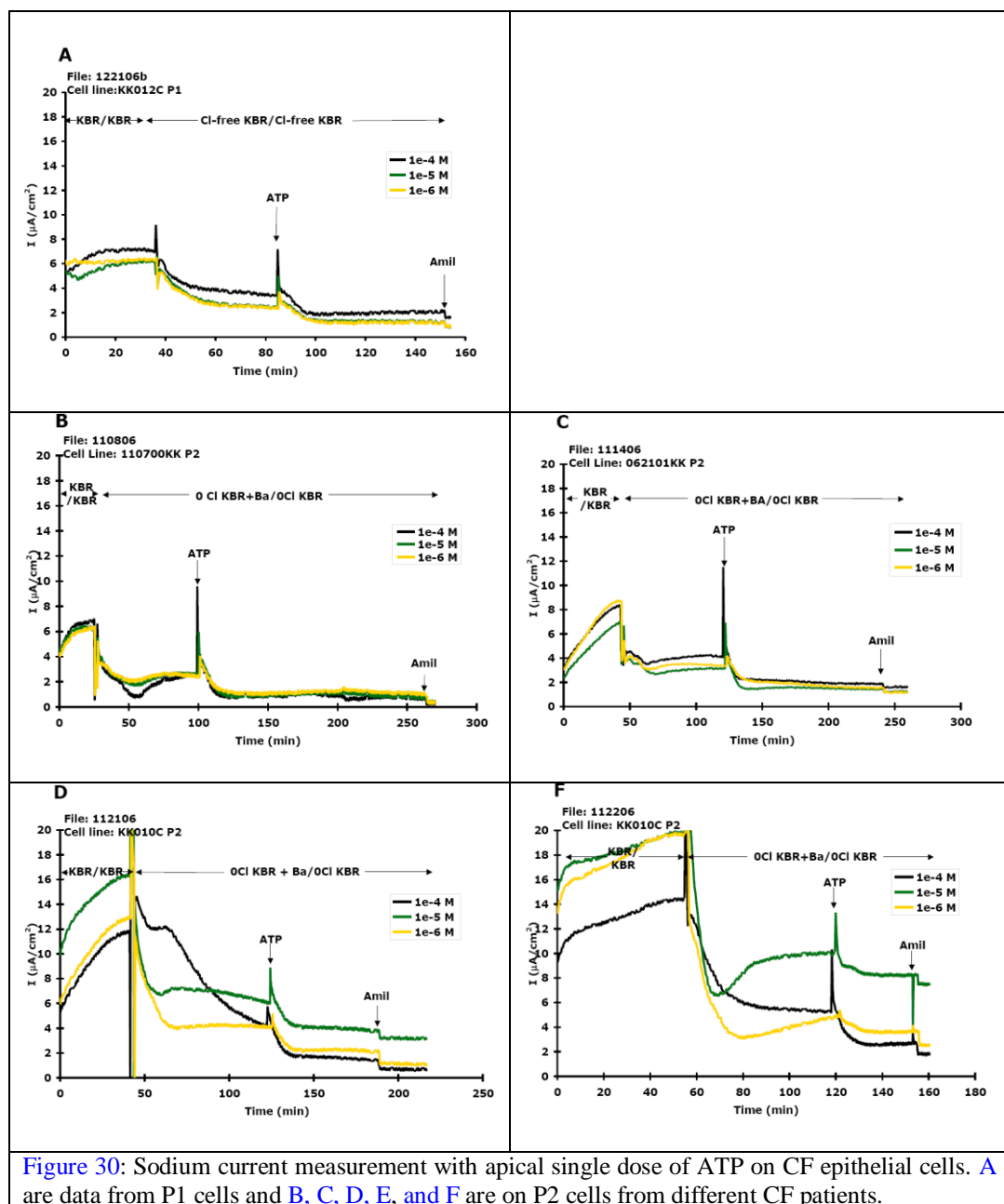


Figure 30: Sodium current measurement with apical single dose of ATP on CF epithelial cells. **A** are data from P1 cells and **B, C, D, E, and F** are on P2 cells from different CF patients.

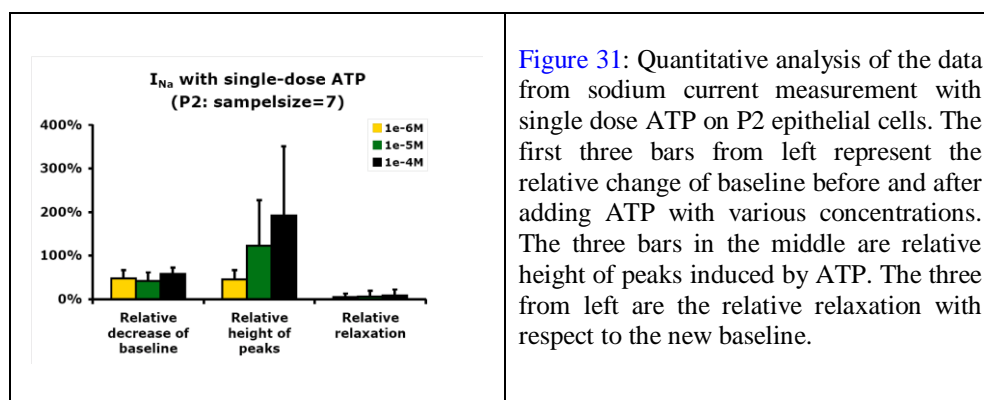


Figure 31: Quantitative analysis of the data from sodium current measurement with single dose ATP on P2 epithelial cells. The first three bars from left represent the relative change of baseline before and after adding ATP with various concentrations. The three bars in the middle are relative height of peaks induced by ATP. The three from left are the relative relaxation with respect to the new baseline.

We observe desensitization of ENaC by cumulative doses of ATP in Figure 32. The data analysis in Figure 33 also confirms this. Interestingly, the cumulative doses not only desensitize the response shown by the peaks (middle group in Fig 33A and B), but also the change of baseline (bars from left in Figure 33A and B). Because there is only one experiment done on P1 cells, we only could conclude that the recovery for P2 cells in this type of experiments is hardly noticeable.

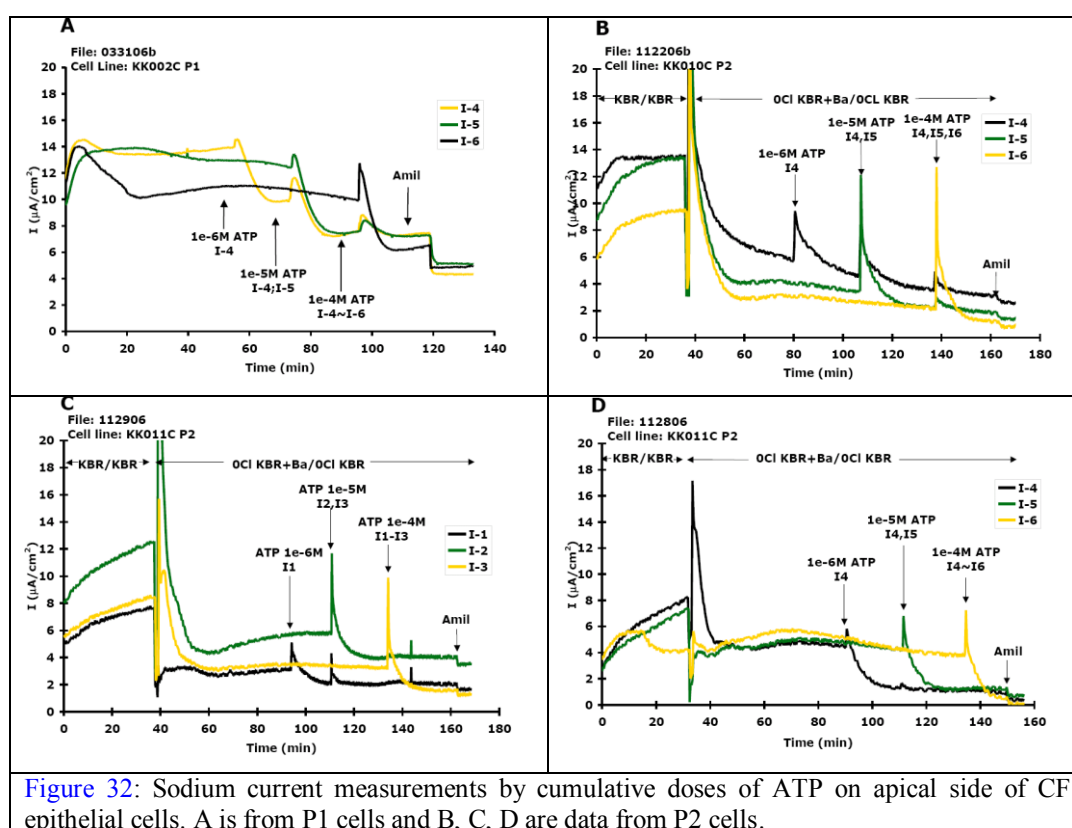


Figure 32: Sodium current measurements by cumulative doses of ATP on apical side of CF epithelial cells. A is from P1 cells and B, C, D are data from P2 cells.

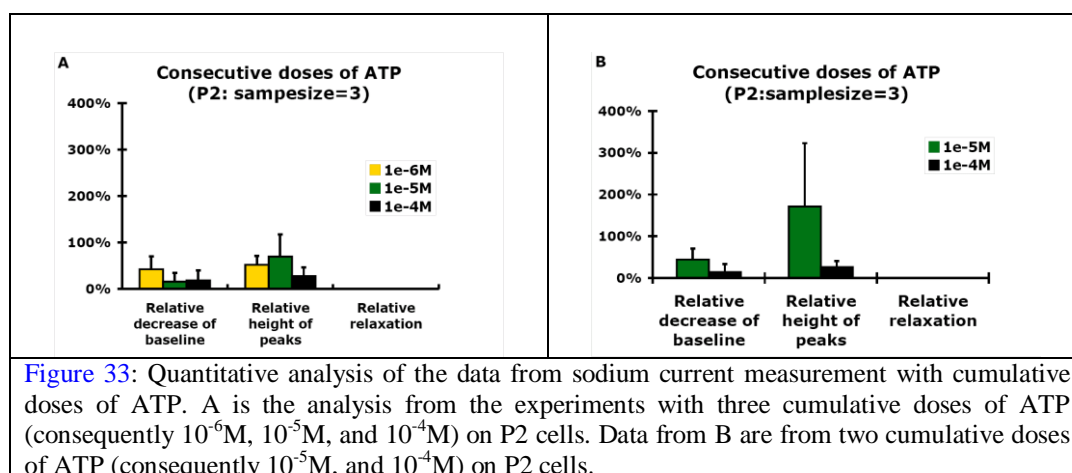
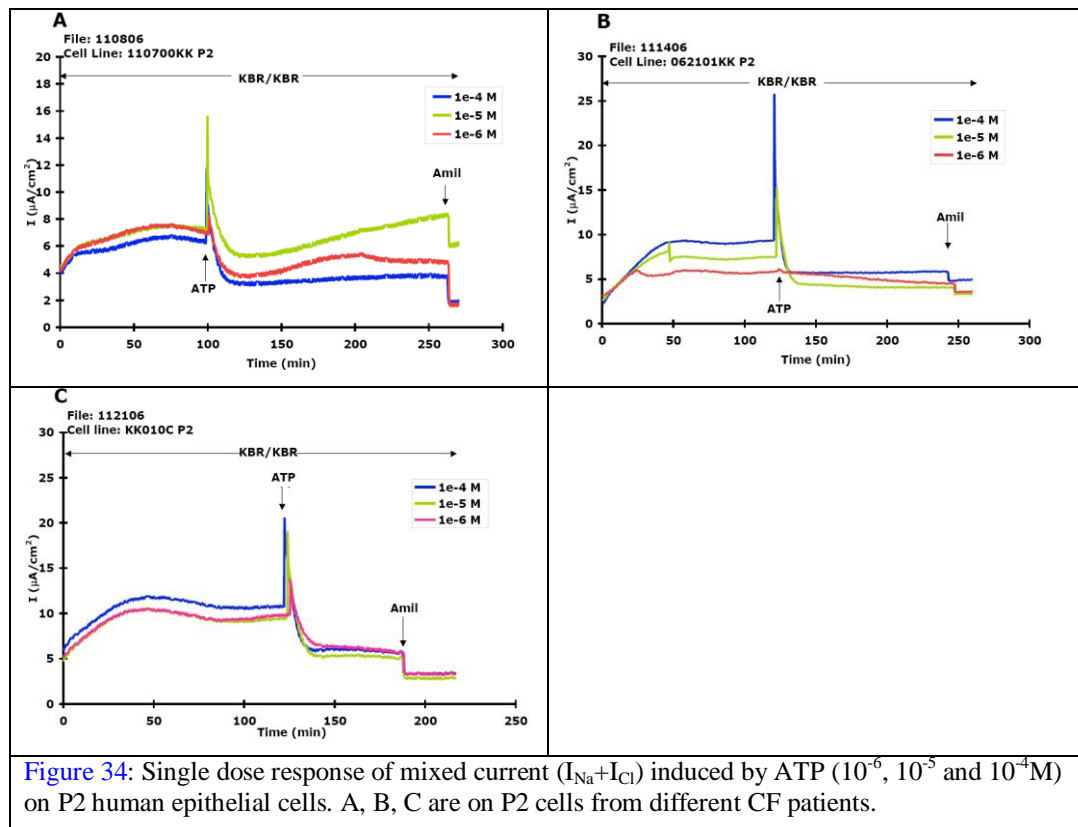


Figure 33: Quantitative analysis of the data from sodium current measurement with cumulative doses of ATP. A is the analysis from the experiments with three cumulative doses of ATP (consequently 10^{-6} M, 10^{-5} M, and 10^{-4} M) on P2 cells. Data from B are from two cumulative doses of ATP (consequently 10^{-5} M, and 10^{-4} M) on P2 cells.

4.3.3 MEASUREMENT OF MIXED CURRENTS

Our experience from previous experiments, which studied sodium channel (ENaC) and chloride channel (CaCC) individually, helps us to narrow the dose of ATP to 10^{-6} to 10^{-4} M for the mixed currents. We observed combined characteristics from both ENaC and CaCC responses induced by ATP in Figure 34. The chloride current obviously plays an important role in the response induced immediately following the addition of ATP, because the peak is much higher than those of ENaC response. However, regulation of the sodium channel has a much longer effect on the total measurements. That's why we see the minimum point that is much lower than the baseline (Figure 34B and C) and sometimes a recovery at higher doses like 10^{-4} M and 10^{-5} M (Figure 34A).



4.3.4 FACTORS THAT AFFECT THE MEASUREMENTS

Our previous observations made us wonder about the several different factors in these experiments that might affect the outcome. First of all, we wanted to learn whether the chloride-free KBR buffer with 5mM barium does anything other than inhibiting potassium secretion and secondly how the cell passage type affects measurements of sodium and chloride currents. Notice the baseline current for both I_{Na} and I_{Cl} are relatively low ($5\sim 10\ \mu A/cm^2$), which makes the study of dose response relationships, especially the sodium current recovery, very hard. The low baseline makes the recovery, if there is any, seem very small. Because dexamethasone, a hormone, has been shown to upregulate ENaC mRNA expression [104], we used it as a pretreatment for the cell cultures. The pretreatment with Dexamethasone in the media starts after two weeks of cell culturing and lasts normally 3 days. Pretreatment with a longer period is also tested in our experiments.

To test how the buffer and cell passage type make a difference in the measurements, we got P0, P1 and P2 cells from the same cell line and conducted sodium and chloride current measurements on each of them. In each sodium current experiment, we also tried to run the cells with same ATP dose in different buffers, one in bilateral Cl-free KBR with 5mM barium and one without barium.

With the pretreatment of Dexamethasone, a 5 to 8 fold of increase in the current baseline was observed in sodium current measurements ([Figure 35](#)). However the increase in baseline was not found in the chloride currents. This confirms that Dexamethasone is able to selectively up-regulate apical ENaC. Meanwhile, a recovery in sodium current measurement is observed ([Figure 35](#)). The higher the dose is, the more obvious the recovery. Comparison of the two curves in each subfigure of [Figure 35](#) shows

no significant difference that 5mM barium makes in the buffer. And if we compare the columns, which represent the same dose of ATP but in different cell types, cell passage type didn't affect the outcome very much. We observed a slightly different behavior for chloride currents (Figure 36). As we would expect, Dexamethasone didn't over express CaCC response to ATP. The baseline current is really low ($<5\mu\text{A}/\text{cm}^2$). Meanwhile it seems that P2 cells are at a higher baseline than P1's and P0's. The response of CaCC to ATP in P2 cells is higher than the other two types as well.

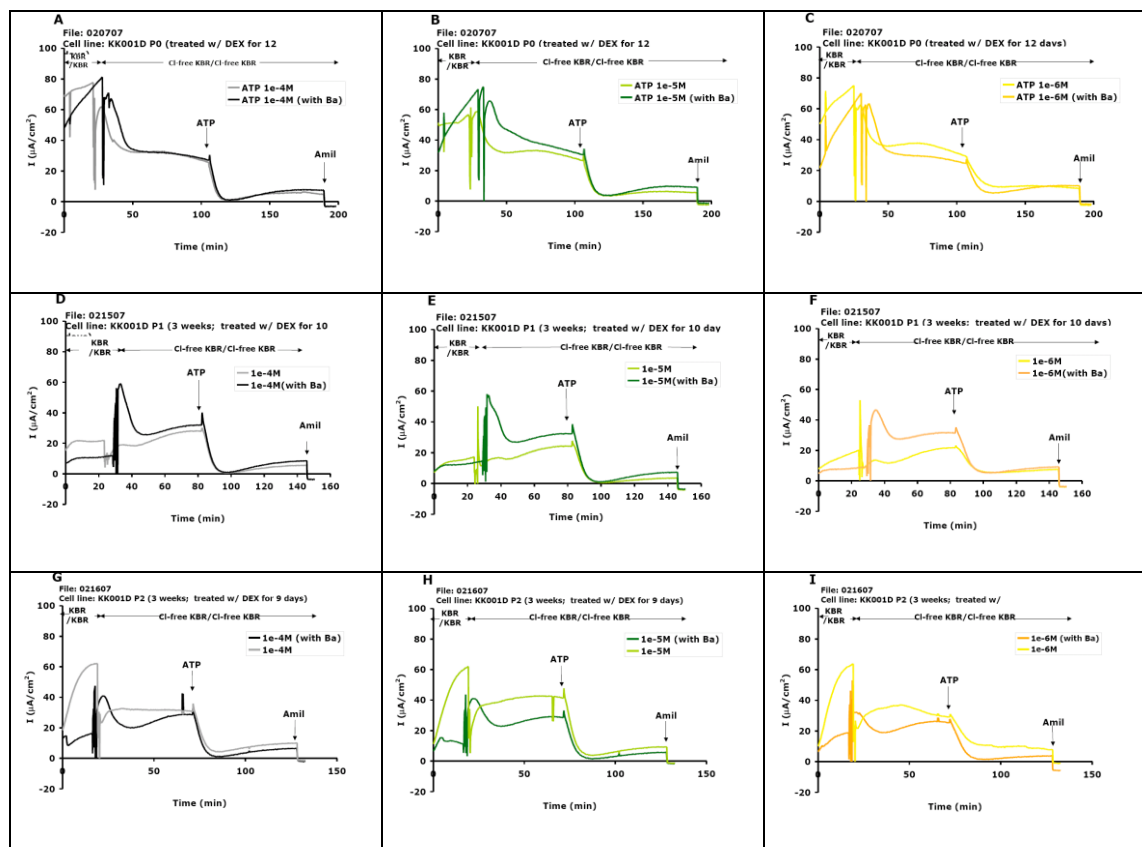
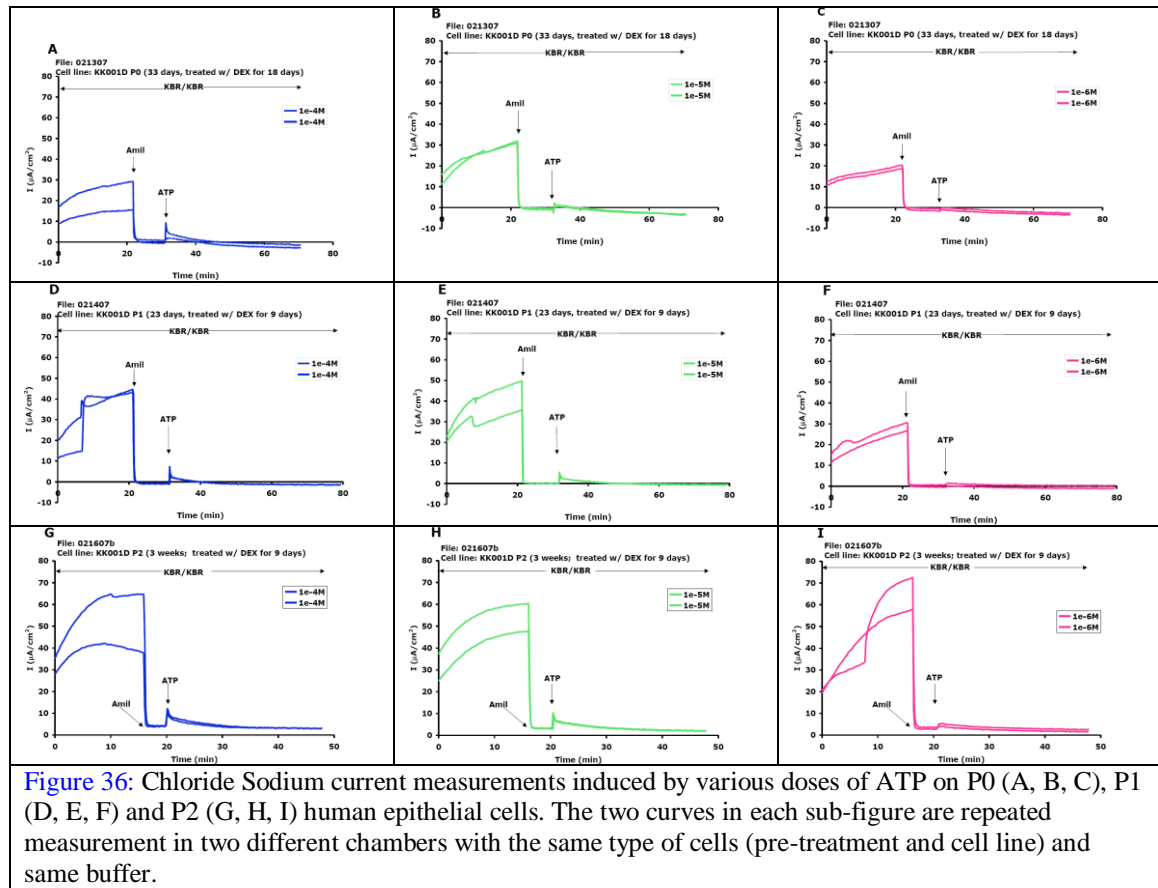


Figure 35: Sodium current measurements induced by various doses of ATP on P0 (A, B, C), P1 (D, E, F) and P2 (G, H, I) human epithelial cells. In each figure, the measurements in lighter color were done in bilateral chloride-free KBR solution. Those in darker color were done in bilateral chloride-free KBR solution with 5mM barium in apical side.

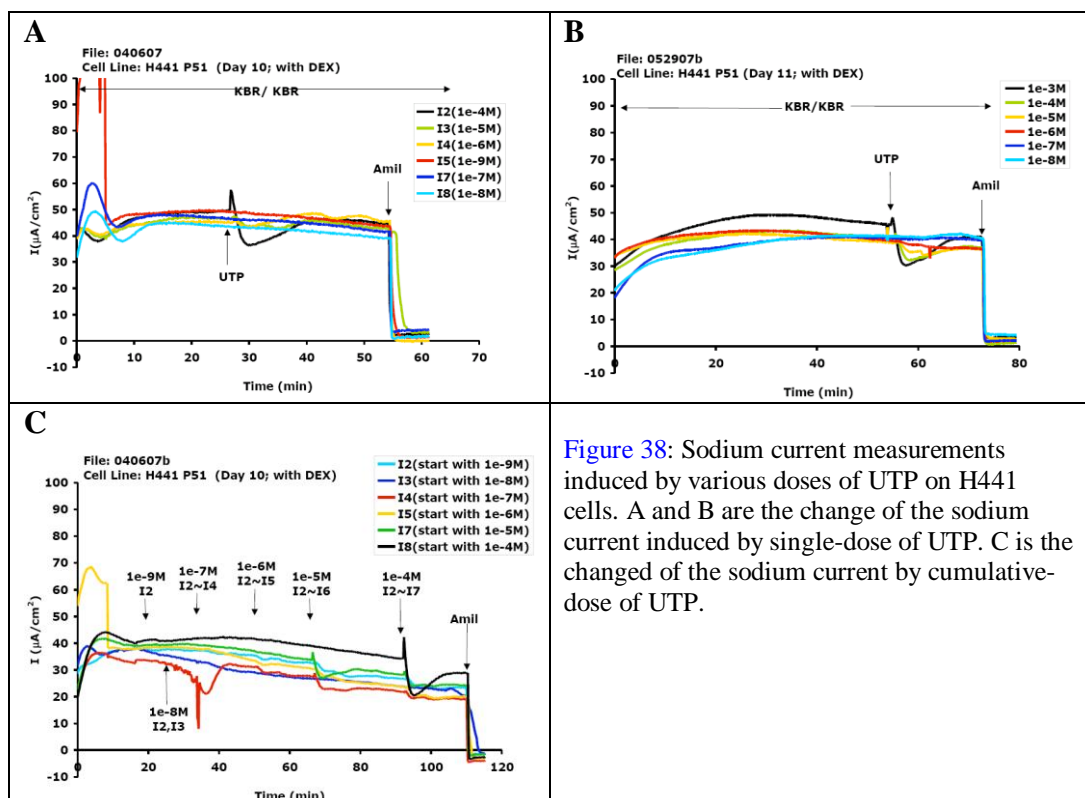
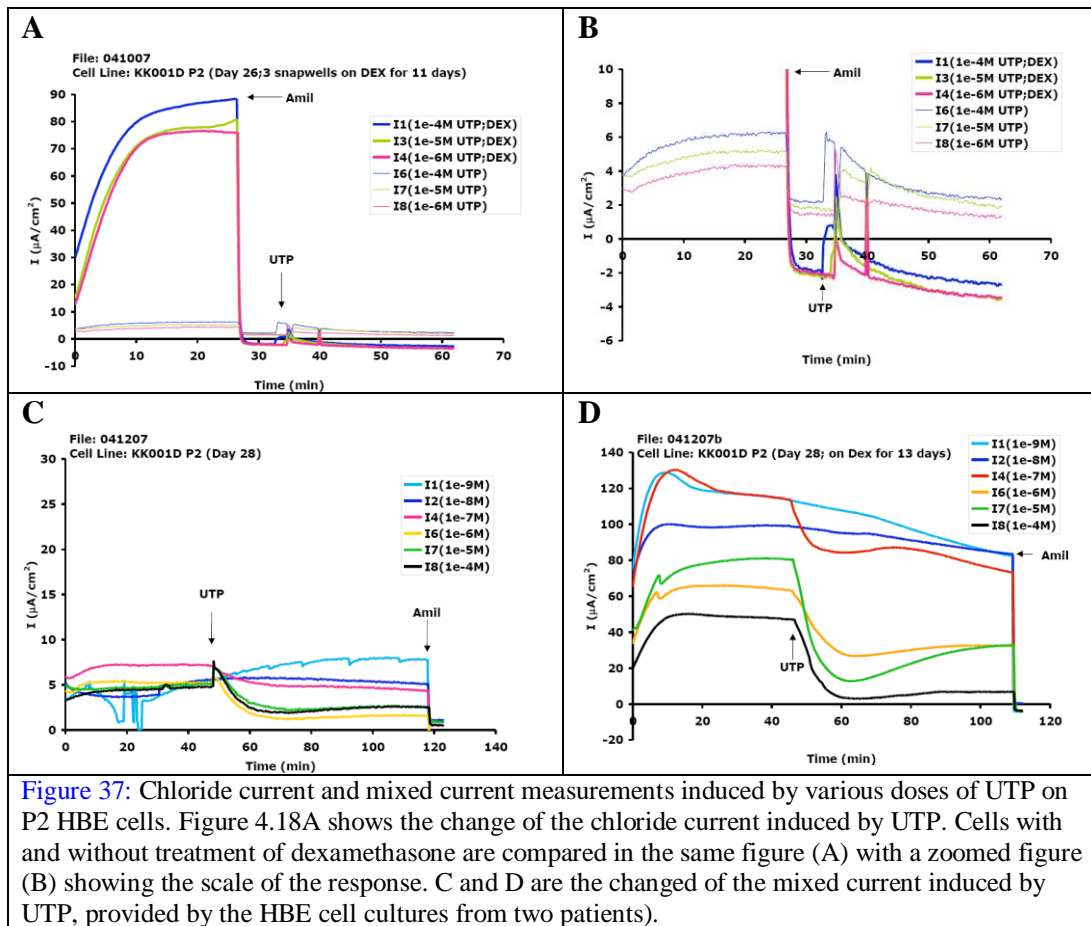
Notice these results are based on cells from a single cell line. To make the conclusion whether cell type really makes a difference in sodium current measurements,

experiments need to be done on different cell lines. The observation that P2 cells are more sensitive in both chloride and sodium current measurements may still hold.



4.4 EXPERIMENTAL RESULTS WITH UTP

UTP have similar effects on airway surface liquid regulation by activating the apical membrane receptors and regulating the transmembrane ionic flows. We replaced ATP with UTP and UDP and followed the same experimental protocol as before to study their regulation characteristics. We've tried these two drugs on two types of cell cultures, the bronchial human epithelial (HBE) cells and a type of cancer cells H441 [101]. H441 cell has similar bioelectric properties of HBE cells except it lacks of chloride channels in the apical membrane. Therefore it could be used to measure the sodium response to the two drugs without having to using Cl-free KBR solution. We also did some control test by



treating both types of cells with Dexamethasone and compare the measurements with those without the treatment.

In comparison with the regulation of ATP on ENaC in HBE cells from CF lungs, UTP induced the sodium channel regulation in H441 cells are somehow different. First, the peak of the response is much smaller ([Figure 38A and B](#)). Meanwhile, the relaxation time of the current, i.e., the time to reach a new steady state is about 20 ~30 minutes. Compared to the time of ATP response (~60 minutes), it is much shorter. The measurements from the cumulative –dose experiments showed a desensitization of signaling pathway to UTP ([Figure 38C](#)).

The response of the chloride channel CaCC and the response of both CaCC and ENaC channels to single dose of UTP ([Figure 37](#)) has similar curvature as that of ATP in the HBE cells. Dexamethasone seems to significantly increase the baseline current, as seen before. Because we currently have measurements from cell cultures of one patient, it is hard to study the amplitude of the response.

4.5 MODELING THE RESPONSE

We've studied the individual response of ENaC and CaCC channels to various doses of apical ATP through electrophysiological experiments. Differences in the dynamics of the responses, such as the time scale, the response amplitude, and the relaxation behavior, were identified. The average level of the induced change in the short-circuit current through CaCC, i.e. the height of the peak in the current relative to the baseline, is proportional to the dose of ATP. This is also true for the ENaC response. Meanwhile, we also saw a decreasing trend in the minimum value of I_{Na} as we increase ATP level. This study is essential for CF because it not only provides a fundamental evidence for the

response of HBE cells to ATP, but also insights into the design of novel therapeutic drugs given the different response of the two channels. As a matter of fact, aerosol nucleotide delivery and the use of amiloride in the airway surface of CF lungs, separately or in combination, have become two typical ways to treat CF. The former affects current through CaCC while the latter ENaC. Due to the difficulty in getting specimens of human bronchial epithelial (HBE) cells from CF patients and the time involved in culturing them, we are not able to collect enough samples to decrease the error bars in these figures. Therefore the study remains qualitative.

As mentioned earlier, the ion water transport model proposed by Novotny *et al.* added volume regulation to the permeability of the apical membrane Cl^- channel and to the maximum flux of the basolateral membrane cotransporter. As the mechanism for the channels and transporters to detect apical and cell volumes remains unclear in this model, a linear coupling was assumed for the volume with prescribed upper and lower bounds on the permeability and maximum flux. In our integrated model, we are going to assume a more realistic nonlinear coupling that does not require the specification of artificial upper and lower bounds. We want to begin by simulating the airway epithelium in normal lungs. Experimental observations suggest that the two apical ion permeabilities and the airway nucleotide and nucleoside concentrations normally follow the dose-response type of relationship. These curves can be mathematically modeled by writing the permeability of apical membrane to chloride and sodium ions, i.e. $P_{\text{Cl},a}$ and $P_{\text{Na},a}$, as nonlinear sigmoid functions of these two metabolites as shown in Eq.(4.2) and Eq.(4.3). The extra term $a_{\text{Na},0}$ and the minus sign in front of nonlinear term in Eq.(4.3) indicate the opposite effect of nucleotide and nucleoside have on the ENaC channel compared to that on CaCC.

$$P_{Cl,a}(C_{ATP}(t), C_{ADO}(t)) = \frac{a_{Cl,1}}{a_{Cl,2} + a_{Cl,3}e^{C_{ATP,ss}-C_{ATP}(t)}} + \frac{a_{Cl,4}}{a_{Cl,5} + a_{Cl,6}e^{C_{ADO,ss}-C_{ADO}(t)}} \quad (4.2)$$

$$P_{Na,a}(C_{ATP}(t), C_{ADO}(t)) = a_{Na,0} - \frac{a_{Na,1}}{a_{Na,2} + a_{Na,3}e^{C_{ATP,ss}-C_{ATP}(t)}} - \frac{a_{Na,4}}{a_{Na,5} + a_{Na,6}e^{C_{ADO,ss}-C_{ADO}(t)}} \quad (4.3)$$

These two equations serve as a connection for integrating the ATP regulation model and ion/water transport models. For the resting state, the level of nucleotides and nucleosides in the airway is not enough to activate the signaling pathway. However, when a big amount of ATP or adenosine is added to the airway, it starts the signaling process and changes the permeabilities of the two apical channels and leads to the change of the ions and water flows. Later this process will be terminated by the decrease in the concentrations of ATP and adenosine, caused by the catalysis of the enzymes on the membrane surface and dilution from water influx to the airway.

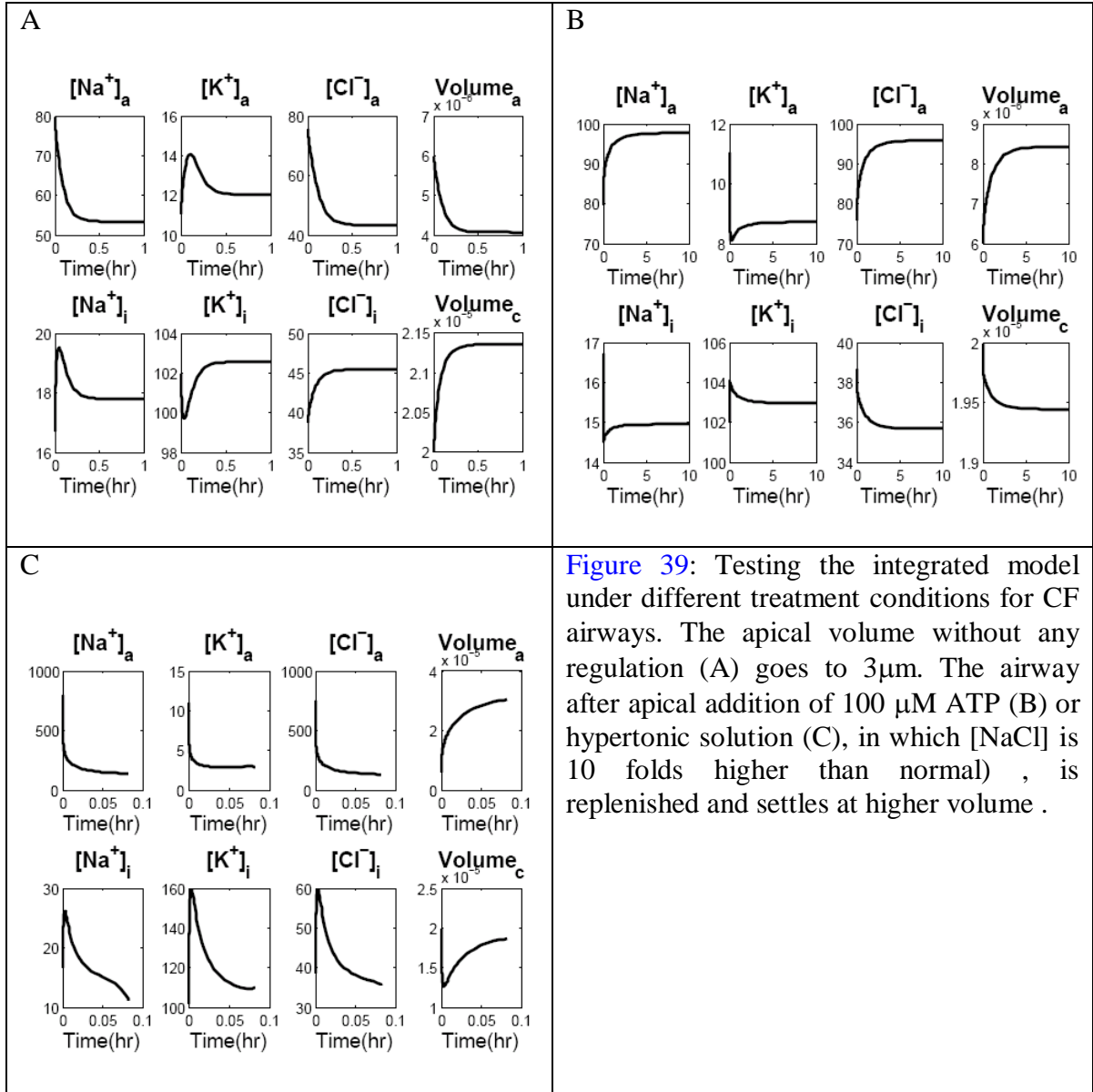
The baseline conditions for membrane permeability to chloride and sodium ions are different in normal and CF lungs and leads to different dose response relationship, and therefore different choices of parameter values in Eq.(4.2) and Eq.(4.3) in these two types of tissue culture. Based on the setup of the integrated model, we came up with different ways to test it systematically as shown in [Table 12](#). Basically the different scenarios have been labeled with various signal numbers. When a certain scenario is chosen, say adding 100 μ M ATP to the airway epithelium of a CF lung, the integrated system will automatically input 100 μ M to ATP regulation model as initial condition, choose permeability values that belongs to CF lungs for the ion/water transport model, and select the right dose-response relationship for CF epithelium to ATP and adenosine.

Although we currently do not have enough information to find out the dose response relationship in Eq(4.2) and Eq (4.3), we built a “toy” model, which combines

the ATP regulation model and ion/water transport model. Two “pseudo” dose response functions were also used to connect the two models in the whole system. The amounts of ATP and adeonsine in the ASL were set to be the same as *in vivo* conditions. We then changed the permeabilities from normal lungs to CF lungs [105] and tested the model under the conditions of aerosol ATP and hypertonic saline solution treatments. In agreement with the *in vivo* condition of CF epithelium which has an over-expressed apical sodium channel and no CFTR Cl channel, the apical membrane permeability to sodium ion, $P_{Na,a}$, was set to be 6.2×10^{-8} m/s and Its permeability to chloride, $P_{Cl,a}$ was decreased to 0. When these changes were made to the parameter set in the model, we ran it from steady state and tried to study the outcome of the model. For the condition that no treatment is conducted to the CF airways, we observed a much lower resting level for ASL ($4 \mu\text{m}$). And in both simulations for aerosol ATP treatment (Fig39B) and hypertonic challenge (Fig39C), the ASL increases due to the regulated CFTR and ENaC and settles at levels that are much higher than $7 \mu\text{m}$. All these simulation results agree with experimental observation under these conditions, which suggests that our integrated model is able to capture the key features of ASL regulation and provide its potential for the drug study to treat CF.

Lung Type	Features	Scenarios	Ion channels	Initial Ion composition
CF Lung	CFTR doesn't function. P2Y ₂ -R-activated pathway regulations through apical CaCC and ENaC	Aerosol ATP	CFTR: off CaCC: on ENaC: on	Steady state
		Hypertonic saline	CFTR: off CaCC: off ENaC: on	Increased
		Amiloride	CFTR: off CaCC: off ENaC: off	Steady state

Table 12: Different scenarios for testing the integrated model in CF lungs.



4.6 CONCLUSION

ASL regulation is a very complicated system. There are still unsolved questions in understanding how it works in CF and normal lungs. To study this system, we compartmentally divided it into two components, the ATP regulation in the airway and the ion/water flux across the epithelial membrane. We then built each component based on the current information we collected from literature and *in vivo* and *in vitro* experiments at CF center at UNC. Due to the lack of information on the dose response relationship between ATP/UTP and ion current or ion permeabilities, it is hard to use real

experimental data to test the integrated model that combines the ATP regulation and the ion/water flux modules. However, the *in vitro* experimental results shown in this chapter have provided useful information on dose response relationship. The key characteristics of dose response from early stage experimental observations, i.e., both the dynamics and relaxation time scale of the ionic current, made it possible for choosing mathematical functions to model the curvature of dose response relationship. Although the detailed information on the coefficients in these functions is yet to be decided as of now, we temporarily chose coefficients that could keep the dose response curves in a biologically reasonable range and integrate the two models in the previous chapters.

The model was not only able to simulate the lower height of ASL when no regulation of drug was involved ([Fig39A](#)). More importantly, it also showed a positive regulation on the ASL with ATP treatment ([Fig39B](#)) and hypertonic challenge ([Fig39C](#)). It is the first model that includes so many characteristics of ASL. Now that we have tested it under the three most important conditions and have observed the agreement with experimental data, we are very confident that this model could contribute tremendously to understanding CF and to the drug study of CF. After enough information is collected to accurately define the dose response between the drug and ionic currents, we could have a even finer tuned integrated model. In the future, we could also study the spacious drug effect by adding diffusion into this model and even include the hydrodynamics of ASL to simulate more realistic conditions of the lungs.

Appendix I:

OPERATOR-SPLITTING METHOD

Operator-Splitting method is a common way to numerically solve reaction/convection diffusion equations, where reaction/convective and diffusive forces are accounted for in separate substeps. The operator splitting method, also called time splitting or the method of fractional steps is widely used in solving initial value partial differential equations, which involves more than one operator on the right-hand side of the equation.

Suppose we have an initial valued equation of the form

$$\frac{\partial \mathbf{u}}{\partial t} = L\mathbf{u} \quad (4)$$

Where L is some operator. While L is not necessarily linear, suppose that it can at least be written as a linear sum of pieces, which acts additively on,

$$L\mathbf{u} = L_1\mathbf{u} + L_2\mathbf{u} + \dots + L_m\mathbf{u} \quad (5)$$

In the reaction diffusion equations, we normally have two operators, the reaction term and the diffusion term. So we will start with case $m = 2$, i.e. $L = L_1 + L_2$. By writing the operators in the form of, our equation looks like a standard growth equation

$$\frac{\partial X}{\partial t} = AX \quad (6)$$

with solution $X(t) = X(0) \exp(tA)$. Although we do not have a simple multiplier, the same principle applies. Namely, our exact solution is $\mathbf{u}(t) = \mathbf{u}(0) \exp(tL)$. By Taylor expansion, $\exp(tL)$ can be written as follows

$$\exp(tL) = 1 + tL + \frac{t^2}{2!}L^2 + \frac{t^3}{3!}L^3 + \dots \quad (7)$$

Therefore the change over 1 time step is

$$\begin{aligned}
\mathbf{u}(t + \Delta t) &= \exp((t + \Delta t)L)\mathbf{u}(0) \\
&= \exp(\Delta t L)\exp(tL)\mathbf{u}(0) \\
&= \exp(\Delta t L)\mathbf{u}(t)
\end{aligned} \tag{8}$$

Suppose that for L , we already know a difference operator scheme for updating the variable from time step n to time step $n + 1$, which can be written symbolically as

$$\mathbf{u}^{n+1} = F(\Delta t)\mathbf{u}^n \tag{9}$$

Comparing and , $F(\Delta t)$ can be thought as a numerical approximation of $\exp(\Delta t L)$. In the case of two operators, we could write the scheme as follows with only the first two terms in the Taylor expansion of each operator.

$$u^* = (I + \Delta t L_1)u^n \tag{10}$$

$$u^n = (I + \Delta t L_2)u^* \tag{11}$$

$F(\Delta t)$ in this case is combination of the two with overall first error accuracy.

$$\begin{aligned}
F(\Delta t) &= (I + \Delta t L_2)(I + \Delta t L_1) \\
&= I + \Delta t L_1 + \Delta t L_2 + \Delta t^2 L_2 L_1 \\
&= I + \Delta t L + \Delta t^2 L_2 L_1 \\
&= \exp(\Delta t L) + O(\Delta t^2)
\end{aligned} \tag{12}$$

Notice that the order we put the two sets of terms from Taylor expansion should follow the sequence we apply the operator on.

Suppose we have second-order schemes for L_1 and L_2 .

$$F_1(\Delta t) = I + \Delta t L_1 + \frac{\Delta t^2}{2!} L_1^2 + O(\Delta t^3) \tag{13}$$

$$F_2(\Delta t) = I + \Delta t L_2 + \frac{\Delta t^2}{2!} L_2^2 + O(\Delta t^3) \tag{14}$$

Sequential application would give

$$F_2(\Delta t)F_1(\Delta t) = I + \Delta t(L_1 + L_2) + \frac{\Delta t^2}{2!}(L_2^2 + 2L_2L_1 + L_1^2) + O(\Delta t^3) \tag{15}$$

The above seems like a second order scheme. Yet we still need to be careful to make the judgment. Since the order of applying the operators is important, if we compare with , the Taylor expansion of the exact operator $L = L_1 + L_2$, we can see some difference.

$$\begin{aligned}\exp(\Delta t L) &= \exp(\Delta t (L_1 + L_2)) \\ &= I + \Delta t (L_1 + L_2) + \frac{\Delta t^2}{2!} (L_1^2 + L_1 L_2 + L_2 L_1 + L_2^2) + O(\Delta t^3)\end{aligned}\quad (16)$$

So the scheme is not second order unless $L_1 L_2 = L_2 L_1$. If this is satisfied, it is said that L_1 and L_2 "commute".

As we can see from the derivation above, whether the two operators are commutable is a prerequisite to achieve the second order accuracy. As this condition may not be satisfied by every problem you work on, people were thinking of other schemes so that both operator splitting and high accuracy can be achieved. That's why Strang splitting method came up in 1968.

The basic idea of Strang splitting is like this. Suppose the reaction term L_1 and diffusion term L_2 in the system happen at different time scales. For example, reaction is a faster process than diffusion. Then operator term L_1 can be further split as $L_1/2 + L_1/2$.

Therefore the difference operator $F(\Delta t)$ is as follows,

$$F(\Delta t) = F_1(\Delta t/2) F_2(\Delta t) F_1(\Delta t/2) \quad (17)$$

which means that we should take half-step with L_1 , full step with L_2 and then half step with L_1 . To verify this is a second order scheme, we can just multiply the two difference operators together assuming and do not commute.

$$\begin{aligned}F(\Delta t) &= F_1(\Delta t/2) F_2(\Delta t) F_1(\Delta t/2) \\ &= \left(I + (\Delta t/2) L_1 + (\Delta t/2)^2 L_1^2 / 2! + O(\Delta t^3) \right) \\ &\quad \cdot \left(I + \Delta t L_2 + \Delta t^2 L_2^2 / 2! + O(\Delta t^3) \right) \\ &\quad \cdot \left(I + (\Delta t/2) L_1 + (\Delta t/2)^2 L_1^2 / 2! + O(\Delta t^3) \right) \\ &= I + \Delta t (L_1 + L_2) + \Delta t^2 (L_1^2 + L_1 L_2 + L_2 L_1 + L_2^2) / 2! + O(\Delta t^3)\end{aligned}\quad (18)$$

Comparing to (16), we can see that no matter L_1 and L_2 commute or not, the overall accuracy is the second order.

Having said all above, we now consider the second order schemes to solve each operator in the reaction diffusion equation. The reaction term, along with time derivative on the left-hand side, forms an ordinary differential equation.

$$\frac{\partial \mathbf{u}}{\partial t} = R(\mathbf{u}(\mathbf{x}, t), t) \quad (19)$$

In this ODE, \mathbf{u} and \mathbf{x} are both vectors. \mathbf{u} denotes the characters for different species in the system, say number of molecules or concentration, while \mathbf{x} is the domain where the system is in. We can use any of our favorite second-order numerical schemes to solve it, for example Runge-Kutta 2.

$$\begin{aligned} k_1 &= \Delta t R(\mathbf{u}_n, t_n) \\ k_2 &= \Delta t R(\mathbf{u}_n + k_1/2, t_n + \Delta t/2) \\ \mathbf{u}_{n+1} &= \mathbf{u}_n + k_2 + O(\Delta t^3) \end{aligned} \quad (20)$$

where $\mathbf{u}_n = \mathbf{u}(\mathbf{x}_n; t_n)$.

As for the diffusion term,

$$\frac{\partial \mathbf{u}}{\partial t} = \frac{\partial}{\partial \mathbf{x}} \left(\mathbf{D} \frac{\partial \mathbf{u}}{\partial \mathbf{x}} \right) \quad (21)$$

to put it in a simple way, we make such assumptions : (1) The diffusion process is in one dimension along the z axis; (2) All the species in the system diffuse at the same rate; (3) The medium along the x and y axes are homogeneous, i.e., the diffusion coefficient for the i^{th} species D_i is a constant. Then the diffusion equation for the i^{th} species can be written as

$$\frac{\partial u_i}{\partial t} = D_i \frac{\partial^2 u_i}{\partial z^2} \quad (22)$$

In the following, we will drop the subscription i for the purpose of convenience. The above forms a parabolic equation and the typical way of solving it is the finite difference method shown in (18). However there is another scheme called "Crank Nicolson scheme" which has same accuracy order but is stable no matter what Δt and Δz you choose.

$$u_j^{n+1} = u_j^n + \frac{D\Delta t}{\Delta z^2} (u_{j+1}^n - 2u_j^n + u_{j-1}^n) \quad (23)$$

Developed by John Crank and Phyllis Nicolson in the mid 20th century, the Crank-Nicolson method is a finite difference method used for numerically solving the heat and related equations.

$$u_j^{n+1} = u_j^n + \alpha \left[(u_{j+1}^{n+1} - 2u_j^{n+1} + u_{j-1}^{n+1}) + (u_{j+1}^n - 2u_j^n + u_{j-1}^n) \right] \quad (24)$$

where $\alpha = D\Delta t / (2\Delta z^2)$. To say the same thing with equations, move all the $n + 1$ terms in to the left and the $n+1$ terms to the right, obtaining

$$-\alpha u_{j+1}^{n+1} + (1 + 2\alpha)u_j^{n+1} - \alpha u_{j-1}^{n+1} = \alpha u_{j+1}^n + (1 - 2\alpha)u_j^n + \alpha u_{j-1}^n \quad (25)$$

Now think of the left side of equation as containing all the unknown quantities and the right side as containing all known quantities. We can rewrite equation as a set of simultaneous equations.

$$\begin{bmatrix} A_{bottom} & -\alpha & 0 & & & \\ -\alpha & 1+2\alpha & -\alpha & 0 & & \\ 0 & -\alpha & 1+2\alpha & -\alpha & 0 & \\ & 0 & 0 & 0 & 0 & 0 \\ & & 0 & -\alpha & 1+2\alpha & -\alpha \\ & & & 0 & -\alpha & A_{top} \end{bmatrix} \begin{bmatrix} u_1^{n+1} \\ u_2^{n+1} \\ u_3^{n+1} \\ \vdots \\ u_{m-1}^{n+1} \\ u_m^{n+1} \end{bmatrix} = \begin{bmatrix} B_{bottom} \\ \alpha u_1^n + (1-2\alpha)u_2^n + \alpha u_3^n \\ \alpha u_2^n + (1-2\alpha)u_3^n + \alpha u_4^n \\ \vdots \\ \alpha u_{m-2}^n + (1-2\alpha)u_{m-1}^n + \alpha u_m^n \\ B_{top} \end{bmatrix} \quad (26)$$

where b_{left} and b_{right} are adjustable and have to do with the boundary conditions on the bottom and top of the domain the reaction and diffusion happen. For ADP and AMP that are not released or uptake at epithelial membrane, they have no-flux boundary condition.

This means in Eq ((26))

$$u_{j-1}^{n+1} = u_j^{n+1} \quad (27)$$

$$u_{j-1}^n = u_j^n \quad (28)$$

and therefore we have

$$\begin{bmatrix} 1+\alpha & -\alpha & 0 & & & \\ -\alpha & 1+2\alpha & -\alpha & 0 & & \\ 0 & -\alpha & 1+2\alpha & -\alpha & 0 & \\ & 0 & 0 & 0 & 0 & 0 \\ & & 0 & -\alpha & 1+2\alpha & -\alpha \\ & & & 0 & -\alpha & 1+\alpha \end{bmatrix} \begin{bmatrix} u_1^{n+1} \\ u_2^{n+1} \\ u_3^{n+1} \\ \vdots \\ u_{m-1}^{n+1} \\ u_m^{n+1} \end{bmatrix} = \begin{bmatrix} (1-\alpha)u_1^n + \alpha u_2^n \\ \alpha u_1^n + (1-2\alpha)u_2^n + \alpha u_3^n \\ \alpha u_2^n + (1-2\alpha)u_3^n + \alpha u_4^n \\ \vdots \\ \alpha u_{m-2}^n + (1-2\alpha)u_{m-1}^n + \alpha u_m^n \\ \alpha u_{m-1}^n + (1-\alpha)u_m^n \end{bmatrix} \quad (29)$$

For the case of ATP, because it follows a constant release rate from epithelial cells, it has its release form shown in the boundary condition at $z=0$ as follows

$$J_{ATP} = -D \frac{\partial u}{\partial z} \Big|_{z=0} \quad (30)$$

$$u_0 = u_1 + \frac{J_{ATP} \Delta z}{D} \quad (31)$$

If we write it in a discrete fashion, this equation becomes Eq.(32), and it holds for all the time steps. Again, the boundary condition at the fluid surface still remains to be "no-flux".

This way, the matrix operation become

$$\begin{bmatrix} 1+\alpha & -\alpha & 0 & & & \\ -\alpha & 1+2\alpha & -\alpha & 0 & & \\ 0 & -\alpha & 1+2\alpha & -\alpha & 0 & \\ & 0 & 0 & 0 & 0 & 0 \\ & & 0 & -\alpha & 1+2\alpha & -\alpha \\ & & & 0 & -\alpha & 1+\alpha \end{bmatrix} \begin{bmatrix} u_1^{n+1} \\ u_2^{n+1} \\ u_3^{n+1} \\ \vdots \\ u_{m-1}^{n+1} \\ u_m^{n+1} \end{bmatrix} = \begin{bmatrix} (1-\alpha)u_1^n + \alpha u_2^n \\ \alpha u_1^n + (1-2\alpha)u_2^n + \alpha u_3^n \\ \alpha u_2^n + (1-2\alpha)u_3^n + \alpha u_4^n \\ \vdots \\ \alpha u_{m-2}^n + (1-2\alpha)u_{m-1}^n + \alpha u_m^n \\ \alpha u_{m-1}^n + (1-\alpha)u_m^n \end{bmatrix} \quad (32)$$

The matrices for solving concentrations of adenosine and inosine are a little trickier to derive because the uptake of these two nucleosides follows nonlinear Michaelis Menten Kinetics shown in Eq.(33). We need to linearize it under a certain conditions in order to construct the first row of matrix A.

$$J_{uptake} = -D \frac{\partial u}{\partial z} \Big|_{z=0} = -\frac{V_{\max} u}{K_M + u} \quad (33)$$

$$u_0 = \frac{(u_1 - K_M - V_{\max} \Delta z / D) \pm \sqrt{(K_M + V_{\max} \Delta z / D - u_1)^2 + 4 K_M}}{2} \quad (34)$$

The experiment we are simulating starts initially with 100 uM of ATP while zero other species in the system. As we could observe from the experimental measurements, time dependent concentration of inosine within the first 60 minutes ranges from 0 to less than 20 uM while that of adenosine from 0 to 80 uM. Both of them have similar uptake rates ($V_{\max}=0.45$ uM/min, $K_M=17$ uM). The comparison of K_M and adenosine and inosine levels indicates that it's not justifiable to linearize the Michaelis Menten term. Instead, the two grid points around the boundary should follow a relationship that holds for all time steps shown in Eq(??). However, if we study the dynamics of the system around steady state in which adenosine are at very down stream of micromolar scale ($[ADO]_{ss}=0.168$ uM, $[INO]_{ss}$ was not measured), Eq.(33) could be linearized as

$$J_{uptake} = -D \frac{\partial u}{\partial z} \Big|_{z=0} = -\frac{V_{\max} u}{K_M + u} : -\frac{V_{\max}}{K_M} u \quad (35)$$

and

$$u_0 = \left(\frac{V_{\max} \Delta z}{K_M + D} + 1 \right)^{-1} u_1 \quad (36)$$

and the matrix operation could be rewritten as

$$\begin{bmatrix} 1+2\alpha-\alpha\beta & -\alpha & 0 & & & \\ -\alpha & 1+2\alpha & -\alpha & 0 & & \\ 0 & -\alpha & 1+2\alpha & -\alpha & 0 & \\ & 0 & 0 & 0 & 0 & 0 \\ & & 0 & -\alpha & 1+2\alpha & -\alpha \\ & & & 0 & -\alpha & 1+\alpha \end{bmatrix} \begin{bmatrix} u_1^{n+1} \\ u_2^{n+1} \\ u_3^{n+1} \\ \vdots \\ u_{m-1}^{n+1} \\ u_m^{n+1} \end{bmatrix} = \begin{bmatrix} (1-2\alpha+\alpha\beta)u_1^n + \alpha u_2^n \\ \alpha u_1^n + (1-2\alpha)u_2^n + \alpha u_3^n \\ \alpha u_2^n + (1-2\alpha)u_3^n + \alpha u_4^n \\ \vdots \\ \alpha u_{m-2}^n + (1-2\alpha)u_{m-1}^n + \alpha u_m^n \\ \alpha u_{m-1}^n + (1-\alpha)u_m^n \end{bmatrix} \quad (37)$$

where $\beta = \left(\frac{V_{\max} \Delta z}{K_M D} + 1 \right)^{-1}$.

As we can see from the above derivation, the problem has been converted to iteratively solving $A \cdot \mathbf{u}^{n+1} = B(\mathbf{u}^n)$ and the matrix equation gives them implicitly by the solution of simultaneous equations. The important thing to notice is that the matrix is tridiagonal, that is, except for three central diagonals all the elements of the matrix are zero. The solution to such a set of simultaneous equations may be economically obtained. In fact, this implicit method turns out to be cheaper in cost in comparison with a lot explicit method, since the increased accuracy allows the use of a much larger numerical choice of Δt .

Since the Crank-Nicolson method involves taking the derivative half way between the beginning and the end of the time space, it is hence an average between a fully implicit and fully explicit model of PDE's. This is where the second-order convergence comes from, because essentially the first-order error term drops out from the averaging. Suppose solution at t_n , i.e. $\mathbf{u}(\mathbf{x}, n\Delta t)$ is available, the following is a flow of chart for the solving procedure applying the Splitting Method.

Step 1: Solve $\frac{\partial \mathbf{u}}{\partial t} = R(\mathbf{u}(\mathbf{x}, t), t)$ in $t \in [n\Delta t, (n+1/2)\Delta t]$ inside the domain Ω using

Crank Nicolson scheme. The solution we get from this step is $\mathbf{u}^*(\mathbf{x}, t_{n+1/2})$;

Step 2: Use $\mathbf{u}^*(\mathbf{x}, t_{n+1/2})$ as initial condition for $\frac{\partial \mathbf{u}}{\partial t} = D \frac{\partial^2 \mathbf{u}}{\partial \mathbf{x}^2}$ and solve it in

$t \in [n\Delta t, (n+1)\Delta t]$ inside Ω using Runge-Kutta 2. The solution we get from this step is

$\mathbf{u}^{**}(\mathbf{x}, t_{n+1/2})$;

Step 3: Solve $\frac{\partial \mathbf{u}}{\partial t} = R(\mathbf{u}(\mathbf{x}, t), t)$ again with initial condition $\mathbf{u}^{**}(\mathbf{x}, t_{n+1/2})$ in

$t \in [(n+1/2)\Delta t, n\Delta t]$ in Ω using Crank Nicolson scheme. The solution is $\mathbf{u}(\mathbf{x}, t_{n+1})$;

Step 4: Go back to Step 1 and work on the $t \in [(n+1)\Delta t, (n+3/2)\Delta t]$.

Although Operator-Splitting method has a second order of accuracy, it also has its drawbacks when it comes to a problem with discontinuous initial condition or the reaction term is not continuous in the space we are solving. The noise around discontinuity gets larger with time and eventually grows out of bound. To minimize the noise, we have to start with a really small delta t or big delta x. Small time step results in a fairly big matrix and time-consuming matrix operation. Big space step leads to rough lattice and less information about distribution of nucleotide and nucleoside concentrations in the space. However, the diffusion model doesn't favor a rough lattice. If we consider a 20 μ m height for ASL and the enzyme layer is only a couple of microns, the size of grid couldn't exceed 1 micron. This results in a heavy and slow computation. Here we didn't use the Due to the problem with the linearization of the boundary condition for adenosine and inosine and intensity of computation, we only studied dynamics of ATP, ADP and AMP using this method.

Appendix II:

Model Equations

Part I: Fluxes across membranes in each of the 3 compartments

1. Apical \leftrightarrow intracellular (passive fluxes)

$$J_{Pass,Na,a \rightarrow c} = \frac{-P_{Na,a} Z_{Na} F V_{m,a}}{RT} \left(\frac{[Na^+]_a - [Na^+]_c \exp\left(\frac{Z_{Na} F V_{m,a}}{RT}\right)}{1 - \exp\left(\frac{Z_{Na} F V_{m,a}}{RT}\right)} \right)$$

$$J_{Pass,K,a \rightarrow c} = \frac{-P_{K,a} Z_K F V_{m,a}}{RT} \left(\frac{[K^+]_a - [K^+]_c \exp\left(\frac{Z_K F V_{m,a}}{RT}\right)}{1 - \exp\left(\frac{Z_K F V_{m,a}}{RT}\right)} \right)$$

$$J_{Pass,Cl,a \rightarrow c} = \frac{-P_{Cl,a} Z_{Cl} F V_{m,a}}{RT} \left(\frac{[Cl^-]_a - [Cl^-]_c \exp\left(\frac{Z_{Cl} F V_{m,a}}{RT}\right)}{1 - \exp\left(\frac{Z_{Cl} F V_{m,a}}{RT}\right)} \right)$$

2. Intracellular \leftrightarrow basolateral region (passive, Na-K pump and Na-K-2Cl cotransport)

$$J_{Pass,K,b \rightarrow c} = \frac{-P_{K,b} Z_K F V_{m,b}}{RT} \left(\frac{[K^+]_b - [K^+]_c \exp\left(\frac{Z_K F V_{m,b}}{RT}\right)}{1 - \exp\left(\frac{Z_K F V_{m,b}}{RT}\right)} \right)$$

$$J_{Pass,Cl,b \rightarrow c} = \frac{-P_{Cl,b} Z_{Cl} F V_{m,b}}{RT} \left(\frac{[Cl^-]_b - [Cl^-]_c \exp\left(\frac{Z_{Cl} F V_{m,b}}{RT}\right)}{1 - \exp\left(\frac{Z_{Cl} F V_{m,b}}{RT}\right)} \right)$$

$$J_{pump,b \rightarrow c} = J_{pump,max} \left(\frac{[Na^+]_c}{[Na^+]_c + K_{pump,Na}} \right)^3 \left(\frac{[K^+]_b}{[K^+]_b + K_{pump,K}} \right)^2 (5 \times 10^{-3} V_{m,b} + 1.25)$$

$$J_{pump,Na,baso \rightarrow cell} = -3J_{pump,baso \rightarrow cell} \quad J_{pump,K,cell \rightarrow baso} = 2J_{pump,baso \rightarrow cell}$$

$$J_{\text{cot},b \rightarrow c} = J_{\text{cot},\text{max}} \left(\frac{[Na^+]_b}{[Na^+]_b + K_{\text{cot},Na}} \cdot \frac{[K^+]_b}{[K^+]_b + K_{\text{cot},K}} \cdot \frac{[Cl^-]_b}{[Cl^-]_b + K_{\text{cot},Cl,1}} \cdot \frac{[Cl^-]_b}{[Cl^-]_b + K_{\text{cot},Cl,2}} \right. \\ \left. - \frac{[Na^+]_c}{[Na^+]_c + K_{\text{cot},Na}} \cdot \frac{[K^+]_c}{[K^+]_c + K_{\text{cot},K}} \cdot \frac{[Cl^-]_c}{[Cl^-]_c + K_{\text{cot},Cl,1}} \cdot \frac{[Cl^-]_c}{[Cl^-]_c + K_{\text{cot},Cl,2}} \right)$$

3. Apical \leftrightarrow intracellular region (passive fluxes)

$$J_{\text{Pass},Na,a \rightarrow b} = \frac{-P_{Na,p} Z_{Na} F V_{m,p}}{RT} \left(\frac{[Na^+]_a - [Na^+]_b \exp\left(\frac{Z_{Na} F V_{m,p}}{RT}\right)}{1 - \exp\left(\frac{Z_{Na} F V_{m,p}}{RT}\right)} \right)$$

$$J_{\text{Pass},K,a \rightarrow b} = \frac{-P_{K,p} Z_K F V_{m,p}}{RT} \left(\frac{[K^+]_a - [K^+]_b \exp\left(\frac{Z_K F V_{m,p}}{RT}\right)}{1 - \exp\left(\frac{Z_K F V_{m,p}}{RT}\right)} \right)$$

$$J_{\text{Pass},Cl,a \rightarrow b} = \frac{-P_{Cl,p} Z_{Cl} F V_{m,p}}{RT} \left(\frac{[Cl^-]_a - [Cl^-]_b \exp\left(\frac{Z_{Cl} F V_{m,p}}{RT}\right)}{1 - \exp\left(\frac{Z_{Cl} F V_{m,p}}{RT}\right)} \right)$$

Part II: Equations for ions and volumes in different compartments

We assume that membranes are at equilibrium all the time. So membrane potentials ($V_{m,a}$, $V_{m,b}$ and $V_{m,p}$) are calculated in the beginning of each iteration by solving the nonlinear equation system using Newton Raphson method.

$$\begin{cases} I_P + I_A = 0 \\ I_P - I_B = 0 \end{cases}$$

Where

$$\begin{aligned} I_A(V_{m,a}) &= J_{\text{Pass},Na,a \rightarrow c} + J_{\text{Pass},K,a \rightarrow c} - J_{\text{Pass},Cl,a \rightarrow c} \\ I_B(V_{m,b}) &= J_{\text{Pass},K,a \rightarrow c} - J_{\text{Pass},Cl,a \rightarrow c} + J_{\text{pump},b \rightarrow c} \\ I_P(V_{m,p}) &= J_{\text{Pass},Na,a \rightarrow b} + J_{\text{Pass},K,a \rightarrow b} - J_{\text{Pass},Cl,a \rightarrow b} \\ V_{m,p} &= V_{m,a} + V_{m,b} \end{aligned}$$

Apical Region:

$$\begin{aligned}
\frac{d[Na^+]_a}{dt} &= \frac{1}{Vol_a} \left(-J_{pass,Na,a \rightarrow c} - J_{pass,Na,a \rightarrow b} - [Na^+]_a \frac{dVol_a}{dt} \right) \\
\frac{d[K^+]_a}{dt} &= \frac{1}{Vol_a} \left(-J_{pass,K,a \rightarrow b} - [K^+]_a \frac{dVol_a}{dt} \right) \\
\frac{d[Cl^-]_a}{dt} &= \frac{1}{Vol_a} \left(-J_{pass,Cl,a \rightarrow c} - J_{pass,Cl,a \rightarrow b} - [Cl^-]_a \frac{dVol_a}{dt} \right) \\
\frac{dVol_a}{dt} &= P_{H_2O,a} \left([Na^+]_a + [K^+]_a + [Cl^-]_a - [Na^+]_c + [K^+]_c + [Cl^-]_c - \frac{\# \text{ of anion}_c}{Vol_a} \right) \\
&\quad + P_{H_2O,p} \left([Na^+]_a + [K^+]_a + [Cl^-]_a - [Na^+]_b + [K^+]_b + [Cl^-]_b \right)
\end{aligned}$$

Intracellular Region:

$$\begin{aligned}
\frac{d[Na^+]_c}{dt} &= \frac{1}{Vol_c} \left(J_{pass,Na,a \rightarrow c} + J_{pass,Na,b \rightarrow c} + 3J_{pump,b \rightarrow c} + J_{cot,b \rightarrow c} - [Na^+]_c \frac{dVol_c}{dt} \right) \\
\frac{d[K^+]_c}{dt} &= \frac{1}{Vol_c} \left(J_{pass,K,b \rightarrow c} - 2J_{pump,b \rightarrow c} + J_{cot,b \rightarrow c} - [K^+]_c \frac{dVol_c}{dt} \right) \\
\frac{d[Cl^-]_c}{dt} &= \frac{1}{Vol_c} \left(J_{pass,Cl,a \rightarrow c} + J_{pass,Cl,b \rightarrow c} + 2J_{cot,b \rightarrow c} - [Cl^-]_c \frac{dVol_c}{dt} \right) \\
\frac{dVol_c}{dt} &= P_{H_2O,a} \left([Na^+]_c + [K^+]_c + [Cl^-]_c + \frac{\# \text{ of anion}_c}{Vol_a} - [Na^+]_a - [K^+]_a - [Cl^-]_a \right) \\
&\quad + P_{H_2O,b} \left([Na^+]_c + [K^+]_c + [Cl^-]_c + \frac{\# \text{ of anion}_c}{Vol_a} - [Na^+]_b - [K^+]_b - [Cl^-]_b \right)
\end{aligned}$$

Basolateral Region:

$$\frac{d[Na^+]_b}{dt} = 0 \quad \frac{d[K^+]_c}{dt} = 0 \quad \frac{d[Cl^-]_c}{dt} = 0 \quad \frac{dVol_c}{dt} = 0$$

Appendix III:

PROTOCOL OF MAKING BATHING SOLUTIONS

Krebs Bicarbonate Ringers (KBR) *

Compound	Stock Solution (1L)			Final Working Solution (1L)	
	Molarity	M.W.	g/L	Volume of stock	Molarity (mM)
K ₂ HPO ₄	48mM	174.18	8.36	50 ml	2.4
KH ₂ PO ₄	8.0mM	136.09	1.08	50 ml	0.4
NaCl	2.3M	58.44	134.42	50 ml	115
NaHCO ₃	500mM	84.01	42	50 ml	25
CaCl ₂ ·2H ₂ O	24mM	147.0	3.6	50 ml	1.2
MgCl ₂ ·6H ₂ O	24mM	203.30	4.88	50 ml	1.2

1. Combine K₂HPO₄, KH₂PO₄, NaCl, and NaHCO₃
2. Add distilled H₂O (700 ml)
3. Gas for 30 minutes with 5% CO₂ – 95% O₂
4. Add CaCl₂·2H₂O
5. Add MgCl₂·6H₂O
6. 0.92g D-glucose
7. Filter

Final Concentration (mM)	
Na	140
K	5.2
Ca	1.2
HCO ₃ ⁻	25
Cl	120
Mg	1.2
Glucose	5.2

* Keep solution well gassed and refrigerated to avoid precipitation. Warm before use.

Chloride free KBR*

Compound	Stock Solution (1L)			Final Working Solution (1L)	
	Molarity	M.W.	g/L	Volume of stock	Molarity (mM)
K ₂ HPO ₄	48mM	174.18	8.36	50 ml	2.4
KH ₂ PO ₄	8.0mM	136.09	1.08	50 ml	0.4
Gluconic Acid (Na Salt)	575 mM	218.13	125.42	200 ml	115
NaHCO ₃	500mM	84.01	42	50 ml	25
Gluconic Acid (Ca Salt)	24.5mM	215.2	5.34	50 ml	1.2
MgSO ₄ ·7H ₂ O	21.6mM	246.5	5.34	50 ml	1.08

1. Combine K₂HPO₄, KH₂PO₄, Na Gluconate, and NaHCO₃
2. Add distilled H₂O (600 ml)
3. Gas for 30 minutes with 5% CO₂ – 95% O₂
4. Add Ca Gluconate
5. Add MgSO₄·7H₂O
6. 0.92g D-glucose
7. Filter

Final Concentration (mM)	
Na	140
K	5.2
Ca	1.2
HCO ₃ ⁻	25
Gluconate	117.5
Mg	1.08
Glucose	5.2

* Keep solution well gassed and refrigerated to avoid precipitation. Warm before use.

Chloride free KBR with 5mM Ba²⁺ *

Compound	Stock Solution (1L)			Final Working Solution (1L)	
	Molarity	M.W.	g/L	Volume of stock	Molarity (mM)
K ₂ HPO ₄	48mM	174.18	8.36	50 ml	2.4
KH ₂ PO ₄	8.0mM	136.09	1.08	50 ml	0.4
Gluconic Acid (Na Salt)	575mM	218.13	125.42	200 ml	115
NaHCO ₃	500mM	84.01	42	50 ml	25
Gluconic Acid (Ca Salt)	24.5mM	215.2	5.34	50 ml	1.2
Gluconic Acid (Mg Salt)**	21.6mM	207.3	8.95	50 ml	1.08
BaCl ₂	5mM	244.27	1.22	No stock	5

1. Combine K₂HPO₄, KH₂PO₄, Na Gluconate, and NaHCO₃
2. Add dH₂O (600 ml)
3. Gas for 30 minutes with 5% CO₂ – 95% O₂
4. Add Ca Gluconate
5. Add Mg Gluconate
6. Add 0.92g D-glucose
7. Put the solution in measuring cylinder and add distilled H₂O to 1L
8. Add 1.22g BaCl₂ while keeping the solution well stirred
9. Filter

Final Concentration (mM)	
Na	140
K	5.2
Ca	1.2
HCO ₃ ⁻	25
Cl	10
Mg	1.08
Ba	5
Gluconate	119.7
Glucose	5.2

* Keep solution well gassed and refrigerated to avoid precipitation. Warm before use.

** Mg Gluconate : Since Ba²⁺ reacts with SO₄²⁻ and precipitates, SO₄²⁻ needs to be replaced by Gl⁻. Every Mg₂Gl molecule has **half** of Mg²⁺ and 1 Gl⁻.

REFERENCES

1. Kerem, B., Rommens, J. M., Buchanan, J. A., Markiewicz, D., Cox, T. K., Chakravarti, A., Buchwald, M. and Tsui, L.C. Identification of the Cystic Fibrosis Gene: Genetic Analysis. *Science* 245 (4922): 1073-80 (Sept. 8, 1989). PMID: 2570460
2. Riordan, J. R., Rommens, J. M., Kerem, B., Alon, N., Rozmahel, R., Grzelczak, Z., Zielenski, J., Lok, S., Plavsic, N., Chou, J. L., Drumm, M. L., Iannuzzi, M. C., Collins, F. S. and Tsui, L. C. Identification of the Cystic Fibrosis Gene: Cloning and Characterization of Complementary DNA. *Science* 245 (4922): 1066-73
3. Rommens, J. M., Iannuzzi, M. C., Kerem, B., Drumm, M. L., Melmer, G., Dean, M., Rozmahel, R., Cole, J. L., Kennedy, D., Hidaka, N., Zsiga, M., Buchwald, M., Riordan, J. R., Tsui, L. C. and Collins, F. S. "Identification of the Cystic Fibrosis Gene: Chromosome Walking and Jumping." *Science* 245 (4922): 1059-65
4. Boucher, R.C. Airway surface dehydration in cystic fibrosis: pathogenesis and therapy. *Annual Review of Medicine* Vol. 58: 157-170 (Volume publication date February 2007)
5. Boucher, R.C. Status of gene therapy for cystic fibrosis lung disease. *J Clin Invest*, February 1999, Volume 103, Number 4, 441-445
6. Boucher, R.C. New concepts of the pathogenesis of cystic fibrosis lung disease. *Eur Respir J* 2004; 23:146-158
7. Boucher, R.C. Molecular insights into the physiology of the 'thin film' of airway surface liquid. *J Physiol* 1999; 516:631-38.
8. Matsui, H., Randell, S.H., Peretti, S.W., Davis, W., Boucher, R.C. Coordinated clearance of periciliary liquid and mucus from airway surfaces. *J Clin Invest* 1998; 102:1125-1131.
9. Knowles, M., Gatzky, J., Boucher, R.C. Increased bioelectric potential difference across respiratory epithelia in cystic fibrosis. *N Engl J Med* 1981; 305:1489-1495.
10. Knowles, M., Gatzky, J., Boucher, R. C. Relative ion permeability of normal and cystic fibrosis nasal epithelium. *J Clin Invest*. 1983 May; 71(5): 1410-7.
11. Boucher, R. C., Cheng, E.H.C., Paradiso, A.M., Stutts, M.J., Knowles, M.R., Earp, H.S. Chloride secretory response of cystic fibrosis human airway epithelia: preservation of calcium but not protein kinase C- and A-dependent mechanism. *J. Clin. Invest*. 1989; 84:1424-1431.
12. Willumsen, N. J., Boucher, R. C. Activation of an apical Cl⁻ conductance by Ca²⁺ ionophores in cystic fibrosis airway epithelia. *Am. J. Physiol*. 1989; 256:C226-C233

13. Hartmann, T., Kondo, M., Mochizuki, H., Verkman, A.S., Widdicombe, J.H. Calcium-dependent regulation of Cl secretion in tracheal epithelium. *Am. J. Physiol.* 1992; 262:L163-L168
14. Boucher, R. C. Airway Surface Dehydration in Cystic Fibrosis: Pathogenesis and Therapy. *Annual Review of Medicine* (2007) 58(1), 157-170
15. Boucher, R. C. Evidence for airway surface dehydration as the initiating event in CF airway disease. *Journal of Internal Medicine* (2007); 261(1), 5-16
16. Davis, C. W. Regulation of mucin secretion from in vitro cellular models. (2002) *Norvatis Found Symp.* 248, 113-125
17. Williams, O. W., Sharafkhaneh, A., Kim, V., Dickey, B. F., and Evans, C. M. Airway Mucus: From Production to Secretion (2006) *Am. J. Respir. Cell Mol. Biol.* 34(5), 527-536
18. Donaldson, S. H., and Boucher, R. C. (1998) Therapeutic applications for nucleotides in lung diseases. In: Turner, J. T., Weisman, G. A., Fedan, J. S. (ed). *The P2 Nucleotide Receptors*, Humana Press, Totowa
19. Marcet, B., and Boeynaems J. M., Relationships between cystic fibrosis transmembrane conductance regulator, extracellular nucleotides and cystic fibrosis. *J.M. Pharmacology & Therapeutics* 112, 719-732
20. Lazarowski, E. R., Boucher, R. C., and Harden, T. K. Mechanisms of release of nucleotides and integration of their action as P2X- and P2Y-receptor activating molecules. *Mol Pharmacol* 64:785-795, 2003
21. Tarran, R., Button, B., and Boucher, R. C. Regulation of normal and cystic fibrosis airway surface liquid volume by phasic shear stress. *Annu. Rev. Physiol.* 68: 543-561. (2006) *Annual Review of Physiology* 68(1), 543-561
22. Kunzelmann, K., Scheidt, K., Scharf, B., Ousingsawat, J., Schreiber, R., Wainwright, B., and McMorran, B. Flagellin of *Pseudomonas aeruginosa* inhibits Na⁺ transport in airway epithelia. (2006) *FASEB J.*, 05-4454fje
23. Button, B., Picher, M., and Boucher, R. C. Differential effects of cyclic and constant stress on ATP release and mucociliary transport by human airway epithelia. (2007) *J Physiol* 580(2), 577-592
24. Guyot, A., and Hanrahan, J. W. ATP release from human airway epithelial cells studied using a capillary cell culture system (2002) *J Physiol* 545(1), 199-206
25. Lazarowski, E. R., Tarran, R., Grubb, B. R., van Heusden, C. A., Okada, S., and Boucher, R. C. Nucleotide Release Provides a Mechanism for Airway Surface Liquid Homeostasis (2004) *J Biol Chem* 279(35), 36855-36864
26. Picher, M., Burch, L. H., Hirsh, A. J., Spychala, J., and Boucher, R. C. Ecto 5'-Nucleotidase and Nonspecific Alkaline Phosphatase – TWO AMP-

HYDROLYZING ECTOENZYMES WITH DISTINCT ROLES IN HUMAN AIRWAYS (2003) J Biol Chem 278(15), 13468-13479

27. Picher, M., Burch, L. H., and Boucher, R. C. Metabolism of P2 Receptor Agonists in Human Airways: IMPLICATIONS FOR MUCOCILIARY CLEARANCE AND CYSTIC FIBROSIS. (2004) J Biol Chem 279(19), 20234-20241
28. Picher, M., and Burch, L. E-NTPDases in human airways: Regulation and relevance for chronic lung diseases. (2006) Purin Signal. 2, 399-408
29. Morse, D. M., Smullen, J. L., and Davis, C. W. Differential effects of UTP, ATP, and adenosine on ciliary activity of human nasal epithelial cells (2001) Am J Physiol Cell Physiol 280(6), C1485-1497
30. Huang, P., Lazarowski, E. R., Tarran, R., Milgram, S. L., Boucher, R. C., and Stutts, M. J. Compartmentalized autocrine signalling to cystic fibrosis transmembrane conductance regulator at the apical membrane of airway epithelial cells. (2001) Proc Natl Acad Sci U S A 98(24), 14120-14125
31. Yerxa, B. R., Sabater, J. R., Davis, C. W., Stutts, M. J., Lang-Furr, M., Picher, M., Jones, A. C., Cowlen, M., Dougherty, R., Boyer, J., Abraham, W. M., and Boucher, R. C. Pharmacology of INS37217 [P1-(uridine 5')-P4-(2'-deoxycytidine 5')tetraphosphate, Tetrasodium Salt], a next-generation P2Y2 receptor agonist for the treatment of cystic fibrosis. (2002) J Pharmacol Exp Ther 302(3), 871-880
32. Okada, S. F., Nicholas, R. A., Kreda, S. M., Lazarowski, E. R., and Boucher, R. C. Physiological Regulation of ATP Release at the Apical Surface of Human Airway Epithelia (2006) J. Biol. Chem., M603019200
33. Takemura, H., Takamura, Y., Isono, K., Tamaoki, J., Nagai, A., and Kawahara, K. Hypotonicity-Induced ATP Release Is Potentiated by Intracellular Ca^{2+} and Cyclic AMP in Cultured Human Bronchial Cells (2003) Japanese J. Physiol. 53, 319-326
34. Zimmermann, H. Extracellular metabolism of ATP and others nucleotides. (2000) Naunyn-Schmiedeberg's Archives Of Pharmacology 362(4-5), 299-309
35. Millán, J. Alkaline Phosphatases (2006) Purinergic Signalling 2(2), 335-341
36. Picher, M., and Boucher, R. C. Biochemical Evidence for an Ecto Alkaline Phosphodiesterase I in Human Airways (2000) Am J Respir Cell Mol Biol 23(2), 255-261
37. Donaldson, S. H., Lazarowski, E. R., Picher, M., Knowles, M. R., Stutts, M. J., and Boucher, R. C. Basal Nucleotide Levels, Release, and Metabolism in Normal and Cystic Fibrosis Airways. (2000) Mol Med 6(11), 969-982
38. Picher, M., and Boucher, R. C. Metabolism of extracellular nucleotides in human airways by a multienzyme system. Drug Dev. Res. (2001) Drug Dev. Res. 52, 66-75

39. Donaldson, S. H., Picher, M., and Boucher, R. C. Secreted and Cell-Associated Adenylate Kinase and Nucleoside Diphosphokinase Contribute to Extracellular Nucleotide Metabolism on Human Airway Surfaces (2002) *Am J Respir Cell Mol Biol* 26(2), 209-215
40. Picher, M., and Boucher, R. C. Human Airway Ecto-adenylate Kinase A MECHANISM TO PROPAGATE ATP SIGNALING ON AIRWAY SURFACES (2003) *J Biol Chem* 278(13), 11256-11264
41. Hirsh, A., Picher, M., and Boucher, R. Adenosine metabolism and transport by human airway epithelium. (2001) *Ped. Pulmonol.* 22, 241
42. Fulcher, M. L., Gabriel, S., Burns, K. A., Yankaskas, J. R., and Randell, S. H. Well-differentiated human airway epithelial cell cultures. (2005) *Methods Mol Med* 107, 183-206
43. Donaldson, S. H., Picher, M. and Boucher, R. C. Secreted and Cell-Associated Adenylate Kinase and Nucleoside Diphosphokinase Contribute to Extracellular Nucleotide Metabolism on Human Airway Surfaces. *Am. J. Respir. Cell Mol. Biol.*, February 1, 2002; 26(2): 209 - 215.
44. Apell, H.-J. (2004) *Bioelectrochemistry* 63(1-2), 149-156
45. Dixon, M., and Webb, E. C. (1979) *Enzyme Inhibition and Activation* In. *Enzymes*, Longmans & Green New York
46. Knight, G. E., Bodin, P., De Groat, W. C., and Burnstock, G. ATP is released from guinea pig ureter epithelium on distension (2002) *Am J Physiol Renal Physiol* 282(2), F281-288
47. Hirschberg, C. B., Robbins, P. W., and Abeijon, C. Transporters of nucleotide sugars, ATP, and nucleotide sulfate in the endoplasmic reticulum and Golgi apparatus (1998) *Annual Review of Biochemistry* 67(1), 49-69
48. Bodin, P., and Burnstock, G. Evidence that release of ATP from endothelial cells during increased shear stress is vesicular. (2001) *J. Cardiovasc. Pharmacol.* 38(6), 900-908
49. Ikehara, Y., Mansho, K., Takahashi, K., and Kato, K. Purification and Characterization of Alkaline Phosphatase from Plasma Membranes of Rat Ascites Hepatoma (1978) *J Biochem (Tokyo)* 83(5), 1471-1483
50. Fortuna, R., Anderson, H. C., Carty, R. P., and Sajdeja, S. W. Enzymatic characterization of the matrix vesicle alkaline phosphatase isolated from bovine fetal epiphyseal cartilage. (1980) *Calcif. Tissue Int.* 30(3), 217-225
51. Simao, A. M. S., Beloti, M. M., Cezarino, R. M., Rosa, A. L., Pizauro, J. M., and Ciancaglini, P. (2007) *Comparative Biochemistry and Physiology - Part A: Molecular & Integrative Physiology* 146(4), 679-687

52. Seargeant, L. E., and Stinson, R. A. Inhibition of human alkaline phosphatases by vanadate. (1979) *Can. J. Biochem.* 57(7), 2000-2007
53. Pizauro, J. M., Ciancaglini, P., and Leone, F. A. Allosteric modulation by ATP, calcium and magnesium ions of rat osseous plate alkaline phosphatase. (1993) *Biochimica et Biophysica Acta (BBA) - Protein Structure and Molecular Enzymology* 1202(1), 22-28
54. Demenis, M. A., Furriel, R. P. M., and Leone, F. A. Characterization of an ectonucleoside triphosphate diphosphohydrolase 1 activity in alkaline phosphatase-depleted rat osseous plate membranes: possible functional involvement in the calcification process. (2003) *Biochimica et Biophysica Acta (BBA) - Proteins & Proteomics* 1646(1-2), 216-225
55. Mitchell, C. H., Carre, D. A., McGlinn, A. M., Stone, R. A., and Civan, M. M. A release mechanism for stored ATP in ocular ciliary epithelial cells (1998) *Proc. Natl. Acad. Sci.* 95(12), 7174-7178
56. Hazama, A., Hayashi, S., and Okada, Y. Cell surface measurements of ATP release from single pancreatic β cells using a novel biosensor technique. (1998) *Pflügers Archiv European Journal of Physiology* 437(1), 31-35
57. Hazama, A., Shimizu, T., Ando-Akatsuka, Y., Hayashi, S., Tanaka, S., Maeno, E., and Okada, Y. Swelling-induced, CFTR-independent ATP Release from a Human Epithelial Cell Line: Lack of Correlation with Volume-sensitive Cl^- Channels (1999) *J. Gen. Physiol.* 114(4), 525-533
58. Sunderman, F. W. The clinical biochemistry of 5'-nucleotidase. (1990) *Ann. Clin. Lab. Sci* 20(2), 123-139
59. Van Belle, H. Alkaline phosphatase. I. Kinetics and inhibition by levamisole of purified isoenzymes from humans. (1976) *Clin Chem* 22(7), 972-976
60. Gordon, E. L., Pearson, J. D., and Slakey, L. L. The hydrolysis of extracellular adenine nucleotides by cultured endothelial cells from pig aorta. Feed-forward inhibition of adenosine production at the cell surface. (1986) *J. Biol. Chem.* 261(33), 15496-15507
61. Slakey, L. L., Cosimini, K., Earls, J. P., ThomasC, and Gordon, E. L. Simulation of extracellular nucleotide hydrolysis and determination of kinetic constants for the ectonucleotidases. (1986) *J. Biol. Chem.* 261(33), 15505-15507
62. Maroto, R., and Hamill, O. P. Brefeldin a block of integrin-dependent mechanosensitive ATP Release from xenopus oocytes reveals a novel mechanism of mechanotransduction. (2001) *J. Biol. Chem.* 276(26), 23867-23872
63. Chen, Y., Zhao, Y. H., and Wu, R. Differential regulation of airway mucin gene expression and mucin secretion by extracellular nucleotide triphosphates. (2001) *Am. J. Respir. Cell Mol. Biol.* 25(4), 409-417

64. Conway, J. D., Bartolotta, T., Abdullah, L. H., and Davis, C. W. Regulation of mucin secretion from human bronchial epithelial cells grown in murine hosted xenografts. (2003) *Am J Physiol Lung Cell Mol Physiol* 284(6), L945-954
65. Kukulski, F., Levesque, S. A., Lavoie, E. G., Lecka, J., Bigonnesse, F., Knowles, A. F., Robson, S., Kirley, T. L., and Sevigny, J. Comparative hydrolysis of P2 receptor agonists by NTPDases 1, 2, 3 and 8. (2005) *Purin Signal.* 1, 193-204
66. Say, J. C., Ciuffi, K., Furriel, R. P., Ciancaglini, P., and Leone, F. A. Alkaline phosphatase from rat osseous plates: purification and biochemical characterization of a soluble form. (1991) *Biochim Biophys Acta* 1074(2), 256-262
67. Hourani, S. M. Purinoceptors and platelet aggregation. (1996) *J. Auton. Pharmacol.* 16(6), 349-352
68. Kahner, B. N., Shankar, H., Murugappan, S., Prasad, G. L., and Kunapuli, S. P. Nucleotide receptor signaling in platelets. (2006) *Journal of Thrombosis and Haemostasis* 4(11), 2317-2326
69. Eltzschig, H. K., Ibla, J. C., Furuta, G. T., Leonard, M. O., Jacobson, K. A., Enjyoji, K., Robson, S. C., and Colgan, S. P. Coordinated Adenine Nucleotide Phosphohydrolysis and Nucleoside Signaling in Post-Hypoxic Endothelium: Role of Ectonucleotidases and Adenosine A2B-Receptors. (2003) *J Exp Med* 198(5), 783-796
70. Le Hir, M., Gandhi, R., and Dubach, U. C. Purification and properties of a 5'-nucleotidase from rat renal membranes. (1989) *Enzyme* 41(2), 87-93
71. Stefanovic, V., Savic, V., Vlahovic, P., Ardaillou, N., and Ardaillou, R. Ecto-5'-nucleotidase of cultured rat mesangial cells. (1988) *Ren. Physiol. Biochem.* 11(1), 89-102
72. Matharu, A.-L., Mundell, S. J., Benovic, J. L., and Kelly, E. Rapid Agonist-induced Desensitization and Internalization of the A_{2B} Adenosine Receptor Is Mediated by a Serine Residue Close to the COOH Terminus. (2001) *J. Biol. Chem.* 276(32), 30199-30207
73. Mohsenin, A., and Blackburn, M. Adenosine signaling in asthma and chronic obstructive pulmonary disease. (2006) *Curr Opin Pulm Med* 12(1), 54-59
74. H. Berg, "Random Walks in Biology" (Princeton University Press, 1993)
75. Diehl, H., Ihlefeld, and H. Schwegler. 1991. *Physik fur Biologen.* Springer-Verlag, Berline, P.391.
76. Cusack NJ, Pearson JD, Gordon JL. " Stereoselectivity of ectonucleotidases on vascular endothelial cells." 1983. Sep 15;214(3):975-81.
77. Quinton P.M., Cystic Fibrosis: Lessons from the Sweat Gland. *Physiology* 2007. 22:212—25

78. Donaldson SH, Bennett WD, Zeman KL, Knowles MR, Tarran R, Boucher RC, Mucus Clearance and Lung Function in Cystic Fibrosis with Hypertonic Saline. *New England Journal of Medicine*, 2006.354:241
79. Novotny, J.A. and E. Jakobsson, Computational studies of ion-water flux coupling in the airway epithelium. I. CONSTRUCTION OF A MODEL. *Am.J.Physiol.*, 1996. 270: p. C1751-C1763
80. Novotny, J.A. and E. Jakobsson, Computational studies of ion-water flux coupling in the airway epithelium. II. ROLE OF SPECIFIC TRANSPORT MECHANISMS. *Am.J.Physiol.*, 1996. 270: p. C1764-C1772.
81. Willumsen NJ, Boucher RC. Transcellular sodium transport in cultured cystic fibrosis human nasal epithelium. *Am J Physiol*. 1991.261(2 Pt 1): C332-41.
82. Willumsen NJ, Boucher RC. Sodium transport and intracellular sodium activity in cultured human nasal epithelium. *Am J Physiol*. 1991.261(2 Pt 1):C319-31.
83. Willumsen NJ, Boucher RC. Shunt resistance and ion permeabilities in normal and cystic fibrosis airway epithelia. *Am J Physiol*. 1989. 256(5 Pt 1):C1054-63.
84. Willumsen NJ, Davis CW, Boucher RC. Cellular Cl⁻ transport in cultured cystic fibrosis airway epithelium. *Am J Physiol*. 1989. 256(5 Pt 1):C1045-53.
85. Willumsen NJ, Davis CW, Boucher RC. Intracellular Cl⁻ activity and cellular Cl⁻ pathways in cultured human airway epithelium. *Am J Physiol*. 1989. 256 (5 Pt 1):C1033-44.
86. Breeze, R.G. and E.B. Wheeldon. The cells of the pulmonary airways. *Am. Rev. Respir. Dis*. 116:705-777, 1977
87. Widdicombe, J. H., C. B. Basbaum, and E. Highland. Ion contents and other properties of isolated cells from dog tracheal epithelium. *Am. J. Physiol*. 1981.Z. 241: C184-C 192.
88. Lazarowski, E.R., Tarra, R., Grubb, B.R., van Heusden, C.A., Okada, S., and Boucher, R.C. 2004. Nucleotide release provides a mechanism for airway surface liquid homeostasis. *J. Biol. Chem*. 279:36855-36864
89. Fischer H, Illek B, Finkbeiner WE, Widdicombe JH. Basolateral Cl channels in primary airway epithelial cultures. *Am J Physiol Lung Cell Mol Physiol*. 2007 Jun;292(6):L1432-43.
90. Leuba, D., De Ribaupierre, Y., and Kucera, P. 1996. Ion transport, ciliary activity, and mechanosensitivity of sinus mucosa: an in vitro study. *Am. J. Physiol*. 271:L349-L358
91. Taylor, A.L., Kudlow, B.A., Marrs, K.L., Gruenert, D.C., W.B.Guggino,, and Schwiebert, E.M. 1998. Bioluminescence detection of ATP release mechanisms in

epithelia. *Am. J. Physiol.* 275:C1391-C1406

92. Homolya, L., Steinberg, A.D., and Boucher, R.C. 2000. Cell to cell communication in response to mechanical stress via bilateral release of ATP and UTP in polarized epithelia. *J. Cell Biol.* 150:1349-1360
93. He-Ping Ma, Sunil Saxena, and David G. Warnock Anionic Phospholipids Regulate Native and Expressed Epithelial Sodium Channel (ENaC) *J. Biol. Chem.* 2002 277: 7641-7644.
94. Marcus Mall, Andreas Wissner, Tanja Gonska, Detlef Calenborn, Joachim Kuehr, Matthias Brandis, and Karl Kunzelmann Inhibition of Amiloride-Sensitive Epithelial Na⁺ Absorption by Extracellular Nucleotides in Human Normal and Cystic Fibrosis Airways. *Am. J. Respir. Cell Mol. Biol.* 23: 755-761
95. Gang Yue, Bela Malik, Guichin Yue, and Douglas C. Eaton Phosphatidylinositol 4,5-Bisphosphate (PIP₂) Stimulates Epithelial Sodium Channel Activity in A6 Cells. *J. Biol. Chem.*, Mar 2002; 277: 11965 - 11969
96. Reddy MM, Light MJ, Quinton PM. Activation of the epithelial Na⁺ channel (ENaC) requires CFTR Cl⁻ channel function. *Nature* 1999, 402:301-04
97. Robert Tarran, Matthew E. Loewen, Anthony M. Paradiso, John C. Olsen, Micheal A. Gray, Barry E. Argent, Richard C. Boucher, and Sherif E. Gabriel Regulation of Murine Airway Surface Liquid Volume by CFTR and Ca²⁺-activated Cl⁻ Conductances *J. Gen. Physiol.*, Aug 2002; 120: 407 – 418
98. Paradiso AM, Mason SJ, Lazarowski ER, Boucher RC. Membrane-restricted regulation of Ca²⁺ release and influx in polarized epithelia. *Nature*. 1995 Oct 19; 377(6550): 643-6.
99. Ribeiro CM, Paradiso AM, Carew MA, Shears SB, Boucher RC. Cystic fibrosis airway epithelial Ca²⁺_i signaling: the mechanism for the larger agonist-mediated Ca²⁺_i signals in human cystic fibrosis airway epithelia. *J Biol Chem.* 2005 Mar 18;280(11):10202-9. Epub 2005 Jan 12.
100. Mason SJ, Paradiso AM, Boucher RC. Regulation of transepithelial ion transport and intracellular calcium by extracellular ATP in human normal and cystic fibrosis airway epithelium. *Br J Pharmacol.* 1991 Jul; 103(3):1649-56.
101. Chambers LA, Constable M, Clunes MT, Olver RE, Ko WH, Inglis SK, Wilson SM. Adenosine-evoked Na⁺ transport in human airway epithelial cells. *Br J Pharmacol.* 2006 Sep;149(1):43-55.
102. LL Clarke, T Chinet and RC Boucher. Extracellular ATP stimulates K⁺ secretion across cultured human airway epithelium. *Am J Physiol* (1997) 272: L1084-91.
103. Boucher RC, Stutts MJ, Gatzky JT. Regional differences in bioelectric properties and ion flow in excised canine airways. *J Appl Physiol.* 1981 Sep; 51(3):706-14.

- 104.** A. Lazrak, A. Samanta, and S. Matalon. Biophysical properties and molecular characterization of amiloride-sensitive sodium channels in A549 cells. *Am J Physiol Lung Cell Mol Physiol*. 2000 Apr; 278(4): L848-57.
- 105.** Matsui, H., Davis, C.W., Tarran, R., and Boucher, R.C. Osmotic water permeabilityies of cultured, well-differentiated normal and cystic fibrosis airway epithelia. *J. Clin. Invest*. 2000; 105:1419-1427